



The University of Manchester

# Computational Fluid Dynamics for Intracranial Aneurysms in Clinical Settings

---

*A dissertation submitted to The University of Manchester for the degree of Bachelor of  
Engineering in the Faculty of Science and Engineering*

2025

**Dineth Ramida Ilapperuma**

Student ID: 11121002

Supervisor: Dr. Amir Keshmiri  
The School of Engineering

# Contents

<b>Abstract</b>	<b>8</b>
<b>Lay Summary</b>	<b>9</b>
<b>Declaration</b>	<b>10</b>
<b>Intellectual Property Statement</b>	<b>11</b>
<b>Dedication</b>	<b>12</b>
<b>Acknowledgments</b>	<b>13</b>
<b>Abbreviations</b>	<b>15</b>
<b>Nomenclature</b>	<b>15</b>
<b>Glossary</b>	<b>16</b>
<b>1 Introduction</b>	<b>17</b>
1.1 Aneurysms . . . . .	17
1.1.1 Symptoms . . . . .	19
1.1.2 Risk Factors . . . . .	19
1.2 Treatment Options . . . . .	20
1.2.1 Flow Diversion Stents . . . . .	20
1.2.2 Endovascular Coiling . . . . .	21
1.2.3 Surgical Clipping . . . . .	22
1.3 CFD in Biology . . . . .	23
1.3.1 Key Groups and Stakeholders . . . . .	23
1.4 Background . . . . .	24
1.5 Scope of the Study . . . . .	25
1.6 Aims and Objectives . . . . .	25
1.6.1 Aims . . . . .	25
1.6.2 Objectives . . . . .	26
<b>2 Literature Review</b>	<b>27</b>
2.1 Haemodynamic Parameters . . . . .	28
2.1.1 Wall Shear Stress . . . . .	28
2.1.2 Time-Averaged Wall Shear Stress . . . . .	29
2.1.3 Oscillatory Shear Index . . . . .	29
2.1.4 Relative Residence Time . . . . .	29
2.2 Mechanobiology of Aneurysms . . . . .	30

2.2.1	High-flow Theory . . . . .	30
2.2.2	Low-Flow Theory . . . . .	32
2.2.3	Current Perspective . . . . .	33
2.3	Star-CCM+ Meshing . . . . .	35
2.3.1	Tetrahedral Meshes . . . . .	35
2.3.2	Polyhedral Meshes . . . . .	35
2.4	Mesh Suitability for Aneurysm Simulation . . . . .	36
<b>3</b>	<b>Methodology</b>	<b>37</b>
3.1	CFD Modelling . . . . .	38
3.1.1	CFD Model Development: SimVascular . . . . .	38
3.1.2	Mesh Generation: STAR-CCM+ . . . . .	39
3.1.3	Grid Independence . . . . .	40
3.1.4	Boundary Conditions . . . . .	42
3.1.5	Physics Continuum . . . . .	43
3.1.6	Solver Settings . . . . .	43
3.2	Haemodynamic Parameters . . . . .	44
3.2.1	Wall Shear Stress (WSS) . . . . .	44
3.2.2	Time-Averaged Wall Shear Stress (TA-WSS) . . . . .	44
3.2.3	Oscillatory Shear Index (OSI) . . . . .	45
3.2.4	Relative Residence Time (RRT) . . . . .	46
3.3	Simulation of Endovascular Treatments . . . . .	46
3.3.1	Flow Diversion Stents . . . . .	46
3.3.2	Endovascular Coiling . . . . .	47
3.4	Model Validation and Verification . . . . .	48
3.5	Replicability and Transparency . . . . .	48
3.6	Limitations and Justifications . . . . .	49
3.6.1	Rigid body: Fluid structure interaction . . . . .	49
3.6.2	Blood Flow . . . . .	49
3.6.3	Cardiac Cycle . . . . .	49
<b>4</b>	<b>Results and Discussion</b>	<b>50</b>
4.1	Case 1 . . . . .	51
4.1.1	TA-WSS . . . . .	51
4.1.2	OSI . . . . .	52
4.1.3	RRT . . . . .	53
4.1.4	Streamlines . . . . .	54
4.1.5	Velocity Contours . . . . .	54
4.1.6	Pressure Contours . . . . .	54
4.1.7	Summary . . . . .	55
4.2	Case 2 . . . . .	56
4.2.1	TA-WSS . . . . .	56
4.2.2	OSI . . . . .	57
4.2.3	RRT . . . . .	58
4.2.4	Streamlines . . . . .	59
4.2.5	Velocity Contours . . . . .	59
4.2.6	Pressure Contours . . . . .	59
4.2.7	Summary . . . . .	60

4.3	Case 1 with a flow diversion stent . . . . .	61
4.3.1	TA-WSS . . . . .	61
4.3.2	OSI . . . . .	62
4.3.3	RRT . . . . .	63
4.3.4	Streamlines . . . . .	64
4.3.5	Velocity Contours . . . . .	64
4.3.6	Pressure Contours . . . . .	64
4.3.7	Summary . . . . .	65
4.4	Case 2 with a flow diversion stent . . . . .	66
4.4.1	TA-WSS . . . . .	66
4.4.2	OSI . . . . .	67
4.4.3	RRT . . . . .	68
4.4.4	Streamlines . . . . .	69
4.4.5	Velocity Contours . . . . .	69
4.4.6	Pressure Contours . . . . .	69
4.4.7	Summary . . . . .	70
4.5	Case 1 with an endovascular coiling . . . . .	71
4.5.1	TA-WSS . . . . .	71
4.5.2	OSI . . . . .	72
4.5.3	RRT . . . . .	73
4.5.4	Streamlines . . . . .	74
4.5.5	Velocity Contours . . . . .	74
4.5.6	Pressure Contours . . . . .	74
4.5.7	Summary . . . . .	75
4.6	Case 2 with an endovascular coiling . . . . .	76
4.6.1	TA-WSS . . . . .	76
4.6.2	OSI . . . . .	77
4.6.3	RRT . . . . .	78
4.6.4	Streamlines . . . . .	79
4.6.5	Velocity Contours . . . . .	79
4.6.6	Pressure Contours . . . . .	79
4.6.7	Summary . . . . .	80
4.7	Uncertainty Analysis . . . . .	81
4.8	Comparative Quantitative Analysis . . . . .	82
4.8.1	Case 1 vs. Case 2 . . . . .	82
4.8.2	Case 1 vs. Case 1 (stent) vs. Case 1 (coil) . . . . .	84
4.8.3	Case 2 vs. Case 2 (stent) vs. Case 2 (coil) . . . . .	87
<b>5</b>	<b>Conclusions</b>	<b>90</b>
5.1	Future Work and Limitations . . . . .	92
5.2	Recommendations and Applications . . . . .	93
<b>6</b>	<b>Management</b>	<b>95</b>
6.1	Project Plan and Reflection . . . . .	95
6.2	Future Work . . . . .	96
6.3	Ethical Approval and University Policy . . . . .	96

**Word count: 25,000**

# List of Figures

1.1	Visualisation of an aneurysm (The Royal Children's Hospital 2020) . . . . .	17
1.2	Aneurysm characteristics (Inselspital, Bern University Hospital 2024) . . . . .	18
1.3	Flow Diversion Stents inside an Aneurysm (Mayfield Clinic 2015) . . . . .	20
1.4	Endovascular Coiling inside an Aneurysm (The Royal Children's Hospital 2020) . . . . .	21
1.5	Surgical Clipping of an Aneurysm (The Royal Children's Hospital 2020) . . . . .	22
1.6	Location of the aneurysms (Lebedeva et al. 2013) . . . . .	24
2.1	Illustration of High-Flow and Low-Flow Theories (Giotta Lucifero et al. 2021) . . . . .	30
2.2	Comparison between high-flow and low-flow theories(Meng et al. 2014) . . . . .	33
2.3	Polyhedral Mesh . . . . .	36
3.1	Methodology Workflow . . . . .	37
3.2	Image visualisation to modelling on SimVascular (Lan et al. 2018) . . . . .	38
3.3	Polyhedral mesh cell set for case 1 . . . . .	39
3.4	Cross-sectional planes along case 1 for pressure and velocity analysis. . . . .	40
3.5	Grid independence plots comparing Case 1 and Case 2 . . . . .	41
3.6	Boundary Conditions of IA . . . . .	42
3.7	Inlet velocity monitor plot . . . . .	42
3.8	Flow Diversion Stents . . . . .	47
3.9	Endovascular Coiling . . . . .	47
4.1	Planes and Streamlines (Janiga et al. 2015) . . . . .	50
4.2	3D diagram of TA-WSS for case 1 . . . . .	51
4.3	Detailed TA-WSS for case 1 . . . . .	51
4.4	3D diagram of OSI for case 1 . . . . .	52
4.5	Detailed OSI for case 1 . . . . .	52
4.6	3D diagram of RRT for case 1 . . . . .	53
4.7	Detailed RRT for case 1 . . . . .	53
4.8	Streamlines of case 1 . . . . .	54
4.9	Velocity contours of case 1 . . . . .	54
4.10	Pressure contours of case 1 . . . . .	54

4.11	Predicted rupture locations for case 1 . . . . .	55
4.12	3D diagram of TA-WSS for case 2 . . . . .	56
4.13	Detailed TA-WSS for case 2 . . . . .	56
4.14	3D diagram of OSI for case 2 . . . . .	57
4.15	Detailed OSI for case 2 . . . . .	57
4.16	3D diagram of RRT for case 2 . . . . .	58
4.17	Detailed RRT for case 2 . . . . .	58
4.18	Streamlines of case 2 . . . . .	59
4.19	Velocity contours of case 2 . . . . .	59
4.20	Pressure contours of case 2 . . . . .	59
4.21	Predicted rupture locations for case 2 . . . . .	60
4.22	3D diagram of TA-WSS for case 1 with a stent . . . . .	61
4.23	Detailed TA-WSS for case 1 with a stent . . . . .	61
4.24	3D diagram of OSI for case 1 with a stent . . . . .	62
4.25	Detailed OSI for case 1 with a stent . . . . .	62
4.26	3D diagram of RRT for case 1 with a stent . . . . .	63
4.27	Detailed RRT for case 1 with a stent . . . . .	63
4.28	Streamlines of case 1 with a stent . . . . .	64
4.29	Velocity contours of case 1 with a stent . . . . .	64
4.30	Pressure contours of case 1 with a stent . . . . .	64
4.31	Predicted rupture locations for case 1 with a stent . . . . .	65
4.32	3D diagram of TA-WSS for case 2 with a flow diversion stent . . . . .	66
4.33	Detailed TA-WSS for case 2 with a stent . . . . .	66
4.34	3D diagram of OSI for case 2 with a flow diversion stent . . . . .	67
4.35	Detailed OSI for case 2 with a stent . . . . .	67
4.36	3D diagram of RRT for case 2 with a flow diversion stent . . . . .	68
4.37	Detailed RRT for case 2 with a stent . . . . .	68
4.38	Streamlines of case 2 with a flow diversion stent . . . . .	69
4.39	Velocity contours of case 2 with a flow diversion stent . . . . .	69
4.40	Pressure contours of case 2 with a flow diversion stent . . . . .	69
4.41	Predicted rupture locations for case 2 with a stent . . . . .	70
4.42	3D diagram of TA-WSS for case 1 with an endovascular coiling . . . . .	71
4.43	Detailed TA-WSS for case 1 with an endovascular coil . . . . .	71
4.44	3D diagram of OSI for case 1 with an endovascular coiling . . . . .	72
4.45	Detailed OSI for case 1 with an endovascular coil . . . . .	72
4.46	3D diagram of RRT for case 1 with an endovascular coiling . . . . .	73
4.47	Detailed RRT for case 1 with an endovascular coil . . . . .	73
4.48	Streamlines of case 1 with an endovascular coiling . . . . .	74
4.49	Velocity contours of case 1 with an endovascular coiling . . . . .	74

4.50	Pressure contours of case 1 with an endovascular coiling . . . . .	74
4.51	Predicted rupture locations for case 1 with a coil . . . . .	75
4.52	3D diagram of TA-WSS for case 2 with an endovascular coiling . . . . .	76
4.53	Detailed TA-WSS for case 2 with an endovascular coil . . . . .	76
4.54	3D diagram of OSI for case 2 with an endovascular coiling . . . . .	77
4.55	Detailed OSI for case 2 with an endovascular coil . . . . .	77
4.56	3D diagram of RRT for case 2 with an endovascular coiling . . . . .	78
4.57	Detailed RRT for case 2 with an endovascular coil . . . . .	78
4.58	Streamlines of case 2 with an endovascular coiling . . . . .	79
4.59	Velocity contours of case 2 with an endovascular coiling . . . . .	79
4.60	Pressure contours of case 2 with an endovascular coiling . . . . .	79
4.61	Predicted rupture locations for case 2 with a coil . . . . .	80
4.62	Quantitative comparison of parameters . . . . .	82
4.63	Visualisation of results for case 1 . . . . .	83
4.64	Visualisation of results for case 2 . . . . .	83
4.65	Quantitative comparison of parameters . . . . .	84
4.66	Visualisation of results for case 1 . . . . .	85
4.67	Visualisation of results for case 1 with a stent . . . . .	85
4.68	Visualisation of results for case 1 with an endovascular coil . . . . .	85
4.69	Quantitative comparison of parameters . . . . .	87
4.70	Visualisation of results for case 2 . . . . .	88
4.71	Visualisation of results for case 2 with a stent . . . . .	88
4.72	Visualisation of results for case 2 with an endovascular coil . . . . .	88
5.1	Representation of aneurysm shapes (Withers et al. 2013) . . . . .	93
5.2	Woven EndoBridge device (Mayfield Clinic 2015) . . . . .	94

# List of Tables

2.1	Summary of hemodynamic pattern and vascular wall changes (Staarmann et al. 2019) . . . . .	28
2.2	Haemodynamic parameters used to predict rupture sites after selection of ruptured cases (Janiga et al. 2015) . . . . .	34
3.1	Mesh resolution and corresponding number of cells . . . . .	40
4.1	Summary of case 1 . . . . .	55
4.2	Summary of case 2 . . . . .	60
4.3	Summary of case 1 with a flow diversion stent . . . . .	65
4.4	Summary of case 2 with a flow diversion stent . . . . .	70
4.5	Summary of case 1 with an endovascular coil . . . . .	75
4.6	Summary of case 2 with an endovascular coil . . . . .	80

# Abstract

Intracranial aneurysm rupture prediction is still largely based on anatomical metrics, which fail to account for haemodynamic complexity and individual variability. Current clinical methods rely heavily on measurements such as sac diameter and neck width, often overlooking the dynamic blood flow conditions that critically influence rupture risk. This study addresses that limitation by applying Computational Fluid Dynamics (CFD) to evaluate key haemodynamic parameters and simulate treatment outcomes, with the goal of supporting clinical decision-making and enabling more personalised, predictive care.

Two patient-specific aneurysms (one wide-neck and single-saccular, the other narrow-neck and multi-saccular) were reconstructed on SimVascular and simulated using STAR-CCM+, with geometries enhanced via CAD models of flow diversion stents and endovascular coils. Haemodynamic analysis focused on time-averaged wall shear stress (TA-WSS), oscillatory shear index (OSI), and relative residence time (RRT).

The results showed that regions with low TA-WSS, high OSI, and elevated RRT correlated strongly with rupture-prone regions, supporting the low-flow theory. Case 1 benefitted more from flow diversion stenting, which produced a smoother haemodynamic profile around the sac. In contrast, case 2, responded best to endovascular coiling, reducing TA-WSS by 87.54% and OSI by 86.7%.

Based on these findings, the study proposes the following haemodynamic thresholds indicative of high rupture risk: TA-WSS gradients above 0.25 Pa, OSI values exceeding 0.24, and blood flow velocities greater than 1.0 m/s. It also presents a treatment selection framework: flow diversion stents are recommended for wide-neck, regular aneurysms, while endovascular coiling is more suitable for irregular, multi-saccular geometries. This study demonstrates that CFD can offer clinically actionable insights, supporting personalised treatment planning and reducing rupture risk.

This research highlights CFD's potential as a practical and reliable clinical decision-making tool, enabling personalised rupture risk prediction and optimal treatment selection. Future research should include fluid–structure interaction and more patient data to refine predictive models and thresholds.

# Lay Summary

Brain aneurysms are life-threatening bulges in blood vessels that can rupture without warning. Around 3% of adults globally have an aneurysm (Brain Aneurysm Foundation 2024), yet accurately predicting which are at risk of rupture remains a challenge. This study explores how computational fluid dynamics can help neurosurgeons identify dangerous aneurysms and decide which treatment is most effective.

Using 3D models based on real patient data, the study examines how blood moves through two different aneurysms, determining which one is more likely to rupture. It then simulated two common treatment methods: inserting a stent to divert blood flow or placing coils inside the aneurysm to seal it off. The simulations tracked haemodynamic parameters, blood pressure, flow speed, and patterns to assess which areas were most vulnerable.

The results showed that certain blood flow behaviours (particularly areas of low speed and swirling patterns) were linked to a higher chance of rupture. By comparing the untreated and treated cases, the study also showed how different treatments influence these risk factors.

This work supports the use of personalised computer simulations in hospitals to help doctors predict rupture risk more accurately and select the most effective and safest treatment for each patient.

# **Declaration**

The author, Dineth Ramida Ilapperuma, declares all work presented in this dissertation has been completed independently, unless otherwise stated. Any material derived from other sources has been properly acknowledged and referenced. No portion of this dissertation has been submitted in support of an application for another degree or qualification at this or any other institution.

# Intellectual Property Statement

- i. The author of this dissertation (including any appendices and/or schedules to this dissertation) owns certain copyright or related rights in it (the “Copyright”) and has granted The University of Manchester certain rights to use such Copyright, including for administrative purposes.
- ii. Copies of this dissertation, either in full or in extracts and whether in hard or electronic copy, may be made only in accordance with the Copyright, Designs and Patents Act 1988 (as amended) and regulations issued under it or, where appropriate, in accordance with licensing agreements which the University has entered into. This page must form part of any such copies made.
- iii. The ownership of certain Copyright, patents, designs, trademarks and other intellectual property (the “Intellectual Property”) and any reproductions of copyright works in the dissertation, for example graphs and tables (“Reproductions”), which may be described in this dissertation, may not be owned by the author and may be owned by third parties. Such Intellectual Property and Reproductions cannot and must not be made available for use without the prior written permission of the owner(s) of the relevant Intellectual Property and/or Reproductions.
- iv. Further information on the conditions under which disclosure, publication and commercialisation of this dissertation, the Copyright and any Intellectual Property and/or Reproductions described in it may take place is available in the University IP Policy, in any relevant Dissertation restriction declarations deposited in the University Library, and The University Library’s regulations.

University IP Policy  
University Library’s regulations

# Dedication

To my family and friends:

Thank you for your constant support and belief in me. You've been there through every challenge, and this journey wouldn't have been possible without you. I'm truly grateful for all of you.

To everyone bravely battling an aneurysm:

Your strength and resilience are truly inspiring. Know that you are not alone in this, and your courage gives hope to others.

To the healthcare professionals working with aneurysm patients:

Thank you for your hard work, dedication, and care. You make an incredible difference in people's lives every day, and I'm thankful for everything you do.

# Acknowledgments

Special thanks are extended to Dr. Amir Keshmiri for providing essential materials, guidance, and continual support, which greatly contributed to the completion of this dissertation.

The assistance provided by Research IT and access to the Computational Shared Facility 4 (CSF4) at The University of Manchester are gratefully acknowledged. Appreciation is particularly given to Dr. Ajay B. Harish, Dr. Michael Mays, Dr. Dania Ahmed, Dr. Adel Nasser, and Ms. Pen Richardson for their valuable support in utilising CSF4.

Gratitude is expressed to the Brain Aneurysm Foundation for actively raising awareness about aneurysms and providing crucial statistical resources. Special appreciation is extended to Judith Willans from Manchester Royal Infirmary, Louise Collins from the Vascular Society, and Georgia Brown from the Circulation Foundation for their insightful guidance in aneurysm treatments.

# Preface

The author is currently pursuing a Bachelor of Engineering (BEng) in Mechanical Engineering at The University of Manchester and is keen about the interdisciplinary nature of the field, particularly in bridging mechanical and biomedical engineering to drive innovation and research advancement.

The author has expertise in computational simulations and is proficient in CAD and simulation software, including AutoCAD, SOLIDWORKS, Blender, MeshLab, STAR-CCM+, Abaqus, and ANSYS Fluent. This knowledge has been further developed through previous internships as a Research and Design Engineer at NAFFCO and as an HVAC Engineer at Danway.

Driven by a passion for biomedical engineering, the author has codeveloped *VIMA* - Visual Impairment Motion Assistant — a device designed using computational simulations of a white cane, currently exhibited at the Renold Hub, located within the new Manchester Innovation District, SISTER.

For more information about VIMA, please visit: [www.vima-tech.co.uk](http://www.vima-tech.co.uk).

Beginning in September 2025, the author will undertake a Master of Science (MSc) in Biomedical Engineering with a focus in Computational Bioengineering, to pursue further research and development aimed at enhancing medical device technology.

# Abbreviations

- IA – Intracranial Aneurysms
  - CFD – Computational Fluid Dynamics
  - CAD – Computer Aided Design
  - WSS – Wall Shear Stress
  - TA-WSS – Time Averaged Wall Shear Stress
  - OSI – Oscillatory Shear Index
  - RRT – Relative Residence Time
  - STL - Stereolithography file format used for 3D model export
- 

# Nomenclature

$\tau_w$	Wall shear stress (Pa)
$\mu$	Dynamic viscosity of blood (Pa·s)
$u$	Tangential velocity component (m/s)
$n$	Normal direction to vessel wall
$T$	Duration of a cardiac cycle (s)
$ \cdot $	Magnitude of a vector

# Glossary

**Intracranial Aneurysm** A bulging of a blood vessel in the brain that can rupture, causing a haemorrhagic stroke.

**Aneurysm Neck** The base or opening of the aneurysm sac where it connects to the parent artery.

**Hemodynamics** The study of blood flow and its forces within the circulatory system.

**Flow Diversion Stent** A metallic mesh tube inserted to divert blood flow away from an aneurysm.

**Endovascular Coiling** A procedure where platinum coils are inserted to promote clotting and occlusion of an aneurysm.

**Subarachnoid Haemorrhage (SAH)** Bleeding into the space surrounding the brain, typically caused by aneurysm rupture.

**Hypertension** High blood pressure, when the pressure in your blood vessels is unusually high (140/90 mmHg or higher).

**Thrombus** Blood clot that forms within a blood vessel, either an artery or a vein.

**Wall Shear Stress (WSS)** The tangential force per unit area exerted by blood flow along the vessel wall.

**Time-Averaged Wall Shear Stress (TA-WSS)** The average shear stress acting on a blood vessel wall over one full cardiac cycle.

**Oscillatory Shear Index (OSI)** A measure of the directional change of wall shear stress, indicating disturbed or reversing blood flow.

**Relative Residence Time (RRT)** A measure of how long blood stays near the vessel wall, used to identify regions of low flow and possible thrombus formation.

# Chapter 1

## Introduction

This chapter provides background about aneurysms and clinical intervention strategies to prevent rupture.

### 1.1 Aneurysms

Recognised as a global health burden associated with high mortality and long-term disability rates, an aneurysm is a bulge or swelling in the wall of a blood vessel. These are commonly developed along the aorta and brain. This study focuses on Intracranial Aneurysms (IA), which are located in arteries at the base of the brain, typically the anterior communicating artery and the internal carotid artery. Together, these two locations account for roughly 60% of all IA cases (NHS 2022). Figure 1.1 illustrates the typical locations of intracranial aneurysms, located at the base of the brain.

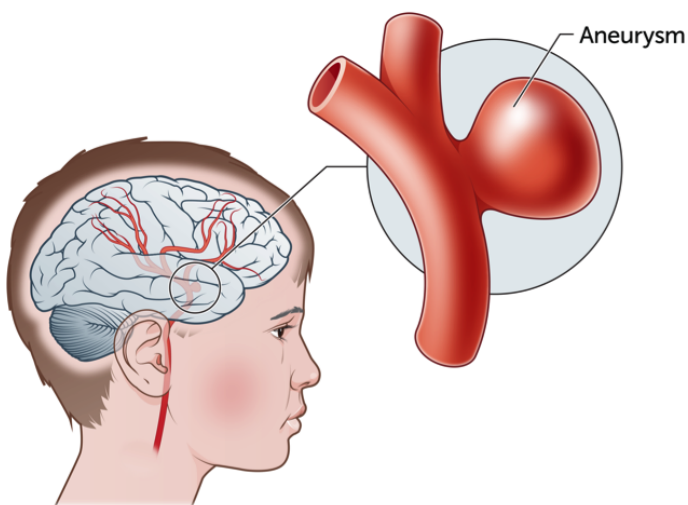


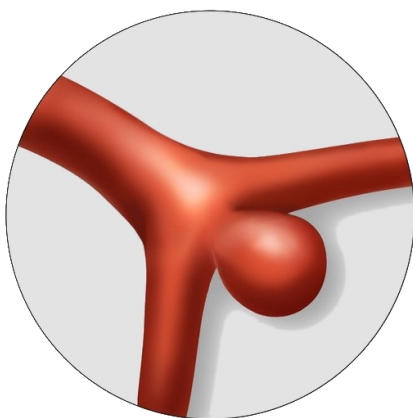
Figure 1.1: Visualisation of an aneurysm (The Royal Children's Hospital 2020)

Aneurysms result in the formation of a saccular outpouching, which is prone to tear and rupture due to the weakened wall lining at the epicenter. The wall lining weakens over time due to the pulsating nature of blood, leading to sac expansion and vessel thinning.

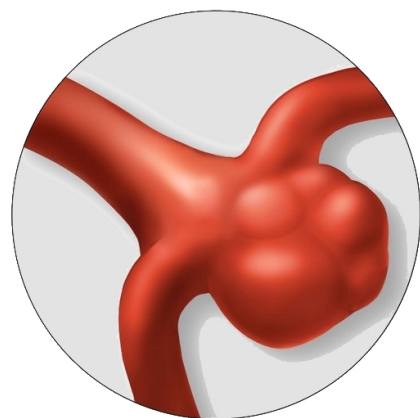
A subarachnoid haemorrhage (SAH), caused by the rupture of the sac, often leads to life-threatening complications within minutes (Hopkins 2018). At the time of writing, an aneurysm ruptures approximately every 18 minutes. (Brain Aneurysm Foundation 2024).

Aneurysms have a 50% mortality rate if ruptured, and of those who survive, about 66% suffer some form of permanent neurological deficit (Brain Aneurysm Foundation 2024). Around 3.2% of the global population, which equates to approximately 250 million people, currently have an unruptured aneurysm. Concerningly, this figure is higher in the United Kingdom with roughly 4% of adults currently suffering with an aneurysm (Walton 2025).

These daunting statistics, coupled with the life-threatening risks aneurysms pose, highlight the urgent need to develop more effective and efficient treatments for patients worldwide. The study of aneurysm rupture, however, remains challenging due to their irregular size, shape, and growth patterns. Their unique geometries complicate both prediction and treatment, as current approaches are often unable to be tailored to individual characteristics. At the time of writing, neurosurgeons and rupture risk calculators primarily estimate rupture risk based on simple physiological parameters. A low-risk aneurysm, as illustrated in Figure 1.2(a), typically exhibits a small sac diameter ( $< 7$  mm), a narrow neck, and a regular, single sac shape. In contrast, Figure 1.2(b) represents a high rupture risk aneurysm, characterised by a larger sac diameter ( $> 10$  mm), a wide neck, and an irregular, multi-saccular morphology.



(a) Low rupture risk



(b) High rupture risk

Figure 1.2: Aneurysm characteristics (Inselspital, Bern University Hospital 2024)

### **1.1.1 Symptoms**

Intracranial aneurysms often prove fatal due to their inconspicuous nature, making them difficult to detect. They are frequently classified as non-critical and, as a result, are often overlooked until rupture or progression to a critical state. Symptoms of an early-stage, unruptured aneurysm (typically < 7 mm in diameter), which are often subtle, include mild headaches, vision changes, and stiffness in eye movement (NHS 2022).

At the onset of rupture, patients may experience more severe symptoms as blood slowly leaks into the surrounding tissue. In such cases, symptoms can rapidly progress to excruciating headaches, nausea, vomiting, drowsiness, dilated pupils, and loss of consciousness (NHS 2022).

Given the severity of a rupture, early identification of even mild symptoms is crucial for improving patient outcomes and preventing catastrophic neurological damage. If unresolved within a short period of time, an aneurysm rupture often results in a coma or death, as evident by the stark 50% mortality rate associated with ruptured aneurysms.

### **1.1.2 Risk Factors**

Several factors contribute to the weakening of the artery wall, increasing the risk of aneurysm formation or rupture. Some of these risk factors are present from birth, while others develop gradually over time due to environmental or lifestyle influences. Age is a significant contributor, with aneurysms more commonly occurring between 30 and 60 years of age. Gender also plays a role, as women are more likely to develop aneurysms than men, with a female-to-male ratio of approximately 3:2 (Brinjikji et al. 2016).

Lifestyle-related factors such as cigarette smoking, heavy alcohol consumption, and the use of illicit drugs are strongly associated with both the formation and rupture of aneurysms. These behaviours raise blood pressure and weaken arterial walls, increasing the likelihood of aneurysm development. High blood pressure itself is a critical risk factor, as the sustained force exerted on arterial walls promotes vascular degeneration over time (Juvela et al. 2008).

Certain genetic conditions and family history significantly increase the risk of aneurysm formation. Inherited connective tissue disorders, such as Ehlers-Danlos syndrome, weaken the blood vessel walls. Structural abnormalities, such as brain arteriovenous malformations, in which arteries and veins are abnormally intertwined, further elevate the likelihood of aneurysm formation (Mayo Clinic 2023).

## 1.2 Treatment Options

With today's medical advancements, three prominent surgical interventions are available for treating unruptured aneurysms. All of these methods share the same principle of preventing blood from entering the aneurysm sac, which leads to its eventual retrusion and shrinkage over time. This section discusses the most common treatment options for aneurysms.

### 1.2.1 Flow Diversion Stents

A stent is used to redirect blood flow away from the aneurysm. These stents are typically made of stainless steel, forming a soft, flexible mesh, as shown in Figure 1.3. The procedure is minimally invasive, relying on a catheter inserted through the groin artery. The stent is then placed at the neck of the aneurysm, effectively rerouting blood flow away from the sac. Over time, new cells grow over the stent, sealing the aneurysm and promoting the retrusion of the sac. Stents are available in varying diameters and lengths, providing a tailored solution for aneurysms of different sizes and locations. They are primarily used for wide-neck aneurysms and for patients over the age of 60, due to their minimally invasive nature.

However, it has been reported that the likelihood of repeat treatment is approximately 15% (Mascitelli et al. 2015). This is attributed to complications arising post-treatment, such as stent failure to adequately divert flow or its interaction within the blood vessel walls. At present, physicians consider stents to be the most effective option for treating early-stage aneurysms, typically those with a smaller sac diameter ( $< 7$  mm). This is due to their relatively low recurrence rate and their ability to treat aneurysms located deep within the brain.

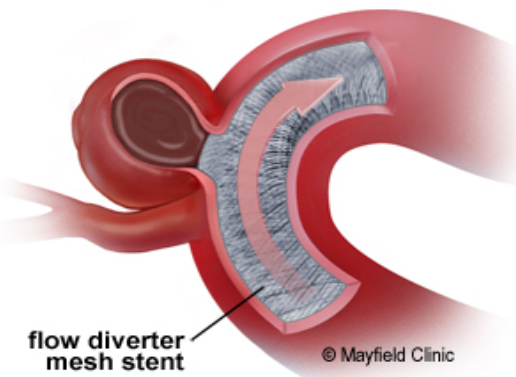


Figure 1.3: Flow Diversion Stents inside an Aneurysm (Mayfield Clinic 2015)

### 1.2.2 Endovascular Coiling

Introduced in the 1990s, coiling involves the use of thin, soft platinum wire shaped like a spring, as shown in Figure 1.4. The coils result in blood stagnation and coagulation, which acts as a deterrent by blocking blood flow from entering the aneurysm sac. A wide range of coils is available, depending on the aneurysm's size, growth rate, and the patient's specific condition. These coils typically range from 1 to 5 millimetres in diameter (Slob et al. 2005).

Similar to flow diversion stents, this method relies on the insertion of a catheter through the groin to guide and place the coils directly into the aneurysm sac. However, unlike flow diversion stents, coiling is specialised for medium-sized aneurysms ( $> 10$  mm) with narrow necks (Liu et al. 2017).

Although this treatment option is effective at sealing aneurysms and has low recurrence and retreatment rates of 20.8% and 10.3%, respectively (Mascitelli et al. 2015). It is frequently critiqued for potential complications, in some cases, coils may protrude into the aneurysm wall or surrounding area, leading to further complications due to puncture of the aneurysm by the catheter, guidewire, or coils. This occurs in approximately 5% of aneurysms that already have a weakened wall (Mayfield Clinic 2015).

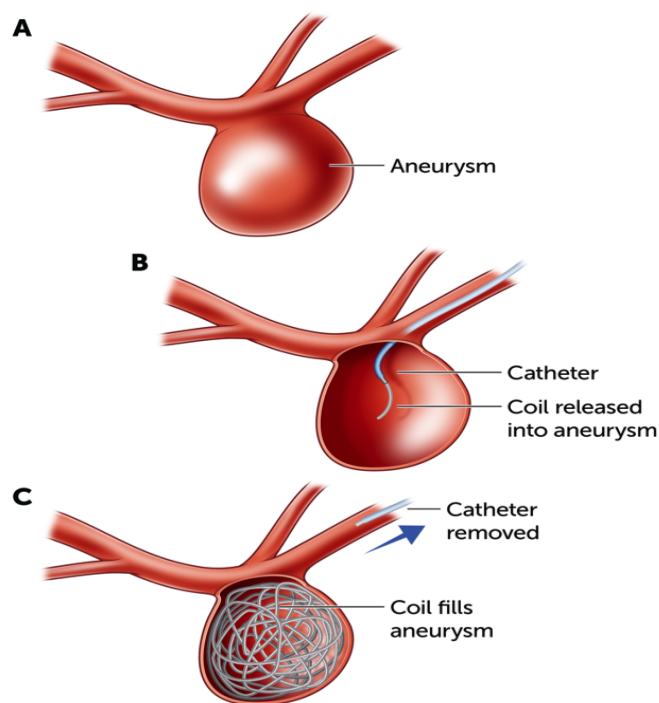


Figure 1.4: Endovascular Coiling inside an Aneurysm (The Royal Children's Hospital 2020)

### 1.2.3 Surgical Clipping

Surgical clipping is a preventative surgical option that involves placing a titanium clip at the neck of an aneurysm, as illustrated by Figure 1.5. This method is regarded as an invasive procedure due to the necessity of making an incision in the skull to access the aneurysm. Consequently, it is often limited in scope, typically applicable only to aneurysms located closer to the skull surface (Dijk et al. 2011).

While surgical clipping is frequently criticised for its invasiveness and prolonged recovery period, it boasts the lowest retreatment rate among treatment options of 1% (Dijk et al. 2011). This makes it a highly reliable choice, particularly for certain types of aneurysms. Additionally, surgical clipping remains effective for aneurysms with irregular shapes or complex geometries, which may not be suitable for endovascular procedures such as coiling or stenting (Belavadi et al. 2021).

However, due to its invasive nature and recent technological advancements in less invasive catheter-based interventions, surgical clipping has become increasingly less common. It is typically recommended for patients who are younger and in good health, as they can tolerate open surgery and the associated risks and recovery time. Surgical clipping is also considered for patients who require an immediate and lasting aneurysm occlusion, particularly when the aneurysm is large or considered high-risk for other methods (Belavadi et al. 2021).

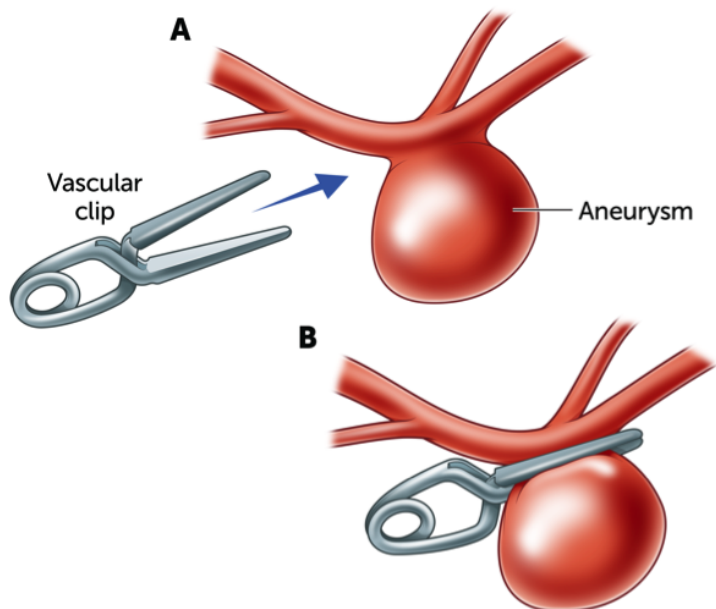


Figure 1.5: Surgical Clipping of an Aneurysm (The Royal Children's Hospital 2020)

## 1.3 CFD in Biology

Computational Fluid Dynamics (CFD) has become a pivotal technology in biomedical engineering, enabling faster medical device certification, reduced risks, and lower research and development costs. A key factor behind this economic shift has been the introduction of *in-silico* simulations, allowing for the exploration of scenarios previously unattainable through conventional *in-vitro* testing.

Furthermore, CFD modelling reduces the need for Magnetic Resonance Imaging (MRI) and Magnetic Resonance Angiography (MRA) following surgery, as the effectiveness of treatments can now be accurately anticipated through computational models. This reduces the need for repeated imaging procedures and helps tailor post-operative care.

### 1.3.1 Key Groups and Stakeholders

CFD is increasingly seen as a transformative technology in the management of aneurysms. The ability to visualise the movement of blood within an aneurysm is crucial for accurately predicting rupture locations and evaluating the effects of preventative treatments. The key groups in this field include patients, clinicians, researchers, and healthcare institutions.

#### Patients

CFD improves treatment outcomes, by providing more accurate rupture predictions, CFD can guide neurosurgeons and physicians in selecting the most appropriate preventative surgery. This allows for tailored treatments, optimising effectiveness and reducing the likelihood of repeat interventions. For patients, this means a reduction in complications and improved survival rates.

#### Neurosurgeons and Physicians

CFD offers neurosurgeons and physicians a deeper understanding of the haemodynamics of aneurysms, which is vital for planning surgeries. Clinicians can anticipate the effects of various treatment approaches, leading to improved surgical decision-making and treatment planning. This is particularly beneficial in the optimisation of minimally invasive interventions, reducing complications and enhancing patient outcomes. Additionally, CFD facilitates the assessment of multiple clinical scenarios and potential treatment strategies, providing valuable quantitative data prior to surgery. This is crucial in predicting aneurysm responses, as each aneurysm has unique geometry and dimensions.

## Healthcare Institutions

Healthcare institutions, including the NHS and hospitals worldwide, can integrate CFD into patient management systems. With more accurate rupture prediction, hospitals can streamline patient care and allocate resources more efficiently. This would allow for the prioritisation of critical aneurysm cases, ensuring faster intervention and reduced mortality rate.

## Biomedical Researchers and Developers

Biomedical researchers and developers working on emerging endovascular techniques will benefit from CFD's ability to model and predict the effects of new treatments. For instance, nano-stents, intrasaccular flow disruptors, and other biodegradable materials can be tested using CFD simulations before being trialled in clinical settings. This reduces the risks associated with the development of new medical devices and speeds up the research and development (R&D) process.

## 1.4 Background

This study utilises two patient-specific aneurysms, sourced from S. Sugiyama in the CFD Rupture Challenge 2013 (Janiga et al. 2015) and provided by Dr. A. Keshmiri. Both aneurysms originate from the left M1 segment, as indicated by the red square in Figure 1.6, and exhibit similar geometric properties.

Case 1 is an unruptured aneurysm, with MRA examinations conducted every 6 months. It has a regular single-sac shape, a large diameter, and a wide neck of 5 mm. Case 2 is a ruptured aneurysm, with a documented rupture site. It has an irregular multi-saccular morphology, a slightly smaller diameter, and a narrow neck of 3 mm.

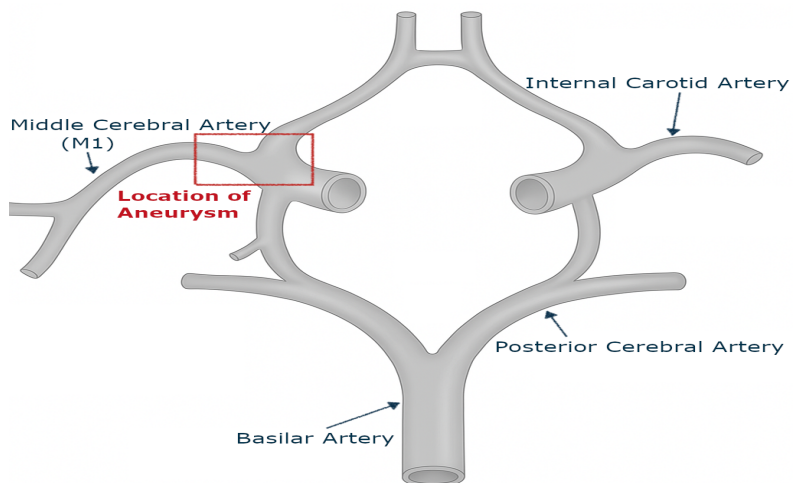


Figure 1.6: Location of the aneurysms (Lebedeva et al. 2013)

## 1.5 Scope of the Study

This study employs CFD software Star-CCM+ v19.02.04 to predict the rupture risk of intracranial aneurysms and evaluate the effectiveness of endovascular treatments, such as flow diversion stents and endovascular coiling. Surgical clipping is not included in this study due to its intrusive nature and limited application, as it is primarily used for aneurysms located near the skull and not for those deep within the brain.

Existing clinical methods for rupture prediction often rely on basic anatomical features, which fail to account for the complex and dynamic haemodynamics within aneurysms and are now considered outdated. This study seeks to better develop the understanding of aneurysm growth and rupture by using CFD data to pinpoint rupture locations, enabling personalised and tailored treatment approaches.

This study is driven by the urgent need to improve patient outcomes and reduce the high mortality associated with aneurysms. The current clinical methods for rupture prediction are insufficient, and by using CFD, this research aims to provide more accurate, quantitative data-driven insights. Ultimately, this study seeks to support clinical decision-making, offering neurosurgeons and physicians the tools to make precise treatment decisions and minimise the risk of reoccurrence, leading to better patient care and improved health outcomes.

## 1.6 Aims and Objectives

### 1.6.1 Aims

Provide a quantitative, data-driven approach to predicting the likelihood and location of aneurysm rupture. Using CFD, this study will evaluate and compare the effectiveness of endovascular treatments, such as flow diversion stents and endovascular coiling.

Furthermore, the study aims to improve patient management systems within healthcare institutions, by prioritising high-risk aneurysms for surgical intervention. Finally, by providing personalised and tailored treatment recommendations, this study will help enhance the effectiveness of aneurysm treatment.

## 1.6.2 Objectives

- Develop patient-specific CFD models for two aneurysms using Star-CCM+, simulating haemodynamic parameters.
- Design flow diversion stents and endovascular coils in SOLIDWORKS, adhering to industrial standards and dimensions.
- Validate and verify the model using benchmark datasets from the CFD Rupture Challenge 2013.
- Perform CFD simulations for aneurysms with three scenarios: baseline (no treatment), flow diversion stent, and endovascular coiling.
- Use haemodynamic parameters, such as Wall Shear Stress (WSS) and Oscillatory Shear Index (OSI), to predict rupture likelihood and the location of aneurysms.
- Investigate haemodynamic characteristics of endovascular treatments.
- Provide personalised and tailored treatment recommendations based on aneurysm geometry and simulation data.
- Improve patient management systems by enabling the prioritisation of high-risk aneurysms for surgical intervention
- Automate the simulation process through the development of macros, which will reduce pre-processing and post-processing times.

# Chapter 2

## Literature Review

The increased accessibility of computational resources in recent decades has significantly accelerated the application of CFD within biomedical engineering. Once limited to simplified flow systems, CFD has since evolved to play a vital role in the design and optimisation of medical devices, including vascular stents and valve prostheses (Reid 2021).

Over the last decade, CFD has been employed in aneurysms extensively, particularly due to the Computational Fluid Dynamics Rupture Challenge 2013. This initiative catalysed research on aneurysms by inviting participants to predict rupture locations based on patient-specific geometries (Phase 1), and subsequently analysing sensitivity to model assumptions (Phase 2) (Janiga et al. 2015).

The challenge demonstrated the feasibility of in-silico rupture prediction but also highlighted the substantial variability that can arise due to model selection, mesh resolution, and boundary conditions.

While the CFD Rupture Challenge advanced the field, it also exposed methodological inconsistencies that complicate clinical translation. These include discrepancies in the oversimplification of wall properties as rigid, and limited use of patient follow-up data for validation.

This chapter critically examines the current state of the literature surrounding aneurysm haemodynamics, with particular focus on rupture prediction metrics, biological mechanisms, and simulation reliability.

## 2.1 Haemodynamic Parameters

### 2.1.1 Wall Shear Stress

Wall Shear Stress (WSS) refers to the tangential force per unit area exerted by flowing blood on the endothelial surface. Under normal physiological conditions (between 1.5 to 2.5 Pa), WSS contributes to endothelial homeostasis and vascular integrity (Dolan et al. 2013). However, deviations from this range, particularly when WSS remains abnormally low, can disrupt endothelial signalling and promote structural weakening of the vessel wall (Aoki et al. 2011).

Intracranial aneurysms are hypothesised to rupture when haemodynamic stresses exceed the mechanical strength of the arterial wall. As WSS is influenced by blood velocity and viscosity, any variation in these properties results in non-uniform distributions across the vessel surface. These fluctuations are captured by the Wall Shear Stress Gradient (WSSG), which quantifies the rate of change in WSS. Accelerating flow yields a positive WSSG, while decelerating flow produces a negative WSSG (Staarmann et al. 2019).

WSS within aneurysms is highly dynamic, evolving with changes in sac morphology and flow patterns. Both abnormally low and excessively elevated WSS levels have been associated with aneurysm progression and rupture, though they are believed to act through distinct mechanobiological pathways. Table 2.1 summarises the vascular responses triggered by different WSS conditions. It is evident from the literature that both extremes in WSS can initiate changes within the vessel wall.

Authors & Year	Parameter	Vascular Wall Changes
Lu & Kassab, 2011	Low WSS	Decreased production of PGI, increased oxidative stress
Zhou et al., 2017	Low WSS	Increased selectin-mediated leukocyte rolling
Papadaki et al., 1998	Low WSS	Decreased tPA production
Hoi et al., 2008	High WSS	MMP production by endothelial cells (ECs)
Fukuda & Aoki, 2015	High WSS	NF- $\kappa$ B and COX-2 increased
Pawlowska et al., 2018	High WSS	IL-1 $\beta$ increased
Shi & Tarbell, 2011	High WSS	PDGF and FGF-2 released from SMCs
Papadaki et al., 1998	High WSS	Increased tPA production

Table 2.1: Summary of hemodynamic pattern and vascular wall changes (Staarmann et al. 2019)

### **2.1.2 Time-Averaged Wall Shear Stress**

Time-Averaged Wall Shear Stress (TA-WSS) represents the mean shear stress exerted on the vessel wall across one cardiac cycle. This parameter mitigates the influence of transient fluctuations arising from the pulsatile nature of blood flow, thereby providing a more stable characterisation of the haemodynamic environment (Mutlu et al. 2023).

In this study, TA-WSS distributions are prioritised over instantaneous WSS, as they provide a more reliable measure of shear exposure on the aneurysm wall. Unlike instantaneous WSS, which is highly sensitive to transient fluctuations, TA-WSS captures the sustained haemodynamic load experienced over the entire cardiac cycle. This cumulative exposure is more relevant to the mechanobiological pathways governing aneurysm progression and rupture, as outlined in the preceding WSS subsection.

### **2.1.3 Oscillatory Shear Index**

The Oscillatory Shear Index (OSI) is calculated from the WSS vector and quantifies the directional and temporal variability of blood flow, reflecting the degree to which flow patterns change throughout a cardiac cycle. A high OSI indicates unstable and oscillatory flow, whereas a low OSI suggests more laminar and stable flow (Machi et al. 2019).

According to Kim et al. (2021) higher OSI is observed in ruptured aneurysms and at rupture locations, suggesting that this oscillatory flow may contribute to wall weakening. However, the precise mechanisms by which oscillatory flow leads to rupture remain a subject of ongoing research, with some studies proposing that extremely low OSI or complex flow patterns are the cause (Wu and Zhu 2021).

### **2.1.4 Relative Residence Time**

Relative Residence Time (RRT) is a haemodynamic parameter that reflects the average duration blood is in close proximity to the arterial wall. It is inversely proportional to WSS, indicating that areas of low WSS typically correspond to regions of prolonged blood residence (Riccardello Jr et al. 2018).

RRT is mathematically defined as a function dependent on TA-WSS and OSI. The relationship between RRT and aneurysm rupture is complex and remains an area of ongoing research; at the time of writing, there are no established standard values for a normal range.

## 2.2 Mechanobiology of Aneurysms

The controversial nature of aneurysm mechanobiology emerged with the proposal of two competing hypotheses, the “High-flow” and “Low-flow” theories, both aiming to explain aneurysm behaviour. These theories, while both addressing aneurysm growth, stability, and eventual rupture, differ significantly in their interpretation of haemodynamic factors. The “High-flow” theory posits that elevated WSS plays a crucial role in aneurysm development and rupture, while the “Low-flow” theory suggests that low WSS and disturbed flow patterns are the primary drivers of these processes. Figure 2.1 provides a side-by-side comparison of these two theories, illustrating their contrasting hypotheses.

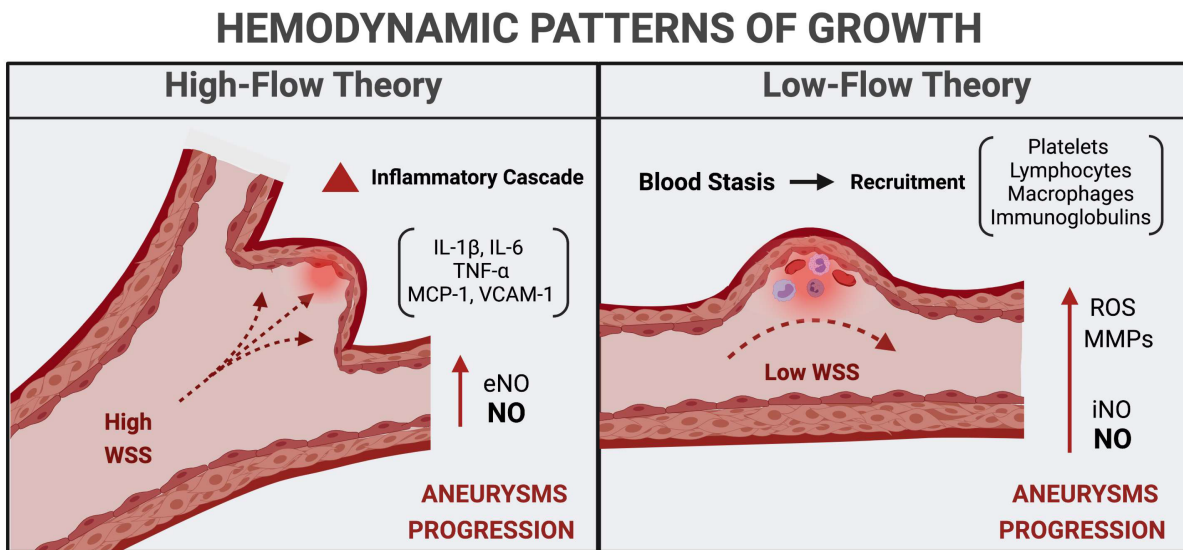


Figure 2.1: Illustration of High-Flow and Low-Flow Theories (Giotta Lucifer et al. 2021)

### 2.2.1 High-flow Theory

The “High-flow” theory in aneurysm mechanobiology centres on the hypothesis that elevated WSS is a key factor in the development and rupture of aneurysms (Friesen et al. 2021). This suggests that the increased frictional force exerted by rapidly flowing blood on the inner lining of the artery can initiate a cascade of events leading to vascular remodelling and weakening. High WSS is thought to cause direct injury to the endothelial cells that line the artery wall. This endothelial damage can trigger a biological response in the vessel wall, potentially leading to the degeneration of the internal elastic lamina, which is crucial for maintaining the structural integrity of the artery (Sforza, Putman, and Juan Raul Cebral 2009).

Hashimoto et al. (1987) found that animal testing has further supported this theory, demonstrating that exposure to hemodynamic stress associated with increased blood flow leads to degenerative changes in the arterial wall, immediately adjacent to the apex of bifurcation and aneurysm formation. These observations suggest a strong link between high WSS and the initial development of aneurysmal dilations.

Castro et al. (2006) has correlated high WSS with aneurysm growth in specific scenarios. For instance, when an inlet flow carrying high inertia enters the aneurysm sac, the dome of the aneurysm can be subjected to high WSS, potentially driving further growth. Moreover, areas of high WSS have been associated with the formation of multi-saccular aneurysms, indicating a localised weakening and remodelling process.

Sforza, Putman, and Juan Raul Cebral (2009) suggest rupture may occur at points of particularly high WSS, where the mechanical stress on the weakened wall exceeds its failure strength. These flow impingement zones are where the high-velocity inflow stream directly impacts the aneurysm wall, resulting in elevated WSS.

### **Key Findings**

The “High-flow” theory attributes the location of aneurysm rupture primarily to regions of maximum WSS. Although RRT is not directly mentioned in this theory, its inverse relationship with WSS means that areas with low RRT often correspond to regions of high WSS. Therefore, rupture-prone regions are to exhibit elevated WSS and TA-WSS, low OSI, and short RRT. In summary, the theory suggests that areas with elevated WSS, stable flow (low OSI), and short blood residence (low RRT) are critical indicators of potential rupture sites.

### **Literature Gaps**

At the time of writing, there are no established threshold values for “high” WSS. As a result, terms such as “elevated” WSS are used in a relative comparison to the surrounding regions of the aneurysm sac, instead of standardised benchmarks.

A further limitation in the literature is the tendency to evaluate WSS in isolation. Past simulations tend to adopt a single-parameter approach, dismissing the interplay between other haemodynamic parameters (OSI and RRT).

Lastly, there are few instances where in-vitro or clinical data have successfully validated in-silico predictions based on high flow theories. The lack of correlation between computational models and observed rupture locations results in a significant uncertainty into the applicability of high flow based rupture predictions.

## 2.2.2 Low-Flow Theory

In contrast, the more recent “low-flow” theory in aneurysm mechanobiology proposes that low WSS and disturbed flow patterns within the aneurysm sac are key contributors to aneurysm growth and eventual rupture Sforza, Putman, and Juan Raul Cebal (2009). This theory suggests that regions of stagnant, slow-moving blood initiate a different biological cascade, where low WSS induces endothelial dysfunction, which promotes inflammation and ultimately compromises the structural integrity of the aneurysm wall.

According to Kumar and Kumar (2023), regions exposed to low WSS tend to exhibit accelerated growth and are more susceptible to rupture than regions experiencing elevated WSS. These low-WSS regions are commonly observed at the apex or tip of the aneurysm, corresponding to regions of wall thinning.

Frösen et al. (2019) reported that low WSS promotes endothelial cell loss and enhances the pro-inflammatory response within the aneurysm. This inflammatory state is associated with the release of enzymes that degrade the extracellular matrix, further weakening the vessel wall and increasing rupture risk.

Kelsey et al. (2017) added that low WSS can also facilitate the formation of intraluminal thrombus. While thrombus formation may initially buffer the mechanical load on the wall, it also serves as a source of inflammatory cytokines and growth factors, which can exacerbate wall degradation.

### Key Findings

The low-flow theory attributes the location of aneurysm rupture to areas of low WSS, typically located at the dome or apex of the aneurysm. Regions of low WSS are often accompanied by disturbed and fluctuating flow (high OSI) and stagnant, slow-moving flow (high RRT) (Terada et al. 2016). The theory employs a different mechanobiological pathway for aneurysm progression and rupture, characterised by endothelial dysfunction and inflammatory action.

### Literature Gaps

Similarly to the high-flow theory, there is no defined threshold for what is classified as “low” WSS. The term is used in a comparative sense to the surrounding regions within the aneurysm sac, which makes standardisation difficult.

Additionally, previous studies have often examined WSS independently, without accounting for the interplay between other key haemodynamic parameters (OSI and RRT).

### 2.2.3 Current Perspective

It is widely recognised that biological phenomena rarely follow a straightforward cause-and-effect relationship (Mayr 1961). Instead, aneurysm formation and rupture are understood to arise from an interplay of multiple factors. The fundamental distinction between the high-flow and low-flow theories is the proposed mechanism of vascular wall weakening. The high-flow theory attributes rupture to mechanical injury caused by elevated WSS, whereas the low-flow theory emphasises biological degradation resulting from flow stagnation and inflammation (Sforza, Putman, and Juan R Cebral 2012).

Meng et al. (2014) demonstrated that the high-flow theory is typically associated with the formation of type I aneurysms, which tend to be smaller and fusiform in shape. In contrast, type II aneurysms which are characterised by their larger, saccular morphology tend to be more commonly linked with the low-flow theory (Keedy 2006). Figure 2.2 presents a visual comparison of these two theoretical frameworks and their associated aneurysm classifications.

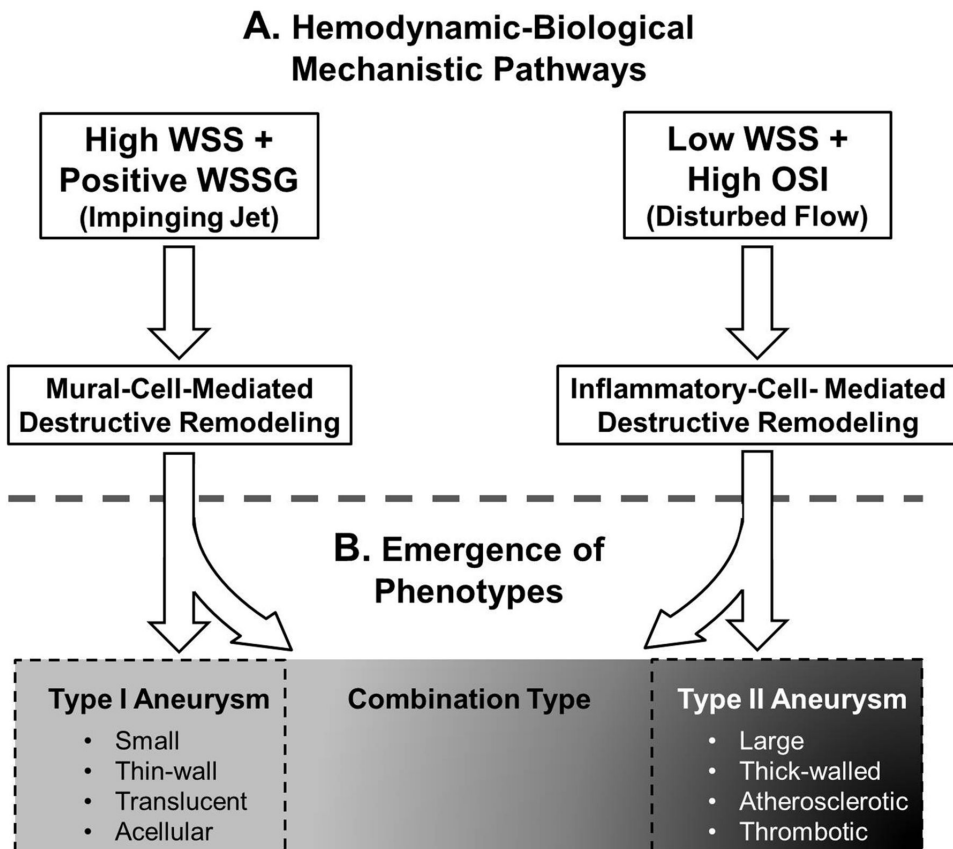


Figure 2.2: Comparison between high-flow and low-flow theories(Meng et al. 2014)

Past CFD studies recognise that both high-flow and low-flow theories hold true in explaining aneurysm rupture mechanisms. However, findings from the 2013 CFD Rupture Challenge indicate that low-flow-based parameters offer stronger predictive performance. Teams that employed metrics consistent with the low-flow theory (as summarised in Table 2.2) were able to localise rupture sites with an accuracy of approximately  $\pm 5$  mm, while approaches based on high-flow theory demonstrated greater uncertainty in their predictions (Janiga et al. 2015).

No. of Parameters	Parameter	No. of Groups
1	Low (TA)WSS	6
	High (TA)WSS	3
	High pressure	1
	Maximum velocity	1
2	Low (TA)WSS, high pressure	3
	Low (TA)WSS, high OSI	3
	High (TA)WSS, pressure gradient	2
	Low TAWSS, complex flow	1
	High TAWSS, complex flow	1
3	High TAWSS, direct impingement	1
	Low TAWSS, high OSI, high RRT	1
	TAWSS distribution, complex flow, flow diversion	1
	Direct impingement, pressure gradient, high WSS	1

Table 2.2: Haemodynamic parameters used to predict rupture sites after selection of ruptured cases (Janiga et al. 2015)

Consequently, this dissertation adopts the low-flow theory as its primary framework, due to its stronger alignment with *in-vitro* and clinical rupture data and its relevance to the patient-specific aneurysms investigated, which display a saccular morphology consistent with type II aneurysm classification.

In addition, this study employs a three-parameter approach to capture the essential interplay between haemodynamic indicators. Specifically, regions characterised by low TA-WSS, elevated OSI, and prolonged RRT are attributed to rupture-prone regions within the aneurysm.

## 2.3 Star-CCM+ Meshing

The choice of mesh type significantly impacts the accuracy, stability, and computational cost of the simulation. Among the various meshing techniques available in commercial CFD software like Star-CCM+, polyhedral and tetrahedral meshes are commonly employed for complex geometries. This section aims to provide a comprehensive comparison of these two mesh types within the context of Star-CCM+, with a specific focus on the advantages of employing polyhedral meshes for the simulation of blood flow in aneurysms.

### 2.3.1 Tetrahedral Meshes

Tetrahedral elements are composed of four triangular faces and are highly adaptable to intricate geometries due to their geometric simplicity. This makes them a common choice for unstructured meshing, particularly where the domain exhibits high curvature or irregularity (Sosnowski et al. 2018). Tetrahedral meshes are generated directly from the geometry, their ease of generation and suitability for arbitrary shapes makes them efficient for initial mesh creation. However, their relatively low number of neighbouring cells limits their ability to accurately capture flow gradients (Zhang et al. 2020).

### 2.3.2 Polyhedral Meshes

Polyhedral meshes consist of cells with an average of 14–16 faces, derived via dualisation from an initial tetrahedral mesh (Kulkarni 2023). This higher face count increases the number of neighbouring cells, typically around 10 per element, enhancing the approximation of velocity gradients and improving numerical stability (Pougatch and Weiss 2021). The enhanced connectivity also facilitates better convergence characteristics and reduced numerical diffusion, particularly beneficial in simulations involving multidirectional or vortical flow fields.

Karakas et al. (2013) showed that polyhedral meshes can achieve similar or improved solution accuracy with significantly fewer cells compared to tetrahedral meshes. This reduction not only decreases memory requirements and solver time, but also supports the feasibility of high-resolution simulations in clinical or resource-limited settings.

## 2.4 Mesh Suitability for Aneurysm Simulation

The irregular and patient-specific geometries of intracranial aneurysms make unstructured meshing approaches essential. While hexahedral meshes offer low numerical diffusion, their generation for complex anatomical structures is impractical (Pougatch and Weiss 2021). Tetrahedral and polyhedral meshes, therefore, are better suited to vascular domains. Importantly, polyhedral meshes provide a good balance between geometric flexibility and computational performance. Their superior accuracy in capturing WSS has been demonstrated across several studies (Spiegel et al. 2011).

Additionally, polyhedral cells exhibit lower sensitivity to stretching and maintain mesh quality more effectively than tetrahedra, which can be prone to high skewness under deformation (Sosnowski et al. 2018). Their robustness allows them to resolve flow features near boundaries when used alongside prism layers for accurate boundary layer resolution.

### Key Findings

The choice of mesh type plays a pivotal role in CFD simulations of blood flow in aneurysms. While tetrahedral meshes are straightforward to generate and suitable for complex domains, polyhedral meshes offer distinct advantages in terms of gradient resolution, convergence, and computational efficiency. Owing to their ability to reduce numerical diffusion, better capture haemodynamic variables such as WSS, and lower overall cell counts. As a result, polyhedral meshing was selected for this study to ensure accurate and computationally efficient simulations of aneurysmal blood flow. Figure 2.3 illustrates the polyhedral mesh cell configuration employed for this study.

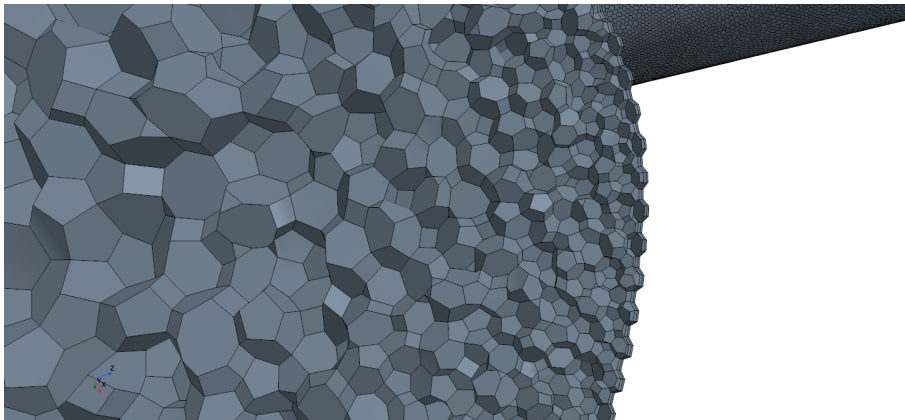


Figure 2.3: Polyhedral Mesh

# Chapter 3

## Methodology

The study uses two patient-specific aneurysms, labelled case 1 and case 2, these cases were provided by S. Sugiyama in The CFD Rupture Challenge 2013. Both aneurysms were located at the left M1 segment and exhibited similar geometric properties. This chapter will describe the methodology for extracting geometry from DICOM data, the meshing process in STAR-CCM+, and the subsequent CFD analysis. A workflow diagram is shown in Figure 3.1.

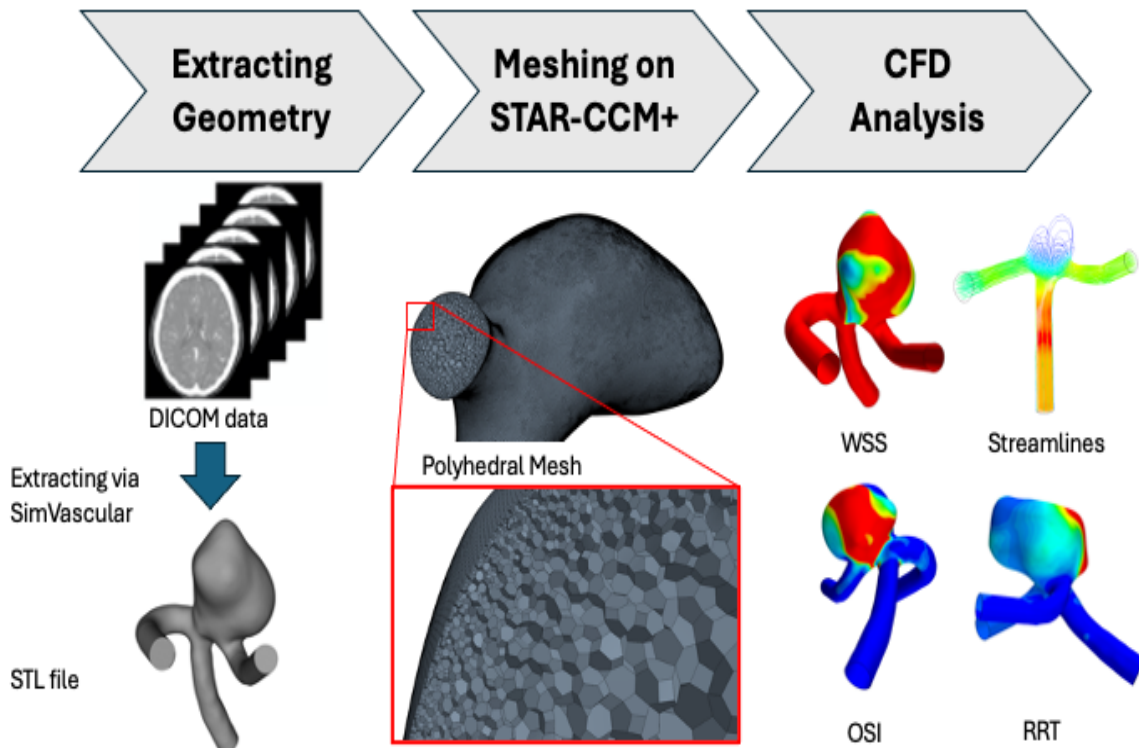


Figure 3.1: Methodology Workflow

## 3.1 CFD Modelling

### 3.1.1 CFD Model Development: SimVascular

The aneurysm geometries employed in the CFD simulations were generated using Magnetic Resonance Angiography (MRA) imaging data. Patient-specific imaging files obtained in Digital Imaging and Communications in Medicine (DICOM) format were imported into SimVascular, an open-source biomedical simulation software package (Wilson et al. 2001).

Within SimVascular, a three-dimensional vessel geometry was reconstructed using a clearly defined workflow. Initially, a path corresponding to the centreline of the aneurysm was established based on the imported imaging data. Subsequently, multiple two-dimensional contours were delineated manually along this path at regular intervals. Each contour traced the boundaries of the vessel lumen, capturing the complex variations and the detailed morphology of the aneurysm.

These sequential contours were interpolated within SimVascular, resulting in a coherent three-dimensional geometric representation of the aneurysm. The resultant model, capturing the unique anatomical structure of each aneurysm case, was then exported as a stereolithography (STL) file. This STL file served as the geometrical basis for subsequent CFD analyses. An illustration of this geometric reconstruction workflow can be found in Figure 3.2.

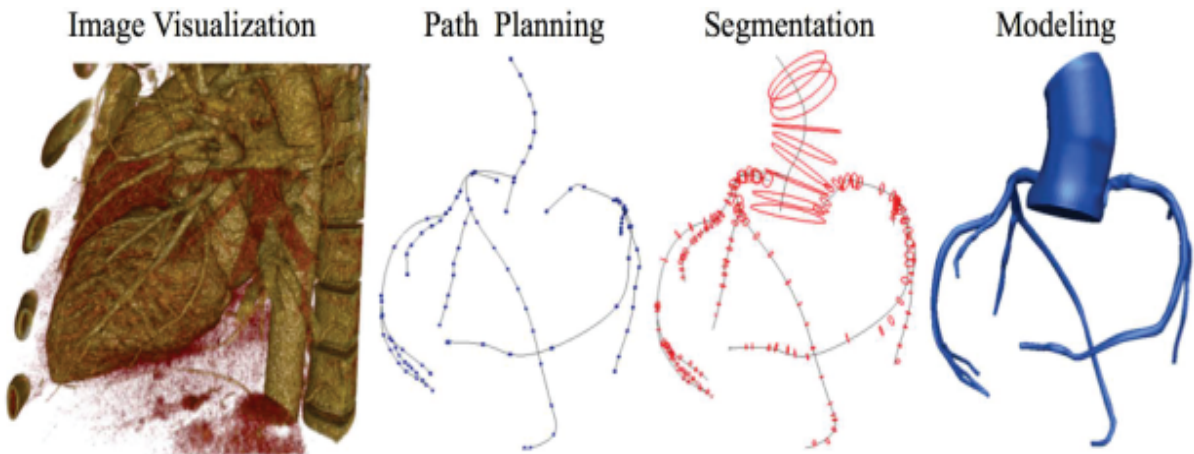


Figure 3.2: Image visualisation to modelling on SimVascular (Lan et al. 2018)

### 3.1.2 Mesh Generation: STAR-CCM+

The geometrical models developed in SimVascular (Section 3.2.1) were imported into Simcenter STAR-CCM+ 2402 (Build 19.02.009) for mesh generation. Initially, each imported surface mesh was inspected using the STAR-CCM+ surface repair toolkit to identify and correct potential issues such as intersecting surfaces, non-manifold edges, and surface irregularities. This step ensured the generation of a clean and CFD compatible geometric model.

For this study, polyhedral meshing techniques were employed due to their proven robustness and capability to accurately capture complex geometries characteristic of intracranial aneurysms. Polyhedral meshes offer distinct advantages over tetrahedral counterparts, notably reduced numerical diffusion, improved convergence properties, and enhanced cell quality. These advantages directly contribute to more accurate simulations of haemodynamic parameters, such as wall shear stress (WSS), oscillatory shear index (OSI), and relative residence time (RRT).

A strategic mesh refinement approach was implemented, involving boundary layer refinement close to aneurysm walls to accurately resolve near-wall flow phenomena and high-gradient regions. Additionally, targeted volumetric refinement was implemented around the endovascular intervention devices (flow diversion stents or coils) to accurately capture complex flow dynamics and vortical structures essential for detailed haemodynamic analysis. Mesh quality was assessed using metrics such as skewness, orthogonality, and aspect ratio, ensuring that all generated meshes conformed to accepted standards for clinical haemodynamics simulations.

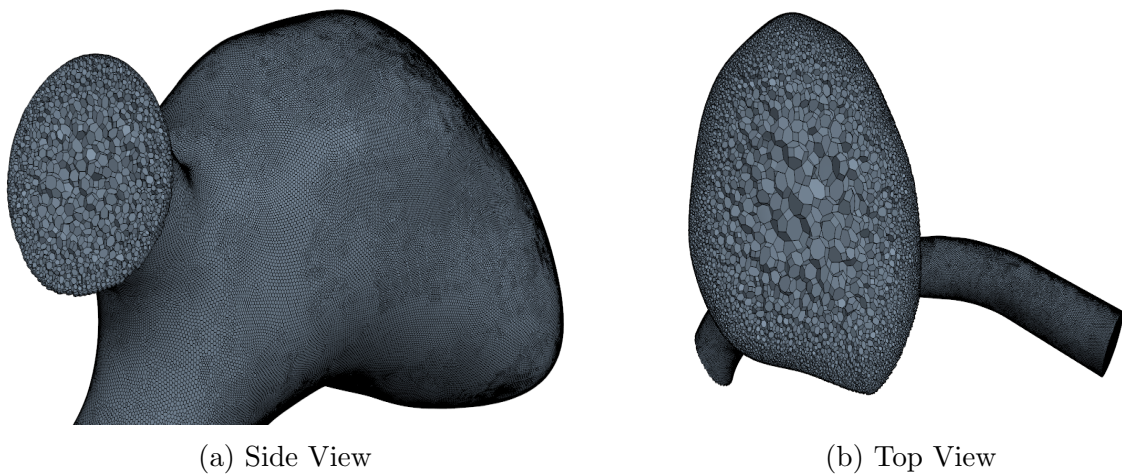


Figure 3.3: Polyhedral mesh cell set for case 1

Additionally, the prism layer mesher was enabled with a first layer thickness set to 33.33% of the base size, generating near-wall inflation layers critical for resolving boundary layer flows. This setup contributed to the generation of an unstructured polyhedral mesh, as shown in Figure 3.3, with targeted refinement in the near-wall regions of the aneurysm sac. These regions are of particular interest due to their direct influence on key haemodynamic parameters such as wall shear stress and oscillatory shear index.

### 3.1.3 Grid Independence

The grid independence study was conducted based on the methodology proposed by Dr. A. Revel and Dr. A. Phase (2013), with modifications tailored to this study's inclusion of endovascular treatments. To determine grid independence, four distinct mesh resolutions were generated by systematically varying the base cell size, resulting in differing cell counts as summarised in Table 3.1.

Name	Base Size [m]	Case 1 Number of Cells	Case 2 Number of Cells
Coarse Polyhedral	0.2	77,916	76,524
Medium Polyhedral	0.1	270,017	251,125
Fine Polyhedral	0.05	1,121,260	1,040,010
Very Fine Polyhedral	0.025	4,576,303	4,275,800

Table 3.1: Mesh resolution and corresponding number of cells

Once the mesh was successfully generated, grid independence was assessed by evaluating velocity and pressure at predefined monitoring points for both Case 1 and Case 2, as illustrated in Figure 3.4. To ensure computational efficiency whilst maintaining physiological relevance, the independence study was conducted using a steady-state inlet velocity profile of 0.65 m/s. This velocity was chosen as it represents the average blood flow velocity typically observed throughout a cardiac cycle (Holdsworth et al. 1999).

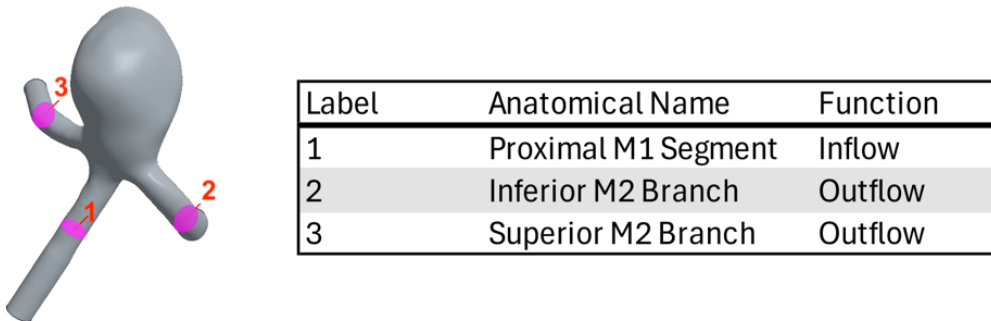
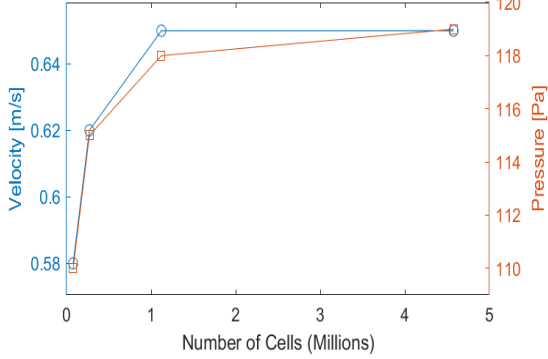
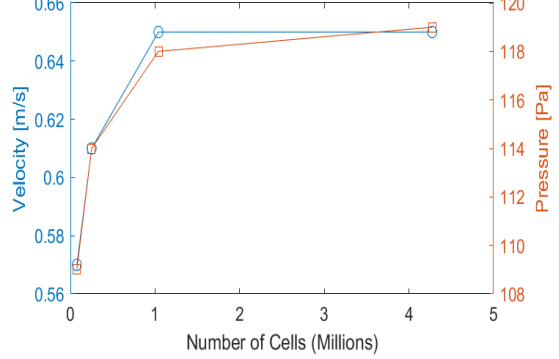


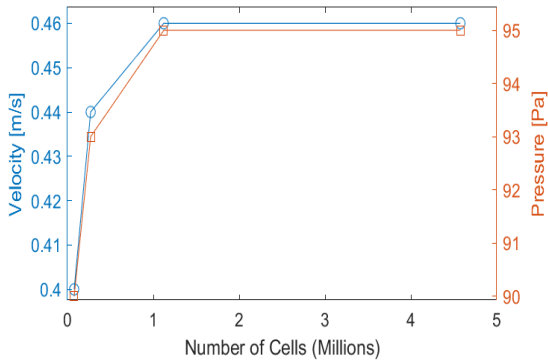
Figure 3.4: Cross-sectional planes along case 1 for pressure and velocity analysis.



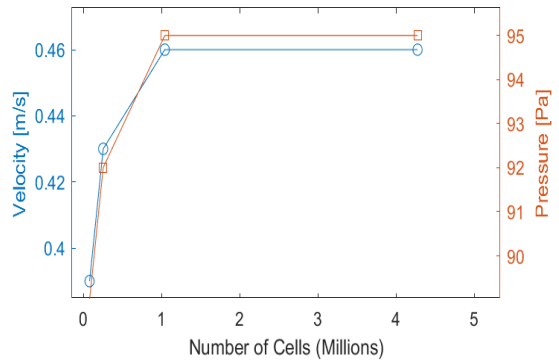
(a) Case 1: Proximal M1 Segment



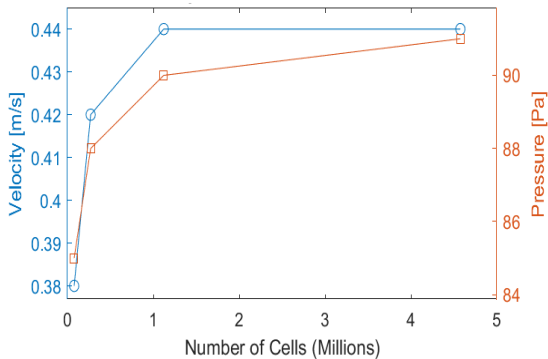
(b) Case 2: Proximal M1 Segment



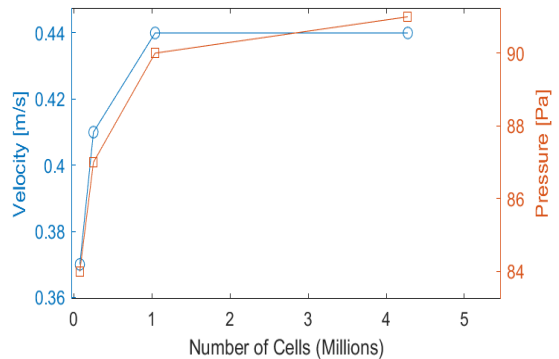
(c) Case 1: Inferior M2 Branch



(d) Case 2: Inferior M2 Branch



(e) Case 1: Superior M2 Branch



(f) Case 2: Superior M2 Branch

Figure 3.5: Grid independence plots comparing Case 1 and Case 2

The outcomes of the grid independence study are presented in Figure 3.5. Analysis of the data clearly indicates that a mesh resolution with *circa* 0.8 million cells provides sufficient accuracy to achieve grid independence. However, considering the additional geometric complexities introduced by including stents and coils in certain simulations, it was determined that a target mesh resolution of *circa* 1.0 million cells would be preferable. Consequently, a base cell size of 0.05 m, as detailed in Table 3.1, was ultimately selected for this study, resulting in 1,121,260 and 1,040,010 cells for case 1 and 2 respectively.

A preview of the meshes used can be found in Appendix C.

### 3.1.4 Boundary Conditions

Boundary conditions were clearly defined by splitting the computational model using the part-surface tool to generate the regions required for subsequent processing stages. These regions included one inlet, two outlets, the vessel wall, and, where applicable internal boundaries corresponding to the surfaces of implanted stents or coils, as illustrated in Figure 3.6

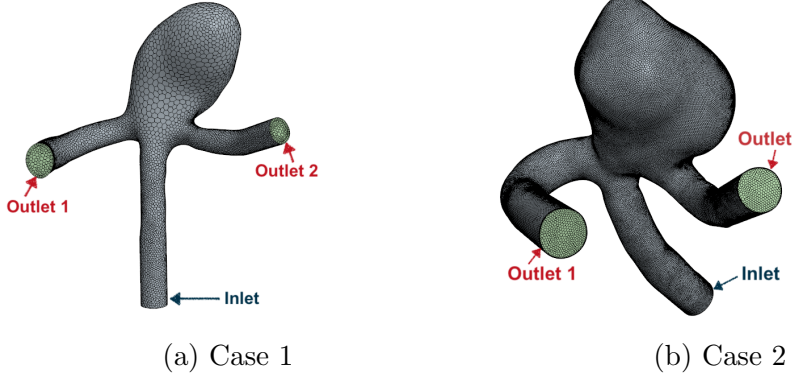


Figure 3.6: Boundary Conditions of IA

**Inlet Conditions:** At the inlet boundary, a uniform pulsatile velocity profile was employed, reflecting typical blood flow conditions within intracranial arteries. The velocity waveform, obtained from clinical literature, accurately represented the haemodynamics of a cardiac cycle, capturing peak systolic velocity ( $V_{\max} = 1.082 \text{ m/s}$ ), minimum diastolic velocity ( $V_{\min} = 0.194 \text{ m/s}$ ), and cycle-averaged peak velocity ( $\bar{V} = 0.388 \text{ m/s}$ ) (Holdsworth et al. 1999). The temporal velocity variation was implemented through a time-resolved dataset in .csv format, which provided discrete velocity values across the duration of the cardiac cycle. A spline interpolation was applied to these data points to generate a smooth, continuous waveform, the resulting inlet waveform used in the simulation is illustrated in Figure 3.7.

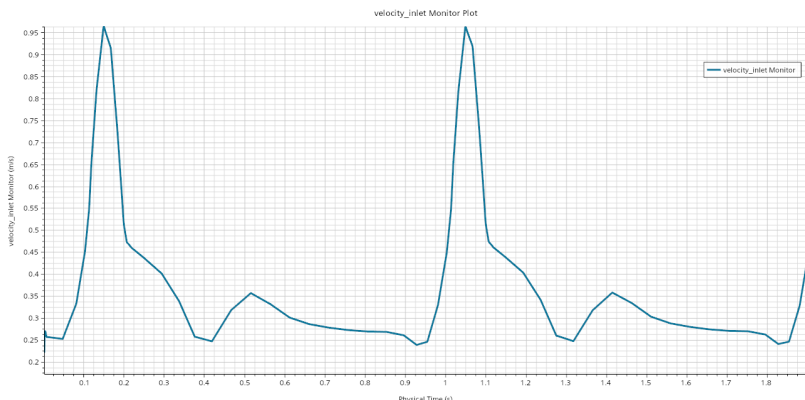


Figure 3.7: Inlet velocity monitor plot

**Outlet Conditions:** For both outlet boundaries, outlet conditions were employed, specifying the mass flow split ratio as 0.5 between the outlets. This approach results in an equal distribution of flow between two outlets and allows for appropriate physiological responses of flow splitting based on downstream arterial resistances, consistent with established CFD aneurysm models in literature (Shimano et al. 2019).

**Wall Boundary Conditions:** All vessel walls were defined with no-slip boundary conditions, assuming rigid walls for simplicity and computational efficiency. This assumption is commonly validated in CFD studies of intracranial aneurysms, given the negligible wall motion of cerebral vessels compared to major systemic arteries (Castro et al. 2006).

**Stent and Coil Surfaces:** In cases involving endovascular devices, surfaces were similarly modelled with no-slip boundary conditions to accurately represent realistic fluid-device interactions and flow disturbances introduced by these devices.

**Flow Regime and Turbulence Modelling:** Considering the relatively low Reynolds numbers typically observed in intracranial arteries ( $Re < 2,300$ ), the flow was assumed to be an incompressible laminar flow for all simulations conducted in this study. This assumption is justified by the negligible influence of turbulence, attributed to the low flow velocities and small vessel diameters (Rahma and Abdelhamid 2023).

### 3.1.5 Physics Continuum

A custom fluid continuum model was defined to represent blood. The flow was assumed to be incompressible, laminar, and Newtonian, with a constant density  $\rho = 1000 \text{ kg} \cdot \text{m}^{-3}$  and dynamic viscosity  $\mu = 0.004 \text{ kg} \cdot \text{m}^{-1} \cdot \text{s}^{-1}$ , based on literature values (Rand et al. 1964). The model was configured for three-dimensional flow, employing a second order segregated solver approach. Additionally, the gradient model was enabled to improve spatial accuracy in regions of complex flow.

### 3.1.6 Solver Settings

An implicit, unsteady solver was employed to capture the transient nature of blood flow. A segregated flow solver was used to separately compute the velocity and pressure fields. The simulation was run for a total physical time of 1.9 seconds—approximately two cardiac cycles—divided into 1900 timesteps of 0.001 seconds. Each timestep included 10 inner iterations to ensure convergence. Stopping criteria were based on the stabilisation of monitored haemodynamic parameters such as TA-WSS and OSI.

## 3.2 Haemodynamic Parameters

The following haemodynamic parameters were defined using custom user-defined field functions via the Automation Toolbox in STAR-CCM+. The definitions of these field functions are detailed in Appendix D.

### 3.2.1 Wall Shear Stress (WSS)

Defined as the tangential force per unit area exerted by blood flow on the inner surface of the vessel wall. It plays a critical role in aneurysm formations and is foundational to several secondary haemodynamic metrics discussed in later sections.

Mathematically, WSS is defined as:

$$\text{WSS} = \tau_w = \mu \left( \frac{\partial u}{\partial n} \right)_{\text{wall}} \quad (3.1)$$

Where:

- $\tau_w$  is the wall shear stress (Pa)
- $\mu$  is the dynamic viscosity of blood ( $0.004 \text{ kg} \cdot \text{m}^{-1} \cdot \text{s}^{-1}$ )
- $u$  is the velocity component tangential to the wall
- $n$  is the direction normal to the vessel wall

### 3.2.2 Time-Averaged Wall Shear Stress (TA-WSS)

Defined as the wall shear stress averaged over the duration of a cardiac cycle. This parameter helps to reduce the influence of short-term fluctuations and transient effects, thereby offering a more stable representation of the shear environment experienced by the vessel wall.

According to the low-flow theory employed in this study, regions exhibiting low TA-WSS are considered more susceptible to rupture compared to areas with higher TA-WSS, as discussed in the literature review (Section 2.1.2).

Mathematically, TA-WSS is expressed as:

$$\text{TA-WSS} = \frac{1}{T} \int_0^T |\text{WSS}| dt \quad (3.2)$$

Where:

- TA-WSS is the time-averaged wall shear stress (Pa)
- WSS is the instantaneous wall shear stress at time  $t$  (Pa)
- $T$  is the duration of the cardiac cycle (s)

### 3.2.3 Oscillatory Shear Index (OSI)

A non-dimensional parameter used to quantify the directional change of wall shear stress (WSS) over a cardiac cycle. It showcases the degree of oscillation and disturbance in the flow near the wall.

OSI takes values in the range of 0 to 0.5, an OSI of 0 indicates purely unidirectional flow, where the WSS vector does not reverse direction. On the other hand, an OSI value of 0.5 corresponds to fully oscillatory flow, where the shear stress is equal in magnitude but opposite in direction over the cycle, leading to net zero directional shear. According to the low-flow theory, regions exposed to elevated OSI are more susceptible to rupture.

Mathematically, OSI is defined as:

$$\text{OSI} = \frac{1}{2} \left( 1 - \frac{\left| \int_0^T \text{WSS} dt \right|}{\int_0^T |\text{WSS}| dt} \right) \quad (3.3)$$

Where:

- OSI is the Oscillatory Shear Index (dimensionless)
- WSS is the instantaneous wall shear stress vector at time  $t$  (Pa)
- $T$  is the duration of the cardiac cycle (s)
- $|\cdot|$  denotes the magnitude of a vector

### 3.2.4 Relative Residence Time (RRT)

Defined as a haemodynamic index that quantifies the residence time of blood particles near the vessel wall, providing an indication of regions susceptible to stagnation. RRT reflects how long blood spends inside the aneurysm sac.

This index is derived from the aforementioned TA-WSS and OSI. Elevated values of RRT are indicative of stagnant or disturbed flow. According to the low-flow theory, regions with high RRT are more susceptible to rupture.

Mathematically, RRT is defined as:

$$RRT = \frac{1}{(1 - OSI) \cdot TA-WSS} \quad (3.4)$$

where:

- RRT is the Relative Residence Time ( $\text{Pa}^{-1}$ )
- TA-WSS is the time-averaged wall shear stress (Pa)
- OSI is the Oscillatory Shear Index (dimensionless)

## 3.3 Simulation of Endovascular Treatments

The introduction of endovascular treatments has led to the development of novel features that are of significant biological interest. Specifically, these treatments involved the use of flow diversion stents or endovascular coils, tailored for patient-specific cases 1 and 2.

### 3.3.1 Flow Diversion Stents

The flow diversion stent was designed using computer aided design (CAD) software, SOLIDWORKS. The design process incorporated dimensions and material properties from the Medtronic Pipeline Flex device. An accurate CAD model was created, tailored to the unique characteristics of the patient's aneurysm. This model was then exported from a .SLDPRT file to a .STL file format.

Using Blender and MeshLab, the stent was positioned at the neck of the aneurysm to effectively divert blood flow away from the sac and for accurate integration into simulation environments. Finally, a Boolean subtraction operation was performed to create the final .STL file, which was subsequently used in the simulation process. The resultant stent and its placement can be seen in Figure 3.8.

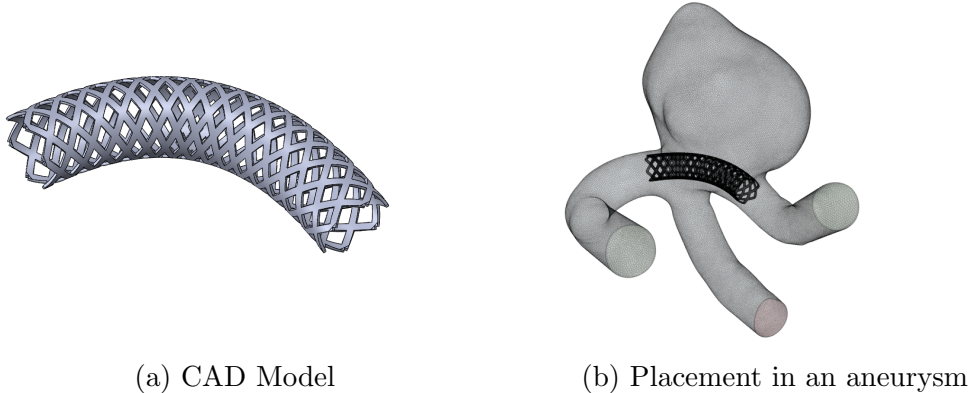


Figure 3.8: Flow Diversion Stents

### 3.3.2 Endovascular Coiling

The process for modelling the endovascular coil closely followed the workflow used for the flow diversion stents. The CAD model of the coil was developed by incorporating the material properties and dimensions from the Stryker Target Detachable Coil series. The model was tailored to fit the unique geometry of the aneurysm's neck and sac. Once the CAD model was finalised, it was transferred to Blender for further processing, where a Boolean subtraction operation was performed to create the final mesh. The resulting .STL file was then prepared for use in subsequent simulations and analyses, and can be seen in Figure 3.9.

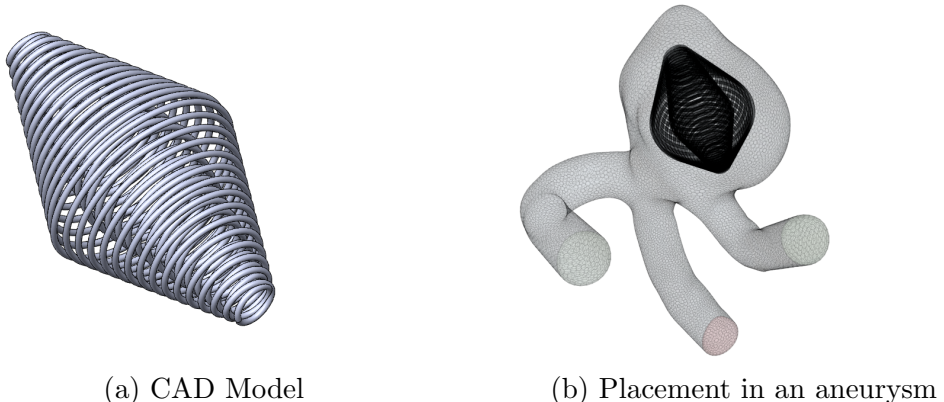


Figure 3.9: Endovascular Coiling

## 3.4 Model Validation and Verification

The validation of untreated aneurysm simulations was conducted using extensive benchmark data from the 2013 CFD challenge. This challenge provided a comparison of various simulation models, offering valuable insights into the most accurate and stable simulations (Janiga et al. 2015). This study closely mirrors those simulations established as the most reliable from the CFD challenge.

In addition to this benchmark validation, the aneurysm model with the highest rupture risk was verified using in-vitro data. Patient-specific aneurysms were monitored over a span of two years using regular MRA scans, with the precise location of rupture recorded. This clinical data proved essential in verifying the simulation model.

Due to the novelty of this study, there is no available data (either in-vitro or in-silico) of aneurysms treated with endovascular techniques at the time of writing. However, this gap in data was mitigated by using the same validated models applied to the untreated aneurysms. Ensuring consistency in model validation and verification of the novel scenarios.

## 3.5 Replicability and Transparency

To ensure project replicability, and due to the repeatable nature of this project, several JavaScript macros were developed to automate key tasks in the pre-processing and post-processing phases. These macros significantly reduced the time required for setting up the simulations, ensuring both efficiency and consistency. The full set of macros, along with detailed instructions on their usage, is available on the author's GitHub repository: [GitHub Macro Repository Link](#).

In addition, to ensure full transparency and reproducibility, all CAD models, including those for the patient-specific aneurysms, flow diversion stents, and endovascular coils, along with all relevant simulation files, are openly available. These files can be accessed through the following GitHub repository: [GitHub CAD and Sim Repository Link](#).

A preview of the repository structure and contents can be found in Appendix E, where additional details about the files and organisation are provided.

## **3.6 Limitations and Justifications**

### **3.6.1 Rigid body: Fluid structure interaction**

An aneurysm is a soft body, undergoing expansion and contraction throughout the course of the cardiac cycle. However, in this study, the aneurysm was treated as a rigid body for computational efficiency. The motion of the aneurysm sac during the cardiac cycle is negligible compared to its recovery time. The decision to adopt a rigid body model is supported by prior studies, which demonstrated that vessel wall motion has minimal impact on flow dynamics in cerebral aneurysms, given their relatively low wall motion compared to major systemic arteries (Castro et al. 2006).

However, it should be noted that this study does not account for the potential shrinkage of the aneurysm sac following the implementation of endovascular treatments, which at the time of writing, is an area of ongoing research.

The rigid body assumption helps reduce computational time without compromising the accuracy of the results, particularly as the focus of the study is on haemodynamic parameters rather than the motion of the aneurysm.

### **3.6.2 Blood Flow**

Recent studies have suggested that blood flow within the aneurysmal sac may exhibit characteristics similar to turbulent flow, particularly due to mixing in the flow dynamics (Ferguson 1970). Furthermore, the interaction between the endovascular devices and the blood may induce additional flow disturbances, which could cause localised turbulent behaviour. Despite these theoretical findings, there is currently no definitive evidence supporting the turbulent nature of blood flow in aneurysms. Therefore, in this study, blood flow was assumed to be laminar, as is typical in studies of aneurysms where Reynolds numbers are low and flow remains predominantly smooth.

### **3.6.3 Cardiac Cycle**

The pulsatile, unsteady velocity profile employed in this study represents an averaged cardiac cycle. Unfortunately, patient-specific cardiac cycle data were not available, and as such, it was not possible to personalise the inflow conditions. Instead, a representative velocity profile, reflective of typical blood flow in healthy individuals, was utilised.

# Chapter 4

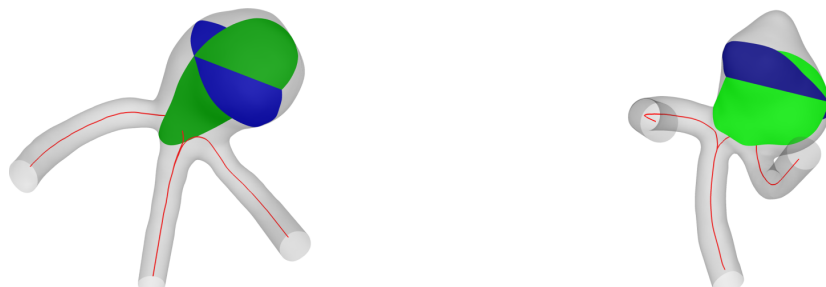
## Results and Discussion

## Introduction

The chapter is structured as follows:

- Section 1: Case 1
  - Section 2: Case 2
  - Section 3: Case 1 treated with a flow diversion stent
  - Section 4: Case 2 treated with a flow diversion stent
  - Section 5: Case 1 treated with endovascular coiling
  - Section 6: Case 2 treated with endovascular coiling

Each section presents detailed visualisations of key haemodynamic parameters (TA-WSS, OSI, RRT), with views arranged according to a 3D diagram flow. In addition, supporting views of streamlines, pressure contours, and velocity contours are provided to illustrate the motion of blood inside the aneurysm. Figure 4.1 illustrates streamlines generated from a 15x15 seed at the inlet (depicted in red), while pressure and velocity contours are visualised on the horizontal (blue) and vertical (green) planes. Additional views emphasise key areas of interest, which will be quantitatively compared to evaluate the impact and effectiveness of the treatments.



(a) Case 1 (b) Case 2  
Figure 4.1: Planes and Streamlines (Janiga et al. 2015)

## 4.1 Case 1

### 4.1.1 TA-WSS

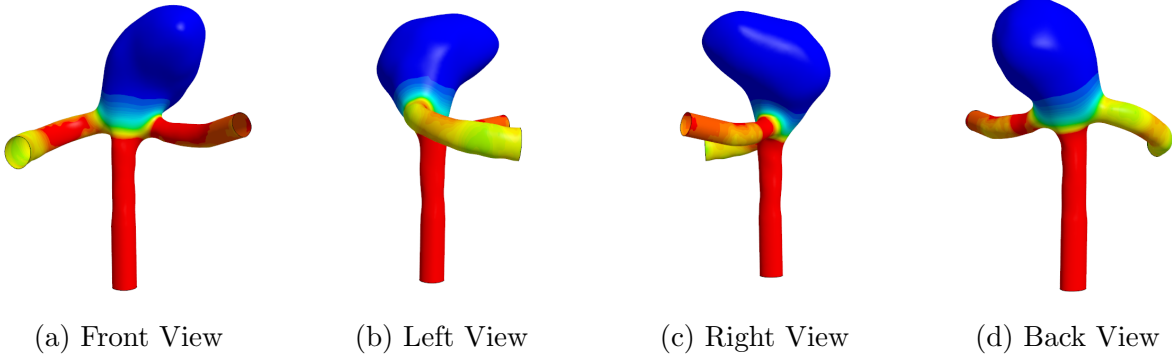


Figure 4.2: 3D diagram of TA-WSS for case 1

Figure 4.2 illustrates the TA-WSS, where the blue areas indicate low TA-WSS ( $< 0.125$  Pa), and the red areas indicate elevated TA-WSS ( $> 0.25$  Pa). Elevated TA-WSS values are observed at the inlet section and outlet branches, likely due to the undisturbed higher flow velocities in these regions. Notably, the right (M2 superior) branch experiences higher TA-WSS compared to the left (M2 inferior) branch. This is a result of the right branch being more closely aligned to the M1 segment (inlet), allowing for a more direct flow path, which increases the shear stress at the wall.

According to the low-flow theory applied in this study, areas of low TA-WSS are considered more prone to rupture due to the stagnant and recirculating flow that characterises these regions. The primary area of concern is the aneurysm sac, which displays a blue hue. The steep gradient at the neck of the aneurysm suggests a transition from a dynamic flow at the vessel neck to a stagnant flow within the sac. The lowest recorded value of TA-WSS is located along the vertical plane, as indicated by the black circle in Figure 4.3.

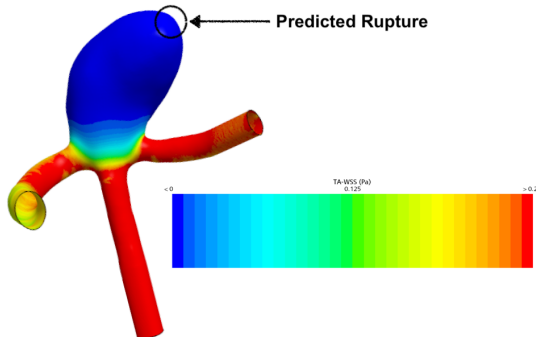


Figure 4.3: Detailed TA-WSS for case 1

#### 4.1.2 OSI

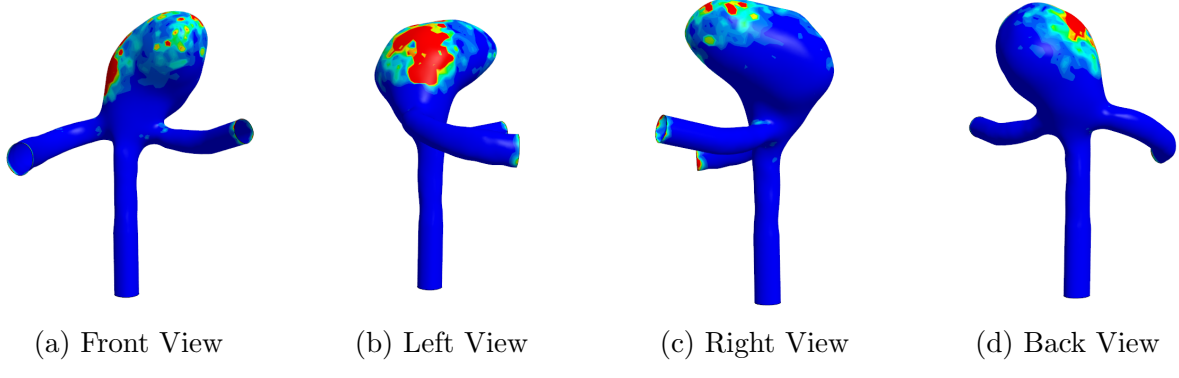


Figure 4.4: 3D diagram of OSI for case 1

Figure 4.4 showcases the OSI for case 1, with blue regions representing very low OSI values ( $< 0.0025$ ), and red regions indicating slightly elevated OSI values ( $> 0.005$ ). The low OSI values observed are a result of the laminar flow model used in this study, which leads to stabilised flow throughout the aneurysm. Despite the pulsating nature of the cardiac cycle, this stabilised flow suggests minimal turbulence within the aneurysm. The OSI gradient is less pronounced than that seen in TA-WSS, indicating a smoother and more gradual transition. It also suggests that the flow at the right side of the aneurysm sac is stagnant, with restricted movement.

According to the low flow theory employed, areas of elevated OSI are more prone to rupture. A prominent localised disturbance is observed at the right side of the aneurysm, resulting in comparatively high OSI values of 0.0604. This disturbance helps to accurately predict the rupture location in case 1, which is along the horizontal plane and towards the right of the sac, as illustrated by the black circle in Figure 4.5.

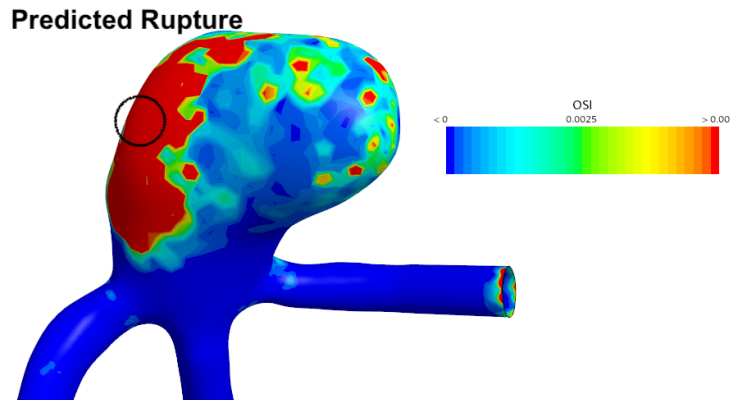


Figure 4.5: Detailed OSI for case 1

### 4.1.3 RRT

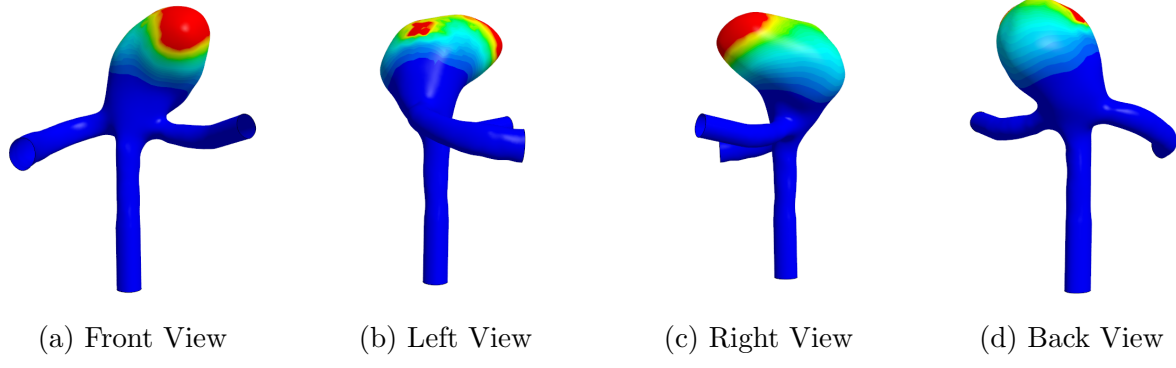


Figure 4.6: 3D diagram of RRT for case 1

Figure 4.6 illustrates the RRT for case 1, which mirrors the TA-WSS plots, with elevated areas of RRT concentrated towards the tip of the aneurysm. Blue regions at the neck of the aneurysm indicate low RRT values ( $< 125 \text{ kPa}^{-1}$ ), suggesting a short residence time with the flow moving freely. In contrast, the red regions in the sac of the aneurysm show elevated RRT values ( $> 250 \text{ kPa}^{-1}$ ), indicating slow-moving flow with extended contact time against the vessel wall. According to the low-flow theory, high RRT values suggest a potential rupture location due to stagnant flow conditions.

The close resemblance between the RRT distribution and the TA-WSS plots further supports the hypothesis that the rupture location is likely near the tip of the aneurysm sac. The highest recorded RRT value was  $645 \text{ kPa}^{-1}$ , highlighted by the black circle in Figure 4.7.

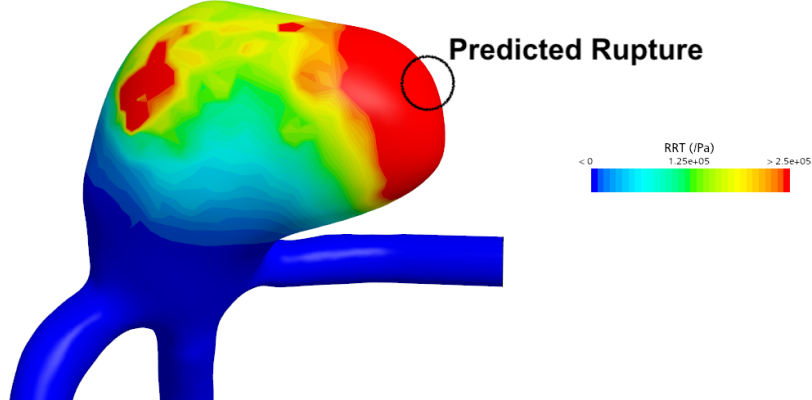


Figure 4.7: Detailed RRT for case 1

#### 4.1.4 Streamlines

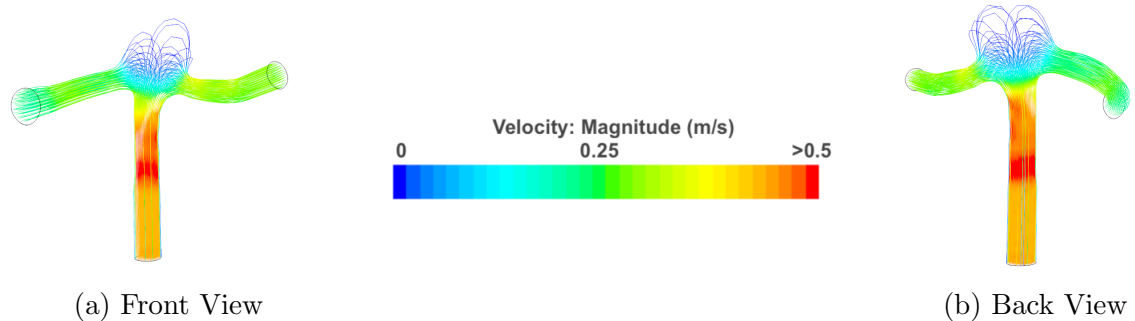


Figure 4.8: Streamlines of case 1

### 4.1.5 Velocity Contours

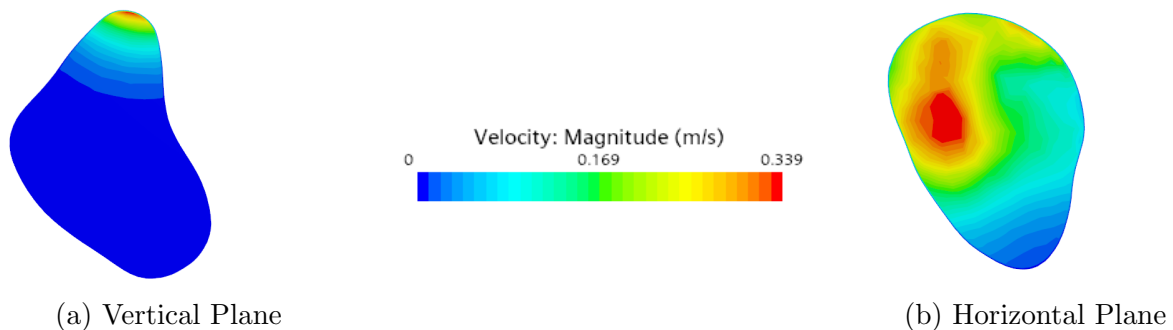


Figure 4.9: Velocity contours of case 1

#### 4.1.6 Pressure Contours

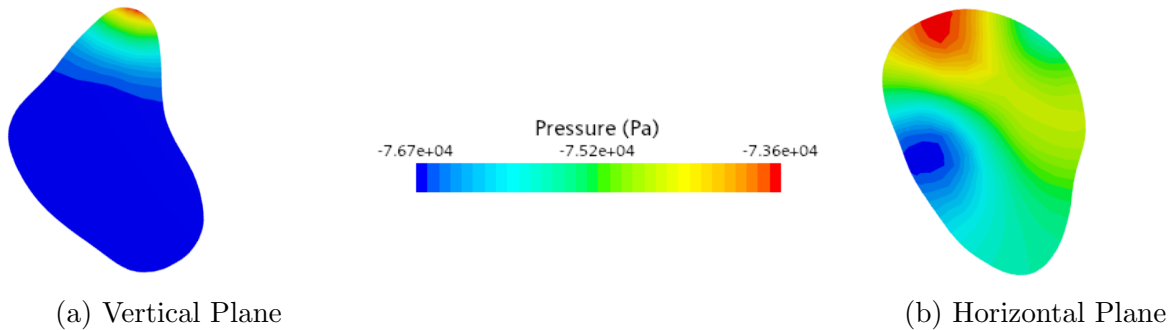


Figure 4.10: Pressure contours of case 1

#### 4.1.7 Summary

Parameter	Minimum Value	Maximum Value
TA-WSS	0 Pa	0.0539 Pa
OSI	0	0.0604
RRT	$18.6 \text{ Pa}^{-1}$	$645 \text{ kPa}^{-1}$
Velocity	0 m/s	0.97 m/s
Pressure	-76.7 kPa	-73.6 kPa

Table 4.1: Summary of case 1

Based on the analysis of the previous subsections, it can be concluded that case 1 presents two potential rupture locations. The primary rupture location is at the uppermost point of the aneurysm sac (point 1 in Figure 4.11). This area is characterised by a combination of high TA-WSS and RRT values, suggesting it is most vulnerable to rupture. The velocity and pressure contours further support this, with a noticeable spike at the tip of the vertical plane, enhancing the accuracy of the rupture location prediction.

A secondary rupture location (point 2 in Figure 4.11) is identified towards the right-hand side of the aneurysm. While this area exhibits lower TA-WSS and RRT values, the elevated OSI values point to increased flow disturbance and higher shear stress, marking it as a secondary area of concern.

Figure 4.11 illustrates these two potential rupture locations, with points 1 and 2 highlighting the regions at risk.

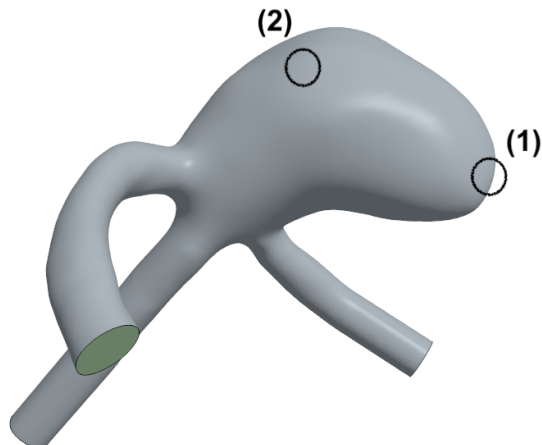


Figure 4.11: Predicted rupture locations for case 1

## 4.2 Case 2

### 4.2.1 TA-WSS

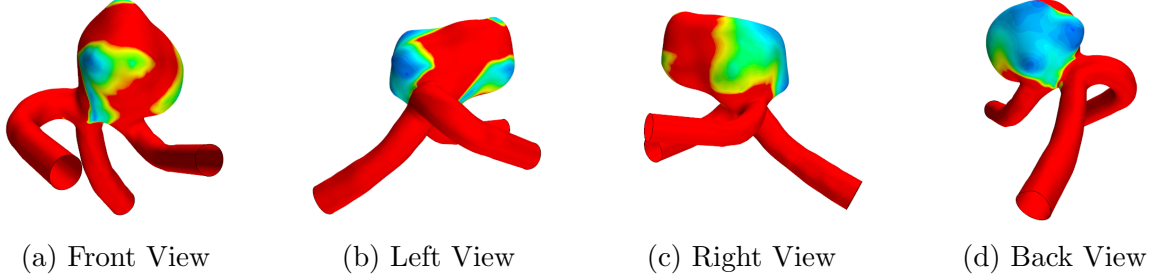


Figure 4.12: 3D diagram of TA-WSS for case 2

Figure 4.12 illustrates the TA-WSS distribution for case 2, which is a multi-saccular aneurysm. As previously mentioned, the blue regions indicate low TA-WSS ( $< 0.125$  Pa), while the red regions represent elevated TA-WSS ( $> 0.25$  Pa). Elevated TA-WSS values are observed at the inlet section and outlet branches. The sac of the aneurysm, however, exhibits both low and high TA-WSS regions. Notably, the regions of low TA-WSS are commonly found at the lobes of the aneurysm, which, according to the low-flow theory, are more susceptible to rupture. From the analysis of the scenes, we can infer that the blood flow inside the front most lobes of the aneurysm is recirculating, which increases their likelihood of rupture.

The lowest recorded TA-WSS value was 0.105 mPa, while the maximum recorded value was 0.262 Pa. The steep gradient observed within the aneurysm sac further suggests that case 2 is more prone to rupture. The predicted rupture location is highlighted by the black circle in Figure 4.13, showcasing a detailed rear view.

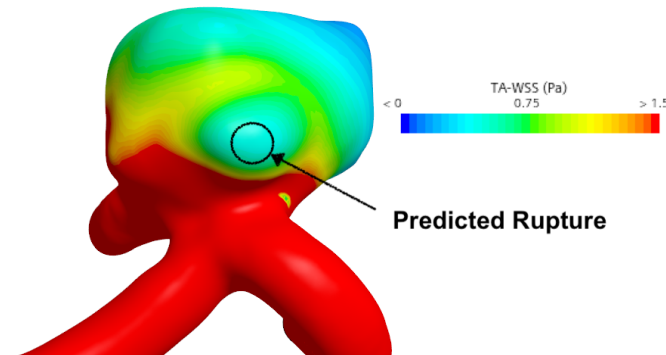


Figure 4.13: Detailed TA-WSS for case 2

#### 4.2.2 OSI

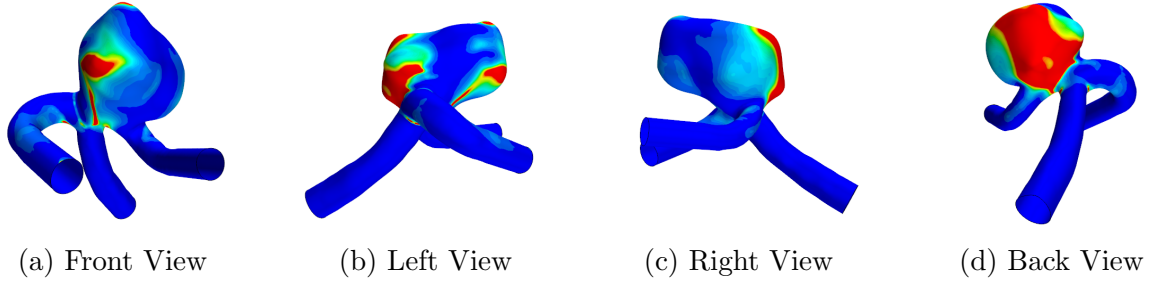


Figure 4.14: 3D diagram of OSI for case 2

Figure 4.14 illustrates the OSI distribution for case 2, where blue regions denote low OSI values ( $< 0.05$ ), and red regions represent elevated OSI values ( $> 0.1$ ). While the aneurysm generally exhibits low OSI throughout the sac, pronounced peaks are observed at the tips of the frontal lobes. These regions closely mirror the distribution patterns seen in TA-WSS, indicating disturbed and oscillatory flow.

As outlined in the low-flow theory, regions of elevated OSI are susceptible to rupture. The elevated OSI values are concentrated at the lobes, and suggest that multi-saccular aneurysms face increased risk of rupture when in comparison to single sac aneurysms.

The minimum recorded OSI value is  $3.29 \times 10^{-8}$ , which is close to zero and indicates regions of near steady flow. The average OSI at the sac is 0.05, while the maximum recorded value is 0.246 at the posterior lobe, as denoted by the black circle in Figure 4.15. The steep gradient and the high maximum OSI value in this area suggest that it is the rupture site.

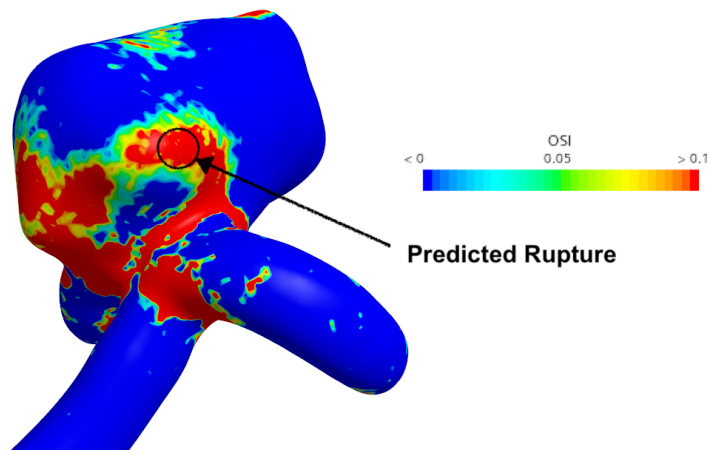


Figure 4.15: Detailed OSI for case 2

#### 4.2.3 RRT

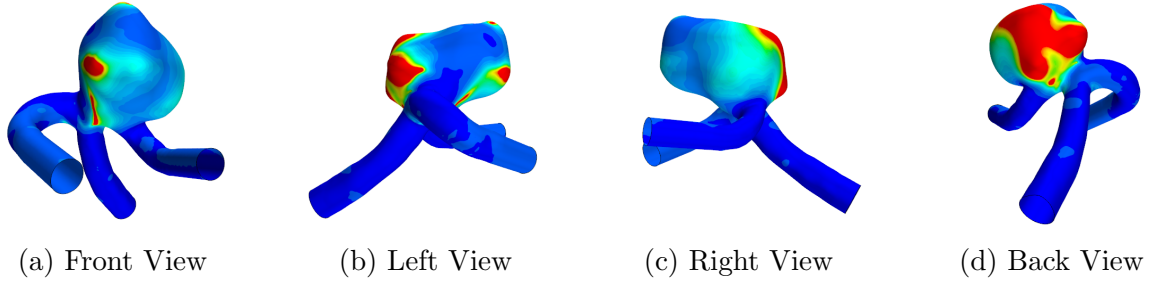


Figure 4.16: 3D diagram of RRT for case 2

Figure 4.16 presents the RRT distribution for case 2. Regions shaded in blue represent low residence times ( $< 500 \text{ Pa}^{-1}$ ), whereas red regions indicate prolonged residence times ( $> 1000 \text{ Pa}^{-1}$ ), suggesting areas of stagnant flow. A consistent trend is observed where elevated RRT values are concentrated at the front and posterior lobes, corresponding to the trends seen in the TA-WSS and OSI plots.

According to the low-flow theory, high RRT is a key pointer to potential wall degeneration. In case 2, the maximum RRT recorded was  $9.51 \text{ kPa}^{-1}$ , observed at the tips of the lobes and highlighted by the black circles in Figure 4.17. These regions coincide with areas of elevated OSI and reduced TA-WSS, reinforcing their classification as likely rupture sites. This further supports the hypothesis that lobular formations significantly increase rupture risk by promoting flow recirculation.

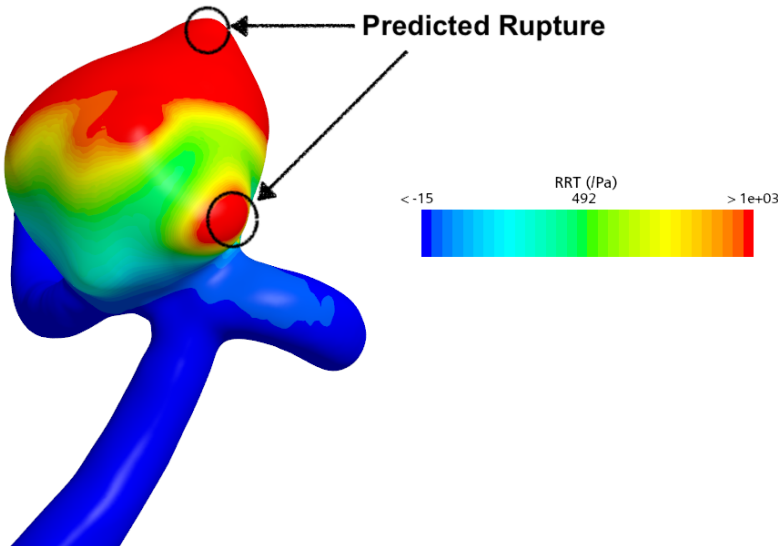


Figure 4.17: Detailed RRT for case 2

#### 4.2.4 Streamlines

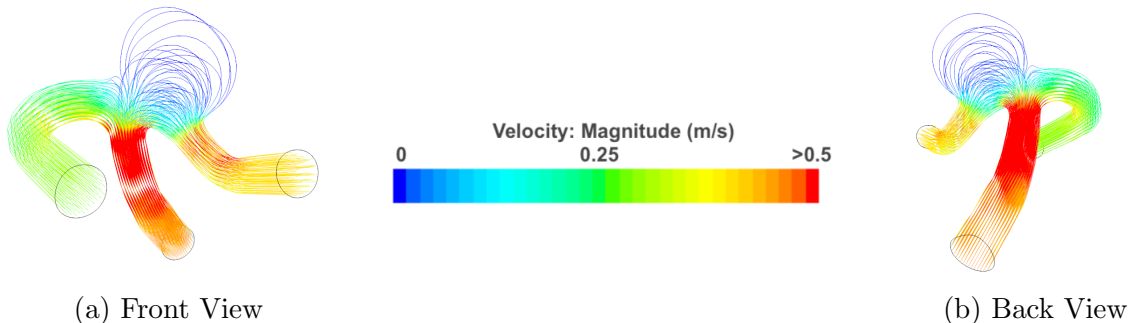


Figure 4.18: Streamlines of case 2

#### 4.2.5 Velocity Contours

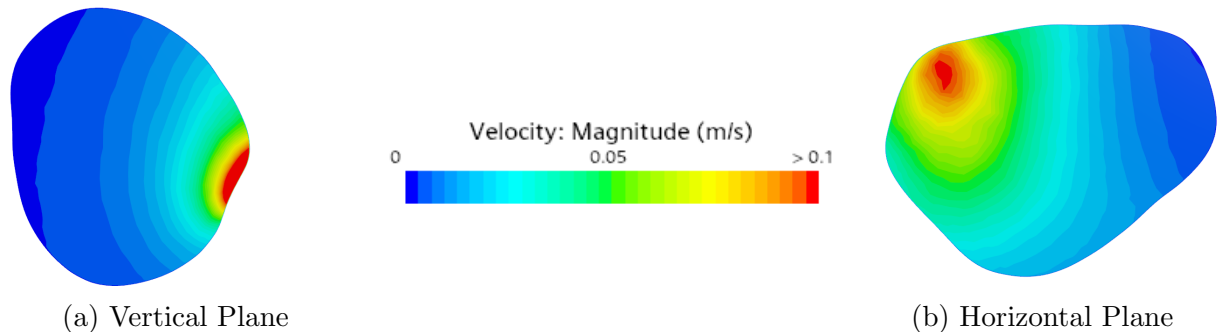


Figure 4.19: Velocity contours of case 2

#### 4.2.6 Pressure Contours

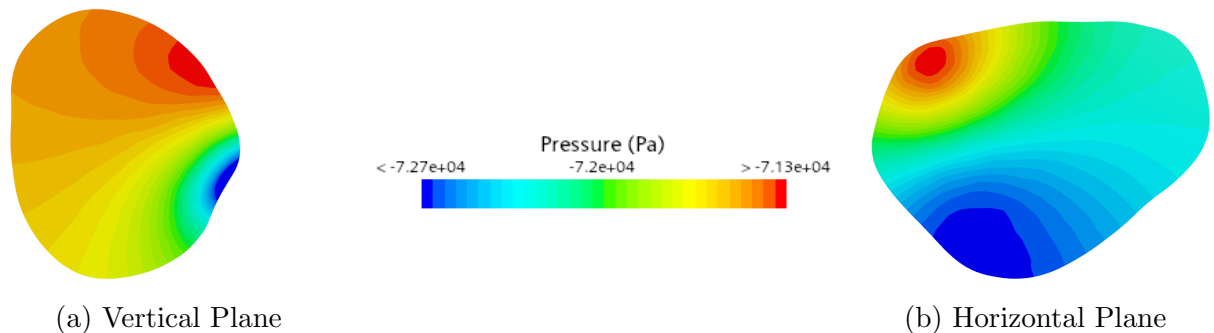


Figure 4.20: Pressure contours of case 2

#### 4.2.7 Summary

Parameter	Minimum Value	Maximum Value
TA-WSS	0 Pa	0.262 Pa
OSI	0	0.246
RRT	$3.81 \text{ Pa}^{-1}$	$9.51 \text{ kPa}^{-1}$
Velocity	0 m/s	1.09 m/s
Pressure	-72.7 kPa	-71.3 kPa

Table 4.2: Summary of case 2

Case 2 presents two potential rupture locations. The primary rupture location is at the front-left lobe of the aneurysm, denoted as point 1 in Figure 4.21. This area is more rupture-prone due to having larger values of TA-WSS and OSI, recorded as 0.262 Pa and 0.246, respectively. These values indicate higher shear stress and flow disturbance.

The secondary rupture location, point 2, is located at the topmost lobe of the aneurysm and exhibits lower values of OSI and TA-WSS but elevated RRT of  $9.51 \text{ kPa}^{-1}$ . Despite the lower shear stress, the elevated RRT values suggest possible flow stagnation, making it a secondary area of concern. Case 2 is comparatively more prone to rupture, as the maximum values recorded in this case are higher than those observed in case 1.

Figure 4.21 illustrates these two potential rupture locations, with points 1 and 2 highlighting the regions at risk.

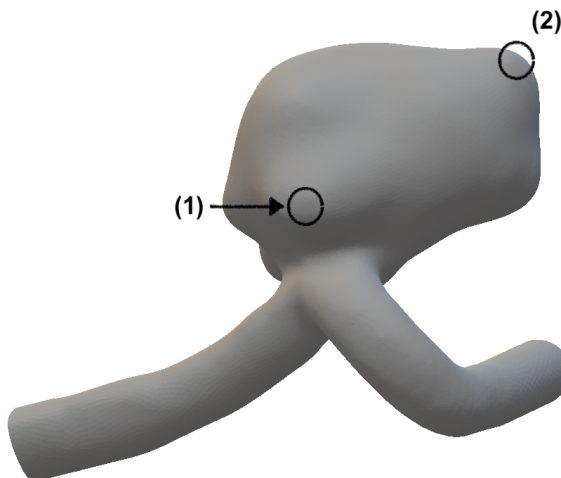


Figure 4.21: Predicted rupture locations for case 2

### 4.3 Case 1 with a flow diversion stent

### 4.3.1 TA-WSS

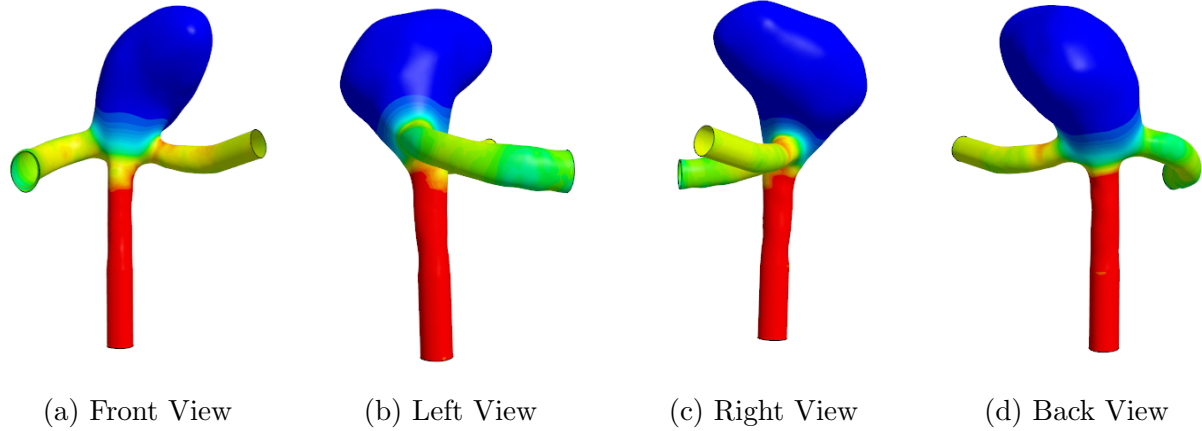


Figure 4.22: 3D diagram of TA-WSS for case 1 with a stent

Figure 4.22 illustrates the TA-WSS distribution for case 1 following the placement of a flow diversion stent at the neck of the aneurysm. The aneurysm sac is predominantly blue, indicating regions of low TA-WSS ( $< 0.02$  Pa). This distribution aligns with the expected haemodynamic effect of flow diversion, where blood is redirected along the parent vessel, resulting in reduced flow into the sac which causes stabilisation and shrinkage over time. The shear gradient from the neck into the sac appears smoother post-treatment, as indicated by the green hues near the neck and branches. According to the low-flow theory applied in this study, regions of low TA-WSS are prone to rupture. The predicted rupture location remains similar to the untreated case, located at the tip of the aneurysm sac. The lowest measured TA-WSS value was  $1.94 \times 10^{-6}$  Pa and is marked by the black circle in Figure 4.23.

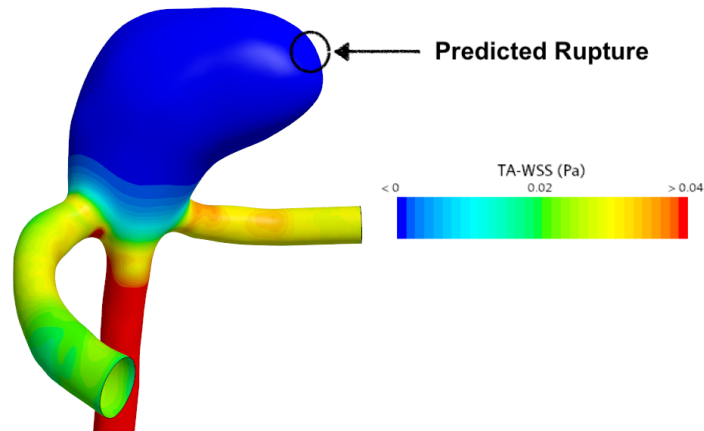


Figure 4.23: Detailed TA-WSS for case 1 with a stent

#### 4.3.2 OSI

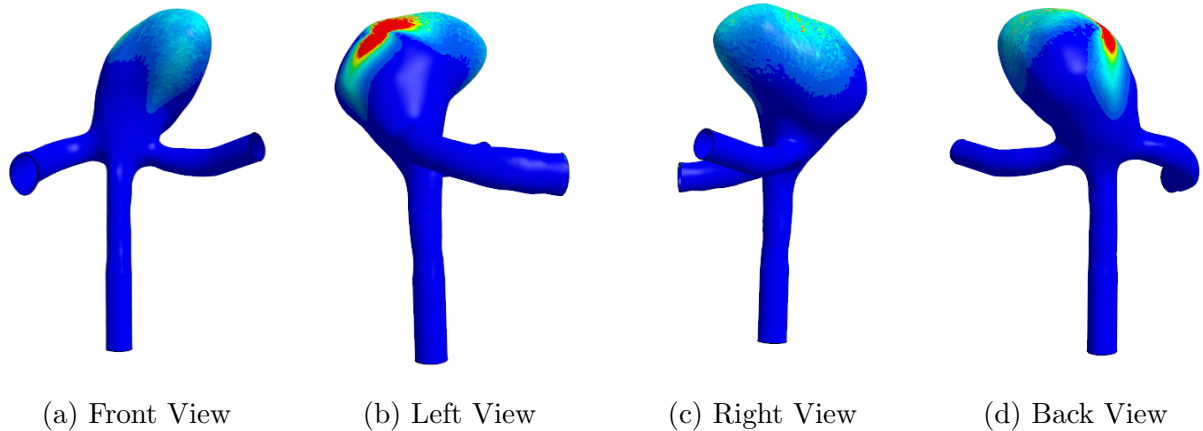


Figure 4.24: 3D diagram of OSI for case 1 with a stent

Figure 4.24 presents the OSI distribution for case 1 following the placement of a flow diversion stent. The overall pattern closely resembles that of the untreated baseline; however, all regions appear less pronounced, indicating a notable reduction in OSI values. The aneurysm sac is largely shaded in blue, with an isolated red region ( $> 0.01$ ) observed at the left lobe, representing a localised area of elevated OSI.

The maximum OSI recorded was 0.186, concentrated at the left region of the aneurysm dome, and is highlighted by the black circle in Figure 4.25. According to the low-flow theory applied in this study, regions with elevated OSI are more susceptible to rupture. Hence, the left lobe is identified as the most likely rupture site following treatment.

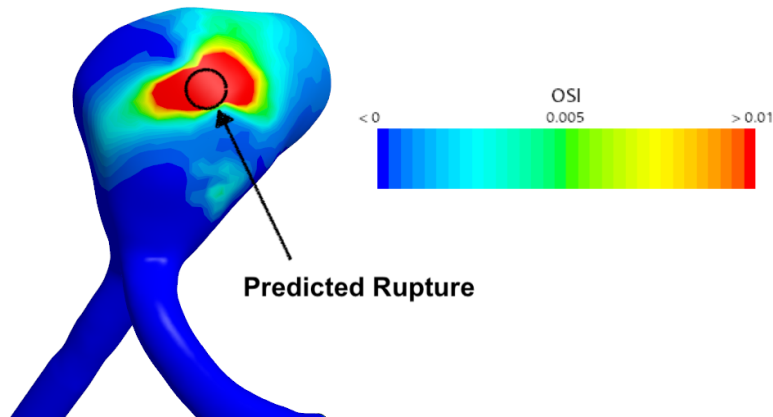


Figure 4.25: Detailed OSI for case 1 with a stent

### 4.3.3 RRT

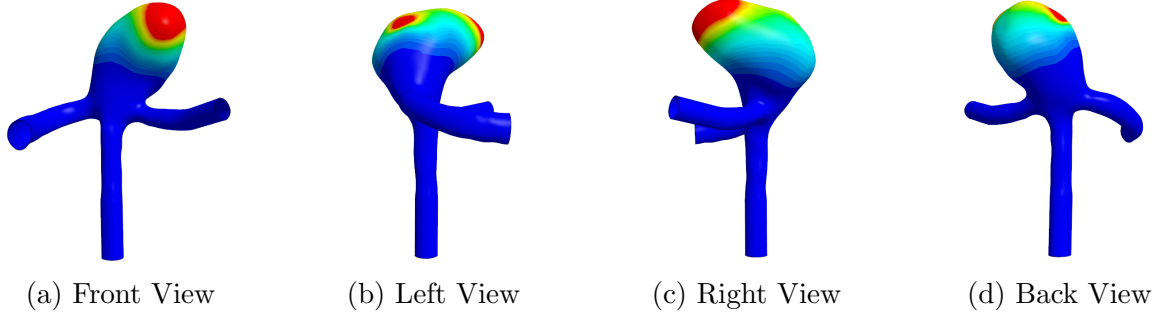


Figure 4.26: 3D diagram of RRT for case 1 with a stent

Figure 4.26 illustrates the RRT distribution for case 1 following the placement of a flow diversion stent. The overall pattern remains similar to the untreated case, with elevated RRT values concentrated at the tip and left side of the aneurysm sac, as indicated by the red hues. A notable increase in RRT is observed when compared to baseline case, reflecting a reduction in intra-aneurysmal flow velocity. This outcome is a result of the stent diverting blood away from the sac, thereby reducing circulation within it. Consequently, blood particles remain within the sac for longer durations, leading to increased residence time.

According to the low-flow theory, elevated RRT values indicate that the aneurysm may remain vulnerable to rupture in the short term due to stagnation of blood within the sac. The maximum recorded RRT value was  $1.31 \times 10^6 \text{ Pa}^{-1}$ , located at the tip of the aneurysm dome, and is highlighted by the black circle in Figure 4.27.

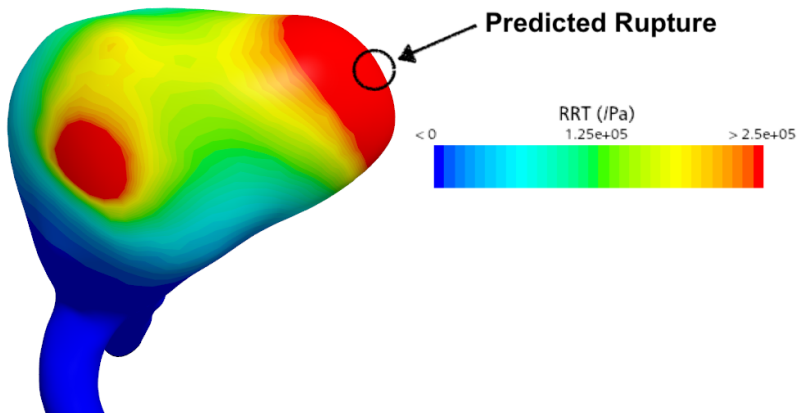


Figure 4.27: Detailed RRT for case 1 with a stent

#### 4.3.4 Streamlines

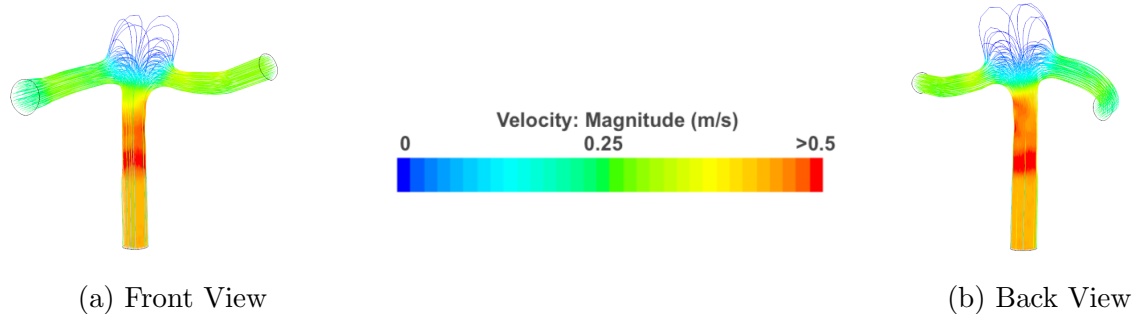


Figure 4.28: Streamlines of case 1 with a stent

### 4.3.5 Velocity Contours

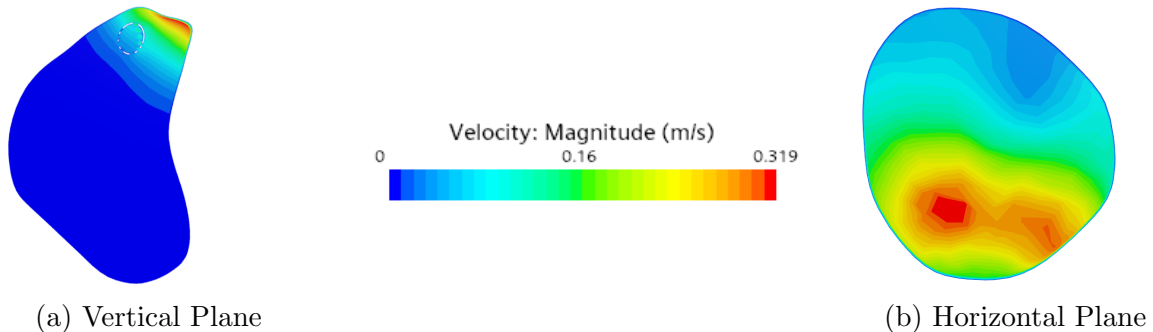


Figure 4.29: Velocity contours of case 1 with a stent

### 4.3.6 Pressure Contours

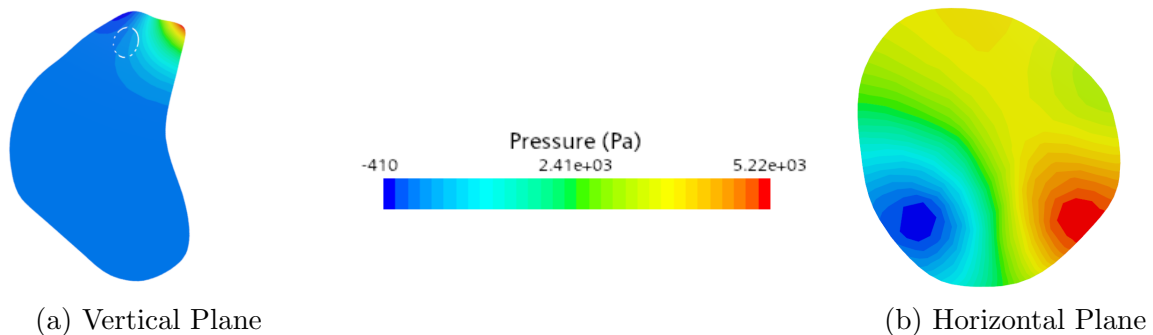


Figure 4.30: Pressure contours of case 1 with a stent

#### 4.3.7 Summary

Parameter	Minimum Value	Maximum Value
TA-WSS	0 Pa	0.0568 Pa
OSI	0	0.186
RRT	$17.6 \text{ Pa}^{-1}$	$131 \text{ kPa}^{-1}$
Velocity	0 m/s	0.88 m/s
Pressure	-410 Pa	5.22 kPa

Table 4.3: Summary of case 1 with a flow diversion stent

TA-WSS has slightly increased compared to the baseline case, due to the fluid-structure interaction (FSI) between the stent and the neck of the aneurysm. However, this effect is negligible, as the increase is only  $2.9 \times 10^{-3}$  Pa.

Point 1 in Figure 4.31 experiences an elevated RRT; however, this value is still comparatively lower than in the original baseline case. The maximum OSI recorded has increased, but it remains an isolated and localised region, located at point 2 in Figure 4.31. Overall, there is a decrease in the average OSI around the aneurysm sac, with a noticeable smoothing of the haemodynamic profile.

The rupture locations have not shifted compared to the baseline case. While the rupture risk has decreased slightly, potential complications may arise at the neck of the aneurysm due to the stent's placement. In comparison to the original baseline, the changes with the treatment are negligible, except for the overall smoothing of the haemodynamic profile.

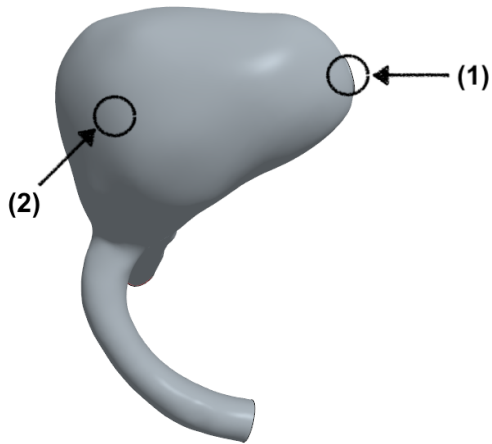


Figure 4.31: Predicted rupture locations for case 1 with a stent

## 4.4 Case 2 with a flow diversion stent

### 4.4.1 TA-WSS

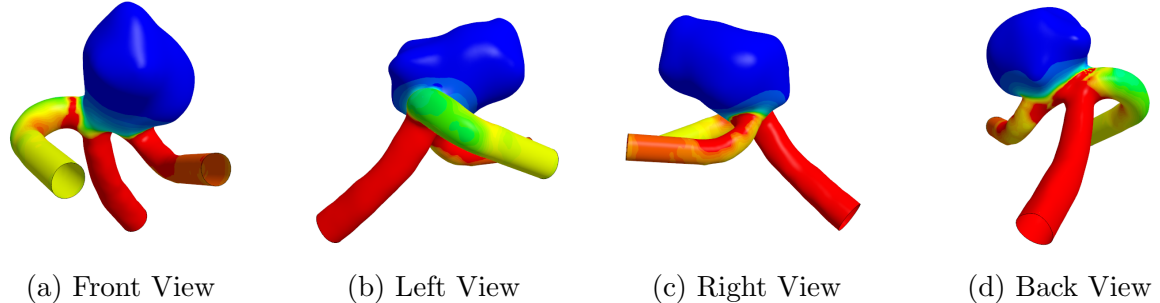


Figure 4.32: 3D diagram of TA-WSS for case 2 with a flow diversion stent

Figure 4.32 illustrates the TA-WSS distribution for case 2 following the placement of a flow diversion stent. The employment of the stent has led to a more widespread presence of low TA-WSS values ( $< 0.015$  Pa), as indicated by the extended blue regions throughout the sac. Elevated TA-WSS values, depicted in red ( $> 0.03$  Pa), remain concentrated around the inlet and outlet branches of the vessel. The gradient at the neck is smoother and less pronounced compared to the untreated baseline case.

The minimum TA-WSS recorded was  $2.49 \times 10^{-5}$  Pa, while the maximum reached 1.04 Pa. According to the low-flow theory, regions of low TA-WSS are more prone to rupture due to increased stagnation and wall exposure. The lowest TA-WSS values are located at the frontmost lobe of the aneurysm sac, which remains the most likely rupture site despite the stent. This area is denoted by the black circle in Figure 4.33.

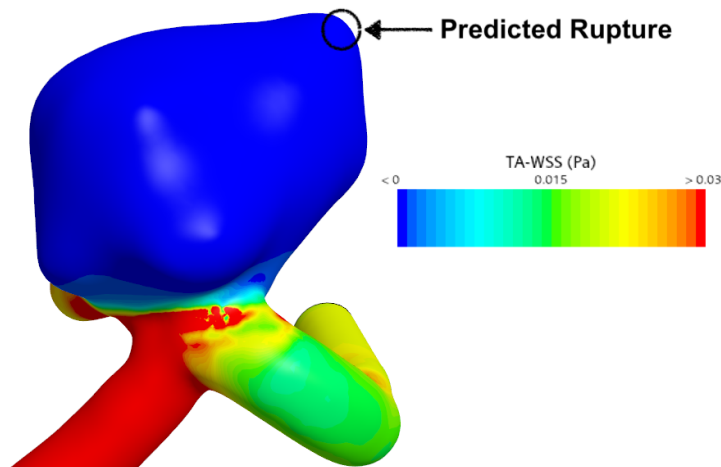


Figure 4.33: Detailed TA-WSS for case 2 with a stent

#### 4.4.2 OSI

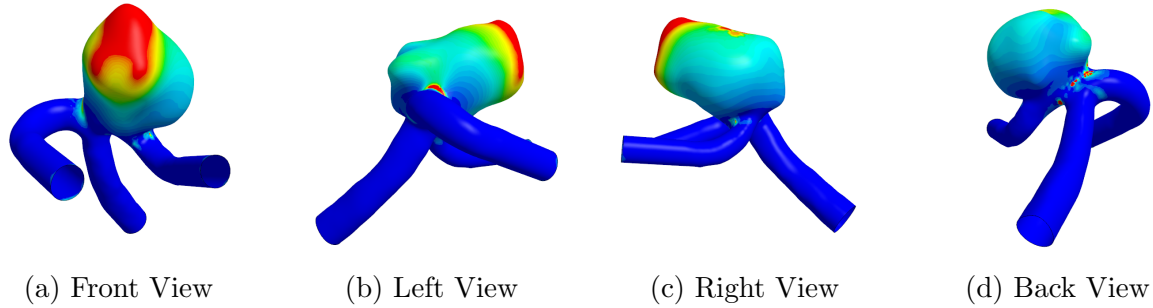


Figure 4.34: 3D diagram of OSI for case 2 with a flow diversion stent

Figure 4.34 illustrates the OSI distribution for case 2 following the placement of a flow diversion stent. A clear reduction in OSI is observed, with more regions shaded blue, indicating lower OSI values ( $< 0.0025$ ). Regions of elevated OSI ( $> 0.005$ ) are at the lobes of the aneurysm. However, in contrast to the untreated case, the posterior lobes now exhibit a marked reduction in OSI, as seen in Figure 4.34(d). This suggests a shift in the predicted rupture location towards the frontal lobes.

This redistribution reflects a change in flow behaviour induced by the stent, where oscillatory flow has become more prominent in the frontal lobes, while the posterior region now appears to exhibit more stable, laminar flow.

According to the low-flow theory, elevated OSI regions are more susceptible to rupture. The maximum OSI value recorded was 0.211, located at the frontal lobe, and is highlighted by the black circle in Figure 4.35. This indicates a reduction in the number of potential rupture locations and a subtle shift in the most probable rupture site.

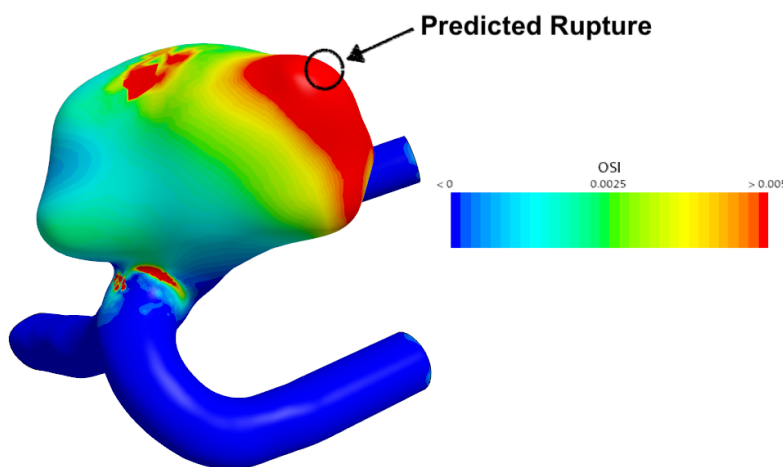


Figure 4.35: Detailed OSI for case 2 with a stent

#### 4.4.3 RRT

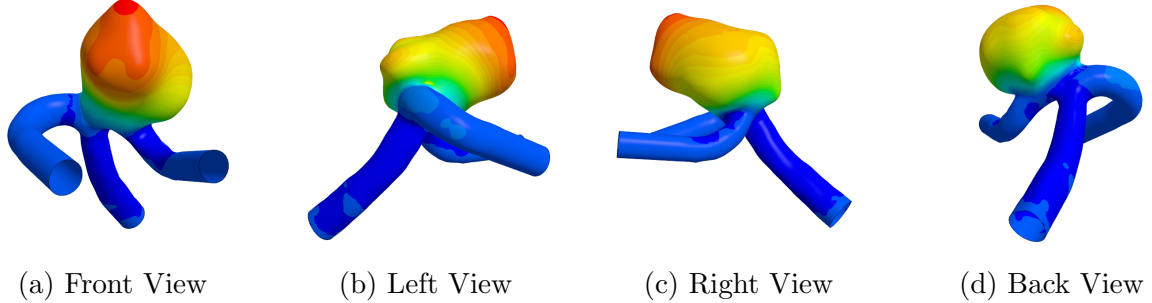


Figure 4.36: 3D diagram of RRT for case 2 with a flow diversion stent

Figure 4.36 presents the RRT distribution for case 2 following the placement of a flow diversion stent. A notable reduction in RRT is observed across the sac, with extensive regions now shaded in yellow, indicating shorter residence times ( $< 750 \text{ Pa}^{-1}$ ). Compared to the untreated case, the elevated RRT values previously observed at the posterior lobes have substantially decreased, as evident by Figure 4.36(d).

The maximum RRT recorded was  $976 \text{ Pa}^{-1}$ , while the minimum was  $1.03 \text{ Pa}^{-1}$ . According to the low-flow theory, elevated RRT is indicative of increased rupture risk due to prolonged blood particle residence. In this case, the most prominent area of elevated RRT remains at the anterior lobe, marked by the black circle in Figure 4.37, though both the intensity and spatial extent have reduced in comparison to the baseline.

The RRT distribution closely mirrors the patterns observed in the OSI and TA-WSS scenes, supporting the conclusion that the stent leads to a reduction in the number of potential rupture locations, as well as a subtle shift in the most probable rupture site.

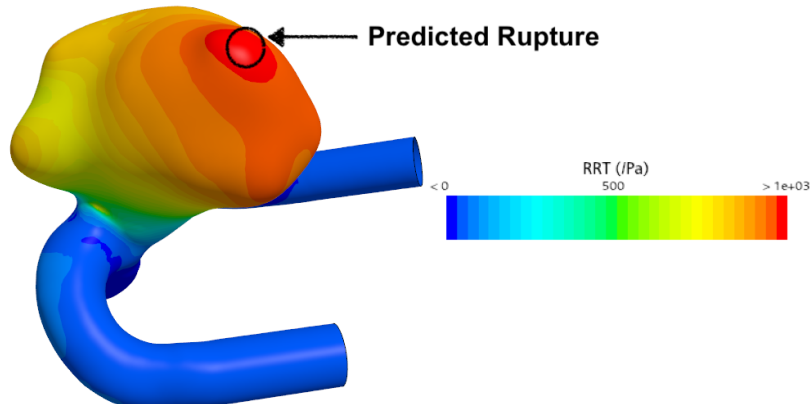


Figure 4.37: Detailed RRT for case 2 with a stent

#### 4.4.4 Streamlines

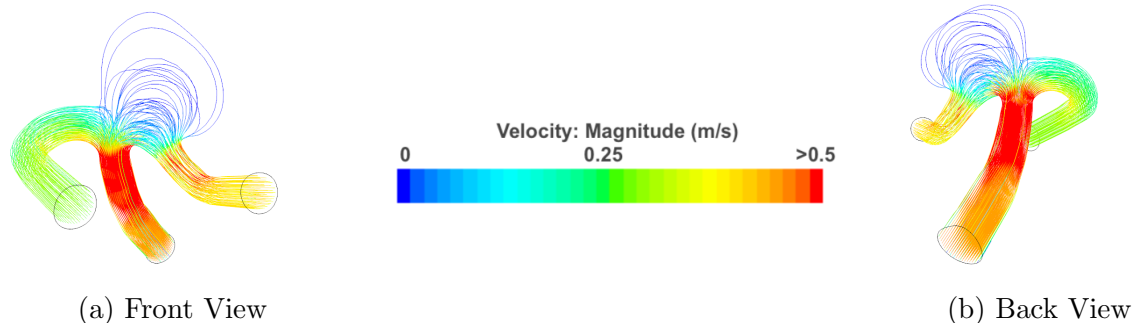


Figure 4.38: Streamlines of case 2 with a flow diversion stent

#### 4.4.5 Velocity Contours

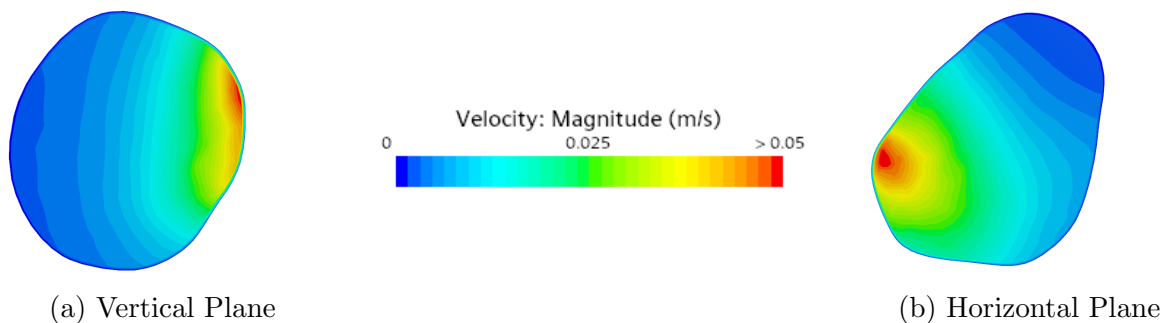


Figure 4.39: Velocity contours of case 2 with a flow diversion stent

#### 4.4.6 Pressure Contours

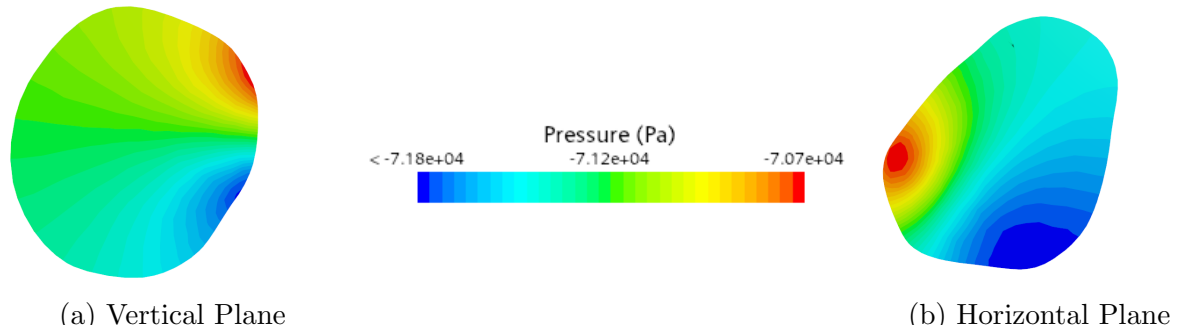


Figure 4.40: Pressure contours of case 2 with a flow diversion stent

#### 4.4.7 Summary

Parameter	Minimum Value	Maximum Value
TA-WSS	0 Pa	1.04 Pa
OSI	0	0.211
RRT	$1.03 \text{ Pa}^{-1}$	$976 \text{ Pa}^{-1}$
Velocity	0 m/s	0.96 m/s
Pressure	-71.8 kPa	-70.7 kPa

Table 4.4: Summary of case 2 with a flow diversion stent

The addition of a stent has resulted in a decrease in the number of potential rupture locations, reducing it to one, as denoted by point 1 in Figure 4.41. There is a notable increase in TA-WSS from 0.262 Pa to 1.04 Pa due to the FSI caused by the stent. This increase is located at the neck of the aneurysm and may cause potential complications both post-treatment and in the long run.

The OSI, velocity, and pressure values remain largely unchanged, with all values showing a  $\pm 15\%$  variation from the baseline. There is a considerable decrease in RRT and an overall smoothing of the haemodynamic profile, as evidenced by the orange gradient shown in Figure 4.36, indicating a more stable flow post-treatment.

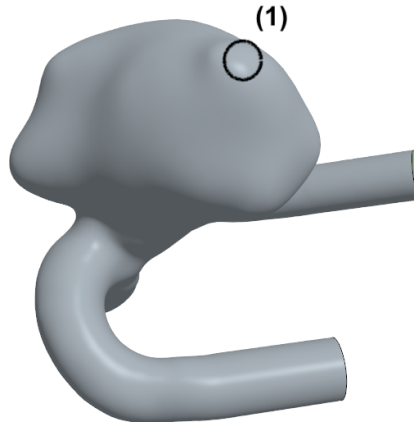


Figure 4.41: Predicted rupture locations for case 2 with a stent

## 4.5 Case 1 with an endovascular coiling

### 4.5.1 TA-WSS

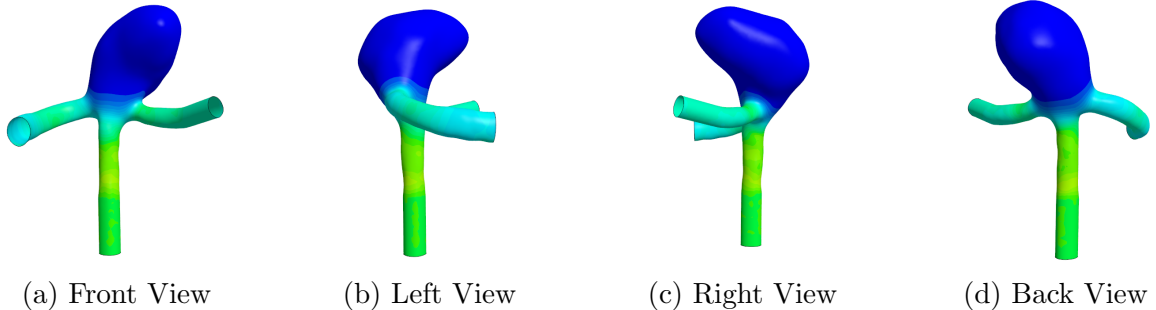


Figure 4.42: 3D diagram of TA-WSS for case 1 with an endovascular coiling

Figure 4.42 illustrates the TA-WSS distribution for case 1 following the addition of an endovascular coil. In comparison to the untreated case, a more uniform region of low TA-WSS ( $< 0.015$  Pa) is observed across the aneurysm sac, which is now entirely shaded blue. This is expected, as coiling disrupts blood flow by physically occupying space within the sac. Unlike the untreated case, where elevated TA-WSS was observed at the branches and a sharp gradient was present at the neck, the coiled case shows minimal shear activity across the aneurysm. The inlet and outlet branches continue to exhibit moderate TA-WSS levels, with the shear gradient being noticeably smoother and less defined.

According to the low-flow theory applied in this study, regions of low TA-WSS are more susceptible to rupture. The lowest TA-WSS value was  $89\mu$  Pa, located centrally within the sac and marked by the black circle in Figure 4.43.

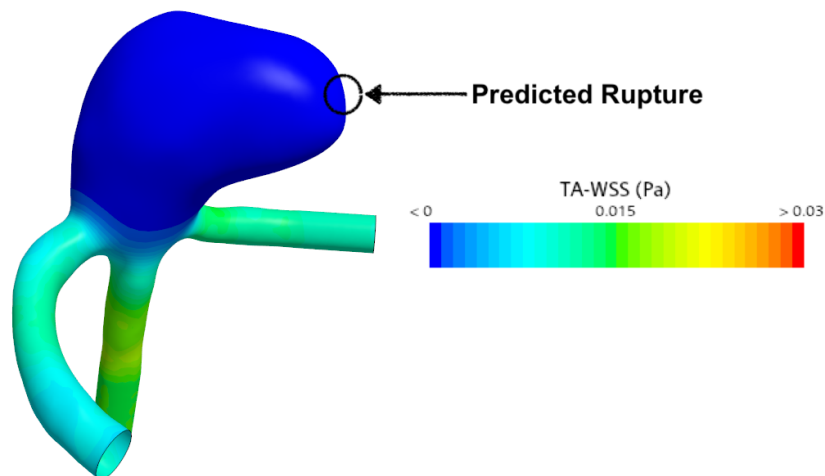


Figure 4.43: Detailed TA-WSS for case 1 with an endovascular coil

#### 4.5.2 OSI

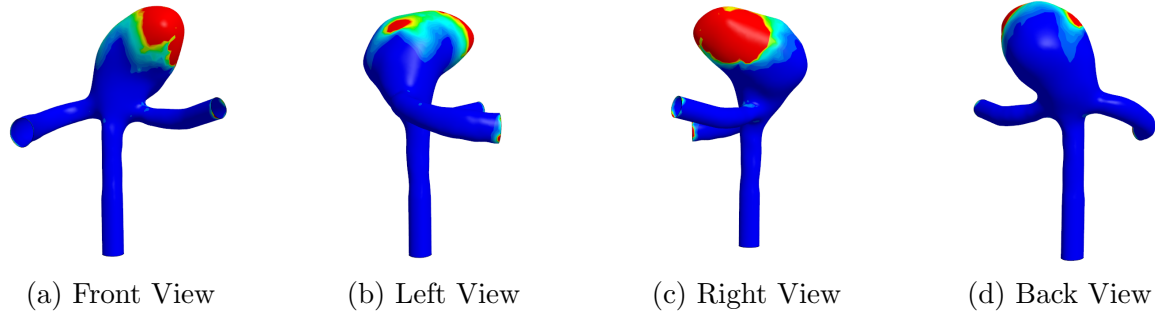


Figure 4.44: 3D diagram of OSI for case 1 with an endovascular coiling

Figure 4.44 presents the OSI distribution for case 1 following the placement of an endovascular coil. A general reduction in OSI is observed across the sac compared to the untreated case, with most of the aneurysm now shaded blue-green, indicating low OSI values ( $< 0.001$ ). Despite this overall decrease, a distinct localised peak remains at the upper right region of the sac, where OSI values exceed 0.05, as shown in red.

According to the low-flow theory applied in this study, regions of elevated OSI are more susceptible to rupture due to disturbed and oscillating flow patterns. The peak OSI recorded was 0.0807 and is located at the same horizontal plane as in the untreated case, supporting the prediction that the right side of the dome remains the most likely rupture. This area is highlighted by the black circle in Figure 4.45.

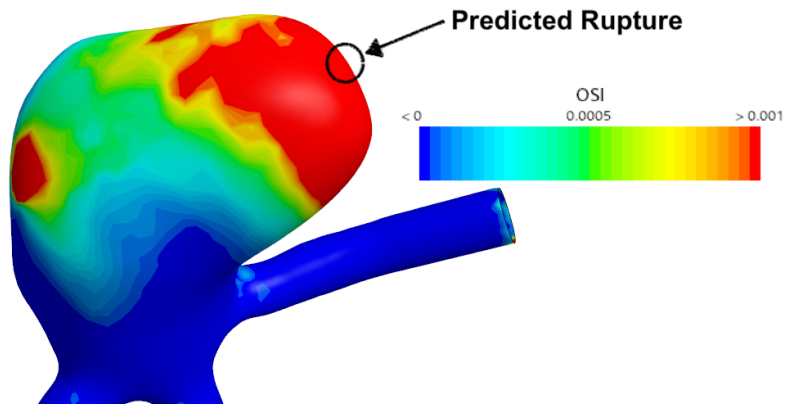


Figure 4.45: Detailed OSI for case 1 with an endovascular coil

### 4.5.3 RRT

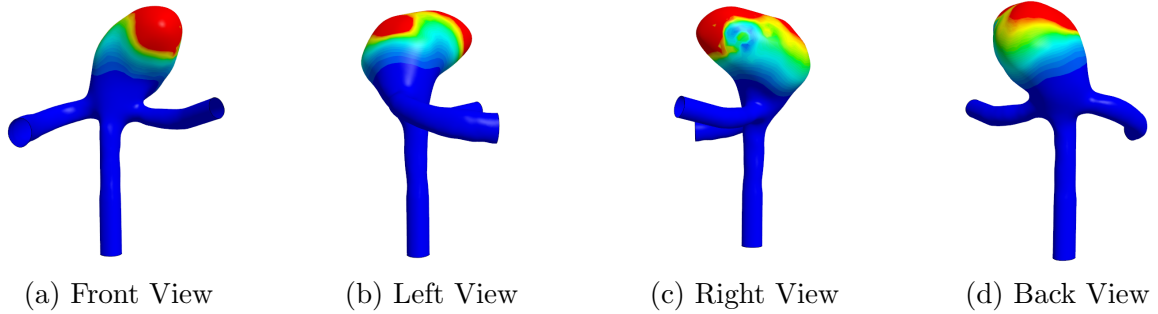


Figure 4.46: 3D diagram of RRT for case 1 with an endovascular coiling

Figure 4.46 illustrates the RRT distribution for case 1 following the placement of an endovascular coil. The overall pattern closely resembles the untreated configuration, with elevated RRT values concentrated at the upper dome of the aneurysm sac. These regions are shown in red, indicating prolonged residence times ( $> 250 \text{ kPa}^{-1}$ ). In contrast, lower RRT values ( $< 125 \text{ kPa}^{-1}$ ) remain at the neck and branches, suggesting areas of faster-moving flow.

The maximum recorded RRT was  $1.55 \times 10^6 \text{ Pa}^{-1}$ , a substantial increase compared to the untreated case. This sharp rise in RRT reflects the stagnation of blood within the sac as a result of coiling, which obstructs flow and encourages prolonged blood residence. According to the low-flow theory, elevated RRT is a key indicator of potential rupture. The highest RRT region, located at the right dome of the aneurysm, is highlighted by the black circle in Figure 4.47.

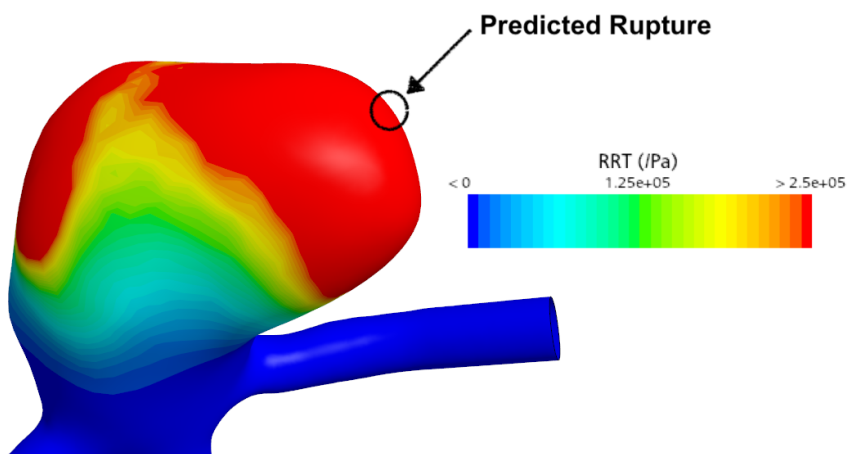


Figure 4.47: Detailed RRT for case 1 with an endovascular coil

#### 4.5.4 Streamlines

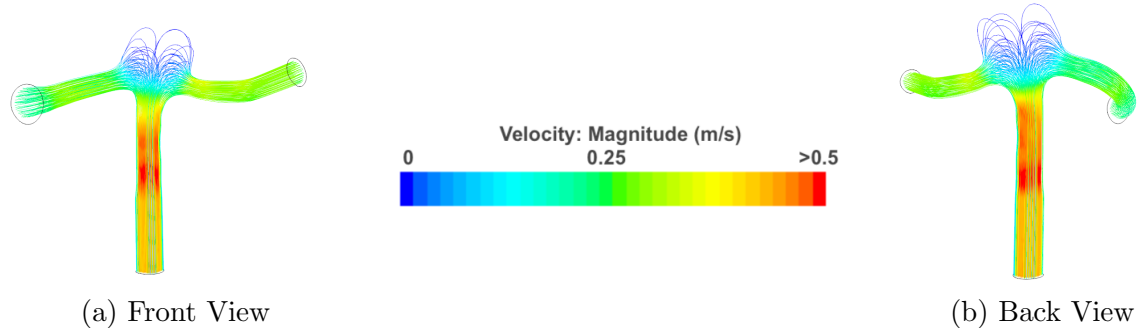


Figure 4.48: Streamlines of case 1 with an endovascular coiling

### 4.5.5 Velocity Contours

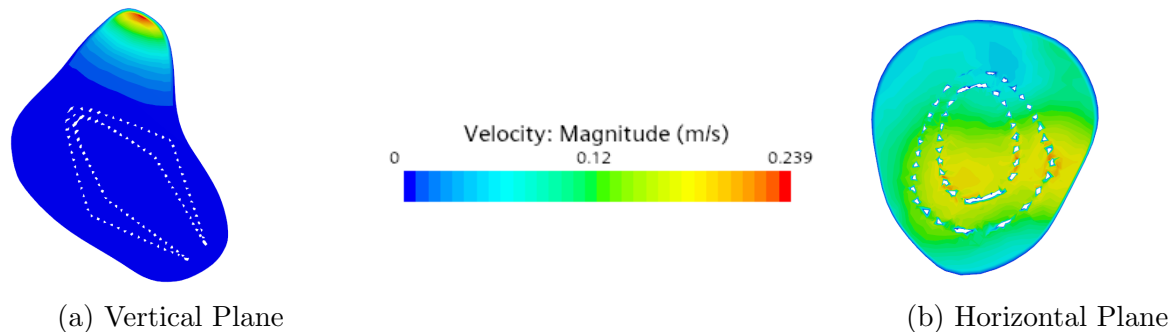


Figure 4.49: Velocity contours of case 1 with an endovascular coiling

#### 4.5.6 Pressure Contours

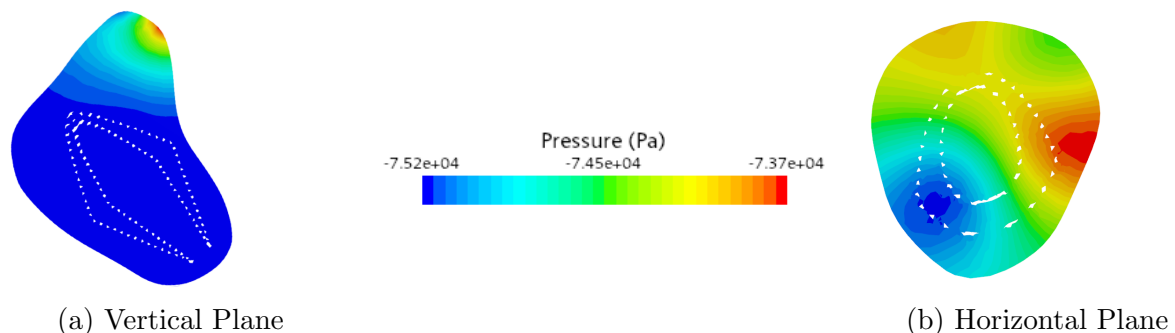


Figure 4.50: Pressure contours of case 1 with an endovascular coiling

#### 4.5.7 Summary

Parameter	Minimum Value	Maximum Value
TA-WSS	0 Pa	0.0186 Pa
OSI	0	0.0807
RRT	$53.6 \text{ Pa}^{-1}$	$155 \text{ kPa}^{-1}$
Velocity	0 m/s	0.79 m/s
Pressure	-75.2 kPa	-73.7 kPa

Table 4.5: Summary of case 1 with an endovascular coil

The addition of a coil has resulted in a decrease in the number of potential rupture locations; however, the primary rupture location persists at the topmost lobe, as denoted by the black circle in Figure 4.51. When compared with the baseline, it is evident that there is a considerable drop in the maximum TA-WSS, from 0.0539 Pa to 0.0186 Pa in the coiled case. Additionally, the maximum velocity recorded has decreased by 0.18 m/s compared to the baseline.

Although promising, when compared to the stent configuration, it is evident that the coiling treatment lacks the decrease in average OSI and RRT. Instead, it results in a smoother haemodynamic profile with lowered maximum values. The RRT values support this trend, as they were recorded at  $155 \text{ kPa}^{-1}$  for the coil and  $131 \text{ kPa}^{-1}$  for the stent, suggesting flow stagnation at the top lobe, which may result in complications.

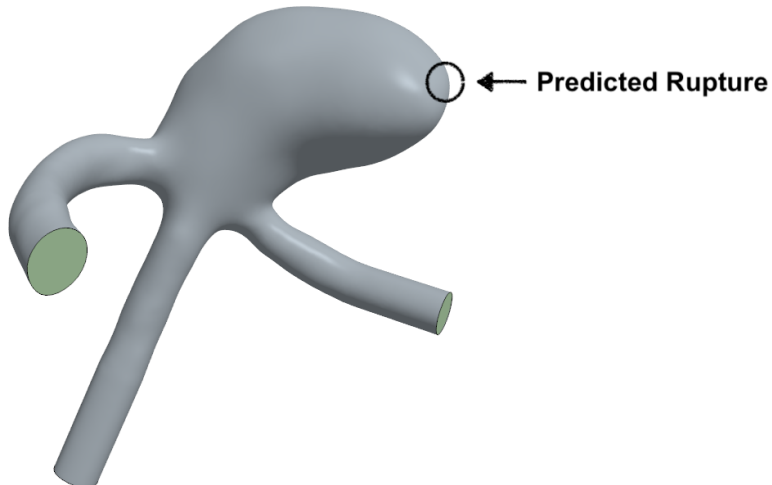


Figure 4.51: Predicted rupture locations for case 1 with a coil

## 4.6 Case 2 with an endovascular coiling

### 4.6.1 TA-WSS

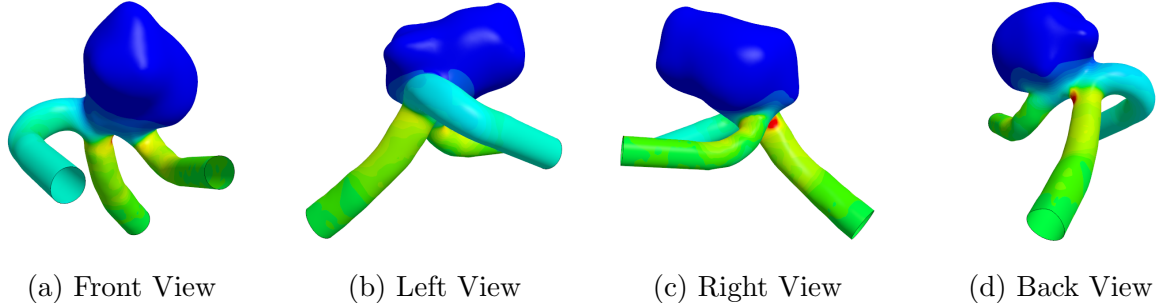


Figure 4.52: 3D diagram of TA-WSS for case 2 with an endovascular coiling

Figure 4.52 illustrates the TA-WSS distribution for case 2 following the placement of an endovascular coil. A reduction in wall shear stress is observed throughout the aneurysm sac, as the entire dome now shaded in blue, representing low TA-WSS values ( $< 0.01$  Pa). In contrast to the untreated configuration, where both low and high shear regions were visible, the coiled case exhibits low TA-WSS across all lobes. This reflects the expected haemodynamic effect of coiling, where blood entry is limited. Elevated shear values are still observed at the vessel branches, the sharp gradients previously seen at the neck and within the lobes have been significantly smoothed out.

The minimum TA-WSS value recorded was  $1.39 \times 10^{-5}$  Pa, and the maximum was 0.0326 Pa. According to the low-flow theory, regions of low TA-WSS are more susceptible to rupture. The lowest TA-WSS region is located at the upper frontal lobe of the sac and is highlighted by the black circle in Figure 4.53.

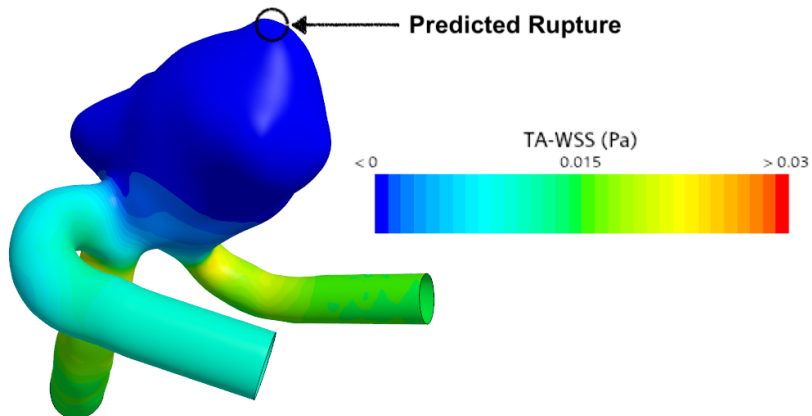


Figure 4.53: Detailed TA-WSS for case 2 with an endovascular coil

#### 4.6.2 OSI

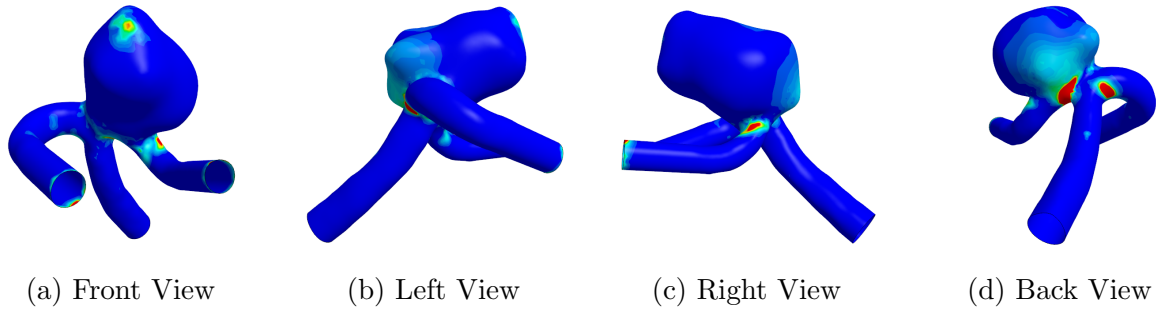


Figure 4.54: 3D diagram of OSI for case 2 with an endovascular coiling

Figure 4.54 illustrates the OSI distribution for case 2 after treatment with an endovascular coiling procedure. It is clear that the OSI values have decreased significantly, as shown by the blue hue now covering the majority of the aneurysm sac, indicating that the OSI values have dropped below  $25 \times 10^{-5}$ . The elevated OSI areas that were present in the frontal lobes in the untreated case are largely mitigated, leaving a small residual peak near the top of the aneurysm, as illustrated in Figure 4.54(a). Although the posterior lobes have also shown a decrease in OSI, there remains a noticeable elevated region near the neck. This is likely due to the fluid-structure interaction between the blood flow and the coil, which causes minor blood flow oscillations. Additionally, elevated OSI is observed at the right (M2 superior) branch, indicating that this area may become a secondary point of concern over time.

The maximum OSI recorded was 0.0642, located at the rear neck of the aneurysm, as denoted by the black circle in Figure 4.55.

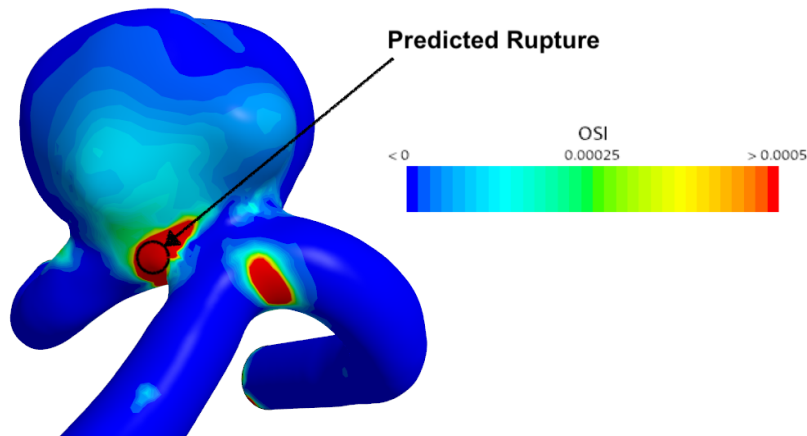


Figure 4.55: Detailed OSI for case 2 with an endovascular coil

### 4.6.3 RRT

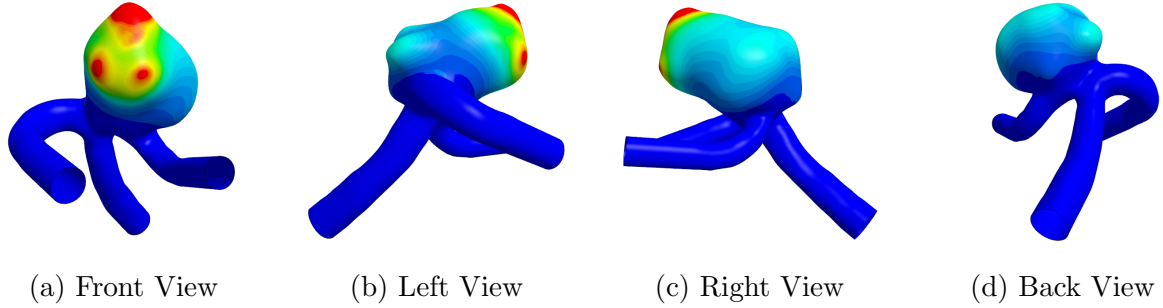


Figure 4.56: 3D diagram of RRT for case 2 with an endovascular coiling

Figure 4.56 showcases the RRT distribution for case 2 following the coiling treatment. It is evident that the RRT has decreased when compared to the untreated case, particularly noticeable in the rear view, where RRT values are now less than  $15 \text{ kPa}^{-1}$ , as indicated by the blue-cyan hue in Figure 4.56(d). While the coil proves advantageous in the rear region, a clustered pattern of elevated RRT values is present in the topmost frontal lobe, as shown in Figure 4.56(a). This region exhibited low RRT values in both the untreated and stent conditions; however, it now experienced RRT values exceeding  $30 \text{ kPa}^{-1}$ . This is likely a consequence of the coil restricting outflow from the sac, leading to higher blood residence times. It is important to note that the simulations in this study were run for two cardiac cycles (1.8 seconds), and as a result, the long-term progression of blood out of the sac is not captured.

According to the low-flow theory employed in this study, regions of elevated RRT are more susceptible to rupture. Based on the current RRT distribution at 1.8 seconds, the maximum recorded value was  $71.8 \text{ kPa}^{-1}$ . It is therefore predicted that the instantaneous rupture location is situated near the top of the aneurysm sac, as indicated by the black circle in Figure 4.57.

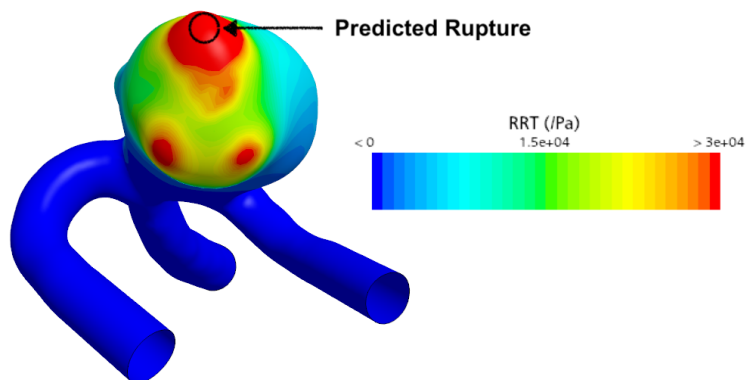


Figure 4.57: Detailed RRT for case 2 with an endovascular coil

#### 4.6.4 Streamlines

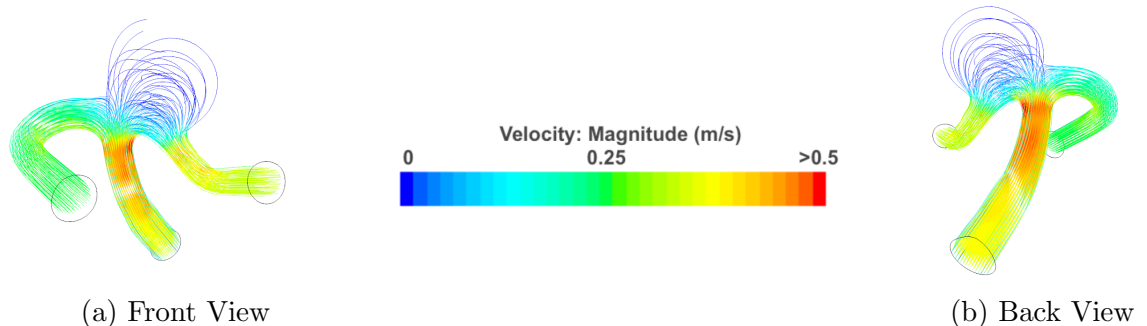


Figure 4.58: Streamlines of case 2 with an endovascular coiling

#### 4.6.5 Velocity Contours

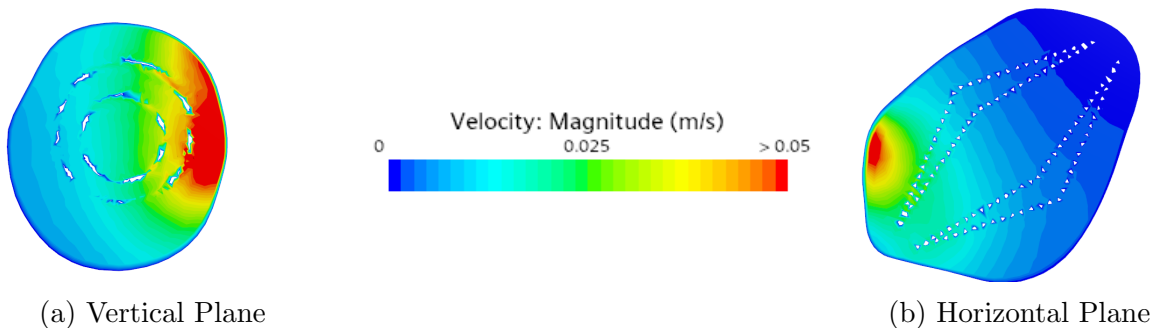


Figure 4.59: Velocity contours of case 2 with an endovascular coiling

#### 4.6.6 Pressure Contours

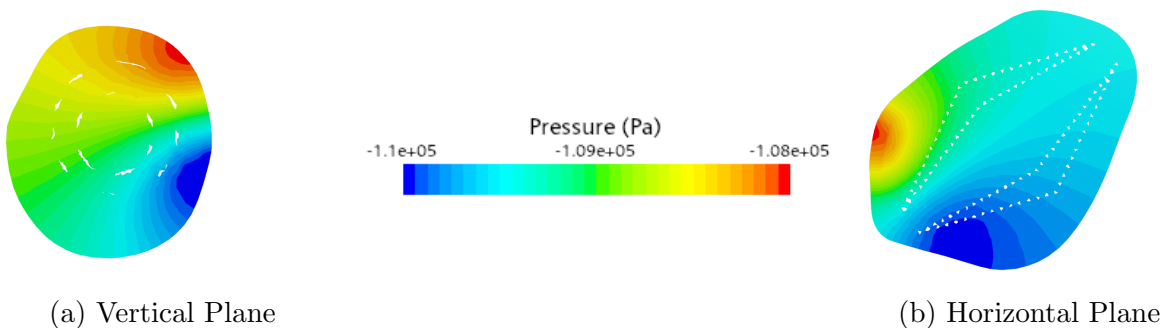


Figure 4.60: Pressure contours of case 2 with an endovascular coiling

#### 4.6.7 Summary

Parameter	Minimum Value	Maximum Value
TA-WSS	0 Pa	0.0326 Pa
OSI	0	0.0642
RRT	$30.7 \text{ Pa}^{-1}$	$71.8 \text{ kPa}^{-1}$
Velocity	0 m/s	0.75 m/s
Pressure	-110 kPa	-108 kPa

Table 4.6: Summary of case 2 with an endovascular coil

Endovascular coiling was deemed the best treatment for case 2, due to its superior performance in decreasing TA-WSS from 0.262 Pa to 0.0326 Pa and reducing OSI from 0.246 to 0.0642, roughly an 80% decrease.

However, two rupture locations remain, with a notable shift in their positions, as denoted by the black circles in Figure 4.61. The primary rupture location, as denoted by point 1, has shifted to the lower-right lobe, resulting from stagnating flow due to the placement of the coil. The secondary rupture location, as denoted by point 2, is now identified at the neck of the aneurysm, where an isolated elevation in OSI occurs, likely due to the FSI between the coil and blood.

Despite these shifts, the two rupture locations are of considerably lower risk when compared to the baseline and stented case, thanks to the improvements in the haemodynamic profile brought about by the coil.

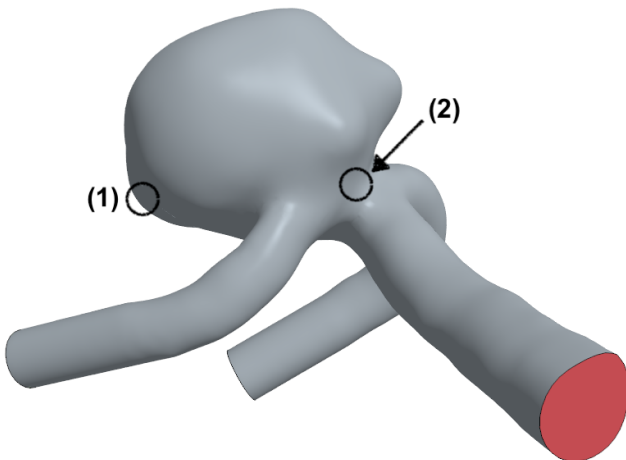


Figure 4.61: Predicted rupture locations for case 2 with a coil

## 4.7 Uncertainty Analysis

The baseline simulations for the untreated aneurysm cases (Section 4.1 and 4.2) were verified against a comprehensive in-vitro dataset provided by the 2013 CFD Rupture Challenge. The untreated simulations achieved an approximate 90% agreement with the best performing entries from the challenge, reinforcing the validity of the simulation. Furthermore, the predicted rupture locations were within a  $\pm 5$  mm margin of the in-silico results, further reinforcing the credibility and accuracy of the simulations.

However, due to the novel addition of endovascular interventions, there exists no in-vitro or in-silico validation data for treated aneurysms at the time of writing. Nonetheless, the modelling and simulation parameters established in the validated untreated scenarios were consistently replicated across all treated cases. The sole modification involved the introduction of a non-slip boundary conditions to represent the surfaces of implanted devices.

Simulations were conducted over two cardiac cycles (1.9 seconds) with a rigid body to ensure computational efficiency. While sufficient for capturing transient flow dynamics, this limited timeframe does not account for the gradual retrusion of the aneurysm sac post-treatment. This constraint significantly affects the reliability of RRT values, which reached anomalously high magnitudes in some cases. Consequently, RRT trends are interpreted qualitatively rather than quantitatively, acknowledging an uncertainty margin of approximately  $\pm 15\%$ .

While OSI distributions were considered reliable under the assumption of laminar flow, it must be noted that the flow regime within aneurysms remains a subject of ongoing research. G. Ferguson (Ferguson 1970) suggests that flow disturbances induced by stents may lead to turbulence-like behaviour, even at low Reynolds numbers of 400. This indicates that OSI values might be underestimated in regions affected by device induced flow mixing.

Lastly, the study utilised a generic, literature-based cardiac cycle profile, as patient-specific inflow conditions could not be integrated due to ethical constraints and the unavailability of clinical data. As such, this study does not capture variations induced by individual health factors such as hypertension or smoking. This limitation restricts the personalisation of the simulations and must be considered when interpreting the results.

## 4.8 Comparative Quantitative Analysis

This section presents a comparative quantitative analysis of the results discussed in the previous section. Its objective is to provide a side-by-side evaluation of the haemodynamic effects observed across different cases and treatment scenarios. The analysis is categorised into the following subsections for clarity and comparison:

**Comparison 1:** Case 1 vs. Case 2

**Comparison 2:** Case 1 vs. Case 1 (stent) vs. Case 1 (coil)

**Comparison 3:** Case 2 vs. Case 2 (stent) vs. Case 2 (coil)

Front views of key parameters (TA-WSS, OSI, RRT, Streamlines) are provided for direct visual comparison. In addition, supplementary views are included to highlight specific regions of interest.

### 4.8.1 Case 1 vs. Case 2

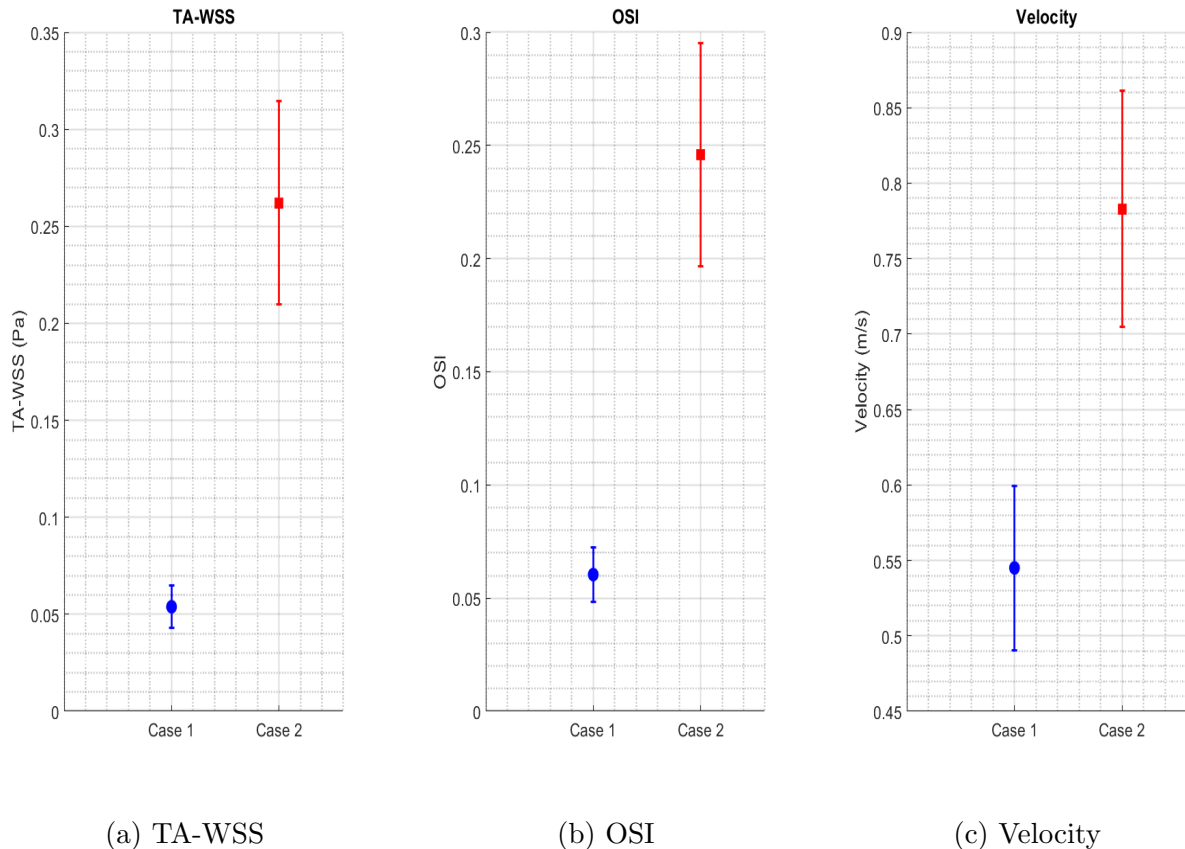


Figure 4.62: Quantitative comparison of parameters

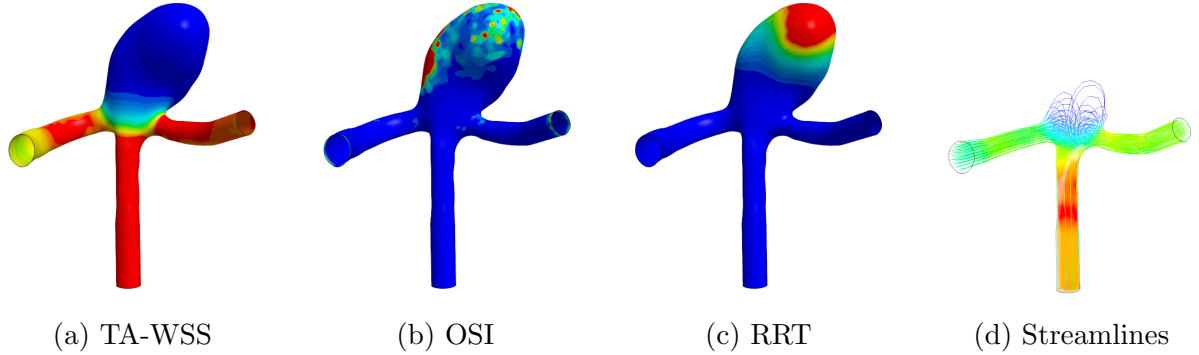


Figure 4.63: Visualisation of results for case 1

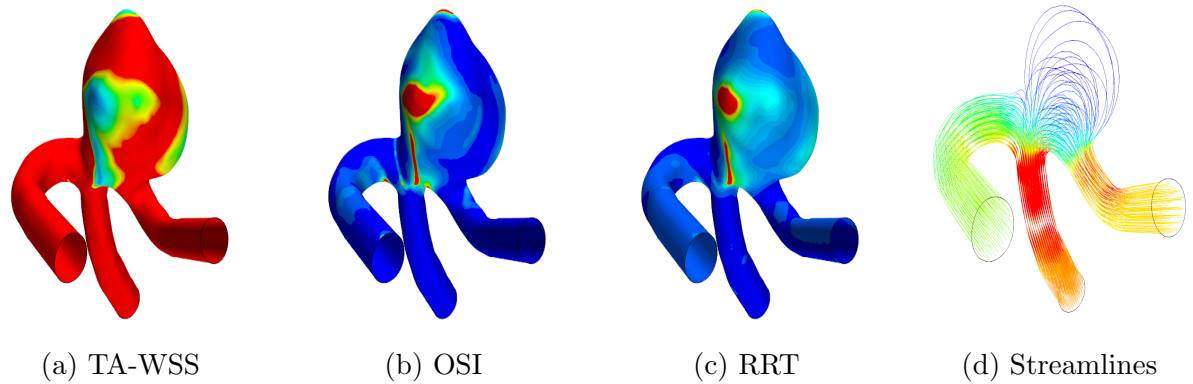


Figure 4.64: Visualisation of results for case 2

Figure 4.63 and 4.64 showcase an overview of the results for case 1 and case 2 respectively. It is evident from the MATLAB plots (Figure 4.62) that case 1 (blue circle marker) experiences significantly lower maximum TA-WSS, OSI, and velocity than case 2 (red square marker).

Comparing the TA-WSS scenes, as denoted by Figure 4.63(a) and 4.64(a), it is concluded that case 1 exhibits a smooth, gradual transition between high and low shear stress regions, as indicated by the green hue at the neck. This smooth gradient suggests more stable flow conditions in the unruptured aneurysm. In contrast, case 2 displays a much sharper and abrupt transition, with a steep gradient that indicates heightened shear stress in case 2. The maximum TA-WSS recorded in case 1 was 0.0539 Pa, whereas in case 2 it was significantly higher at 0.262 Pa.

When referring to the OSI scenes, as denoted by Figure 4.63(b) and 4.64(b), the OSI scenes show that case 1 has a broader distribution of relatively low OSI values, with the highest recorded value being 0.0604 at the left side of the aneurysm. This suggests more stable, unidirectional flow. In contrast, case 2 exhibits significantly higher OSI values at the lobes, with the maximum value recorded of 0.246 at the frontal lobes, a magnitude four times greater than that of case 1.

The RRT scenes, as denoted by Figure 4.63(c) and 4.64(c), further enhance the perception that case 2 is more likely to rupture due to the large gradients of residence time experienced at the lobes of the aneurysm as denoted by the teal hues. Streamline views, as denoted by Figure 4.63(d) and 4.64(d), showcase blood flows at noticeably higher velocities in case 2, with the maximum velocity recorded at 0.783 m/s, compared to the maximum velocity of 0.534 m/s observed in case 1.

To conclude, the haemodynamic parameters in case 2 (the multi-saccular aneurysm) are significantly greater than those in case 1 (the single-sac aneurysm). This suggests that case 2 is comparatively more prone to rupture. The predicted rupture location for case 2 was identified as the frontmost lobe, as mentioned in Section 4.2.7

#### 4.8.2 Case 1 vs. Case 1 (stent) vs. Case 1 (coil)

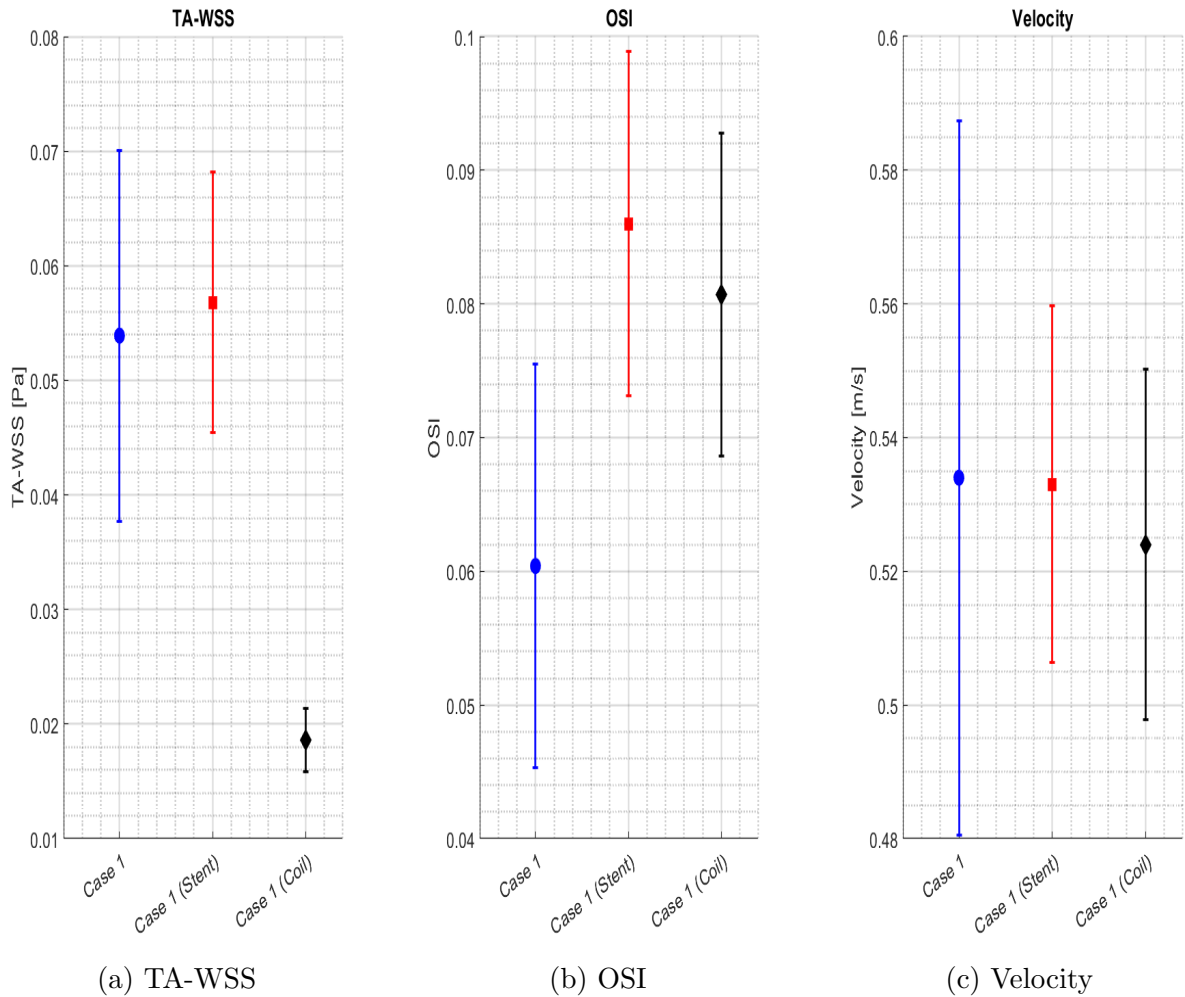


Figure 4.65: Quantitative comparison of parameters

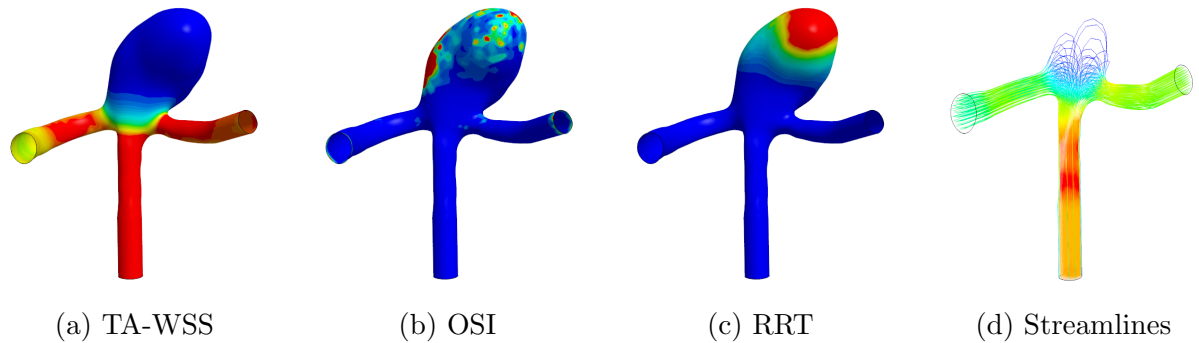


Figure 4.66: Visualisation of results for case 1

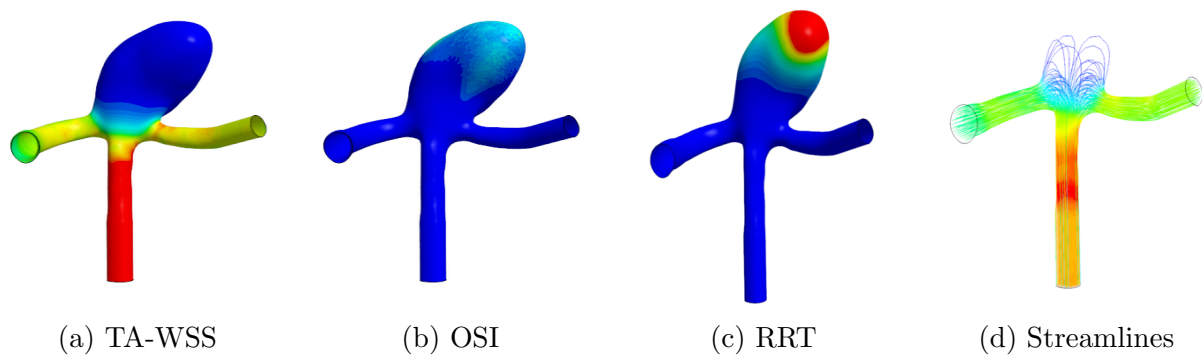


Figure 4.67: Visualisation of results for case 1 with a stent

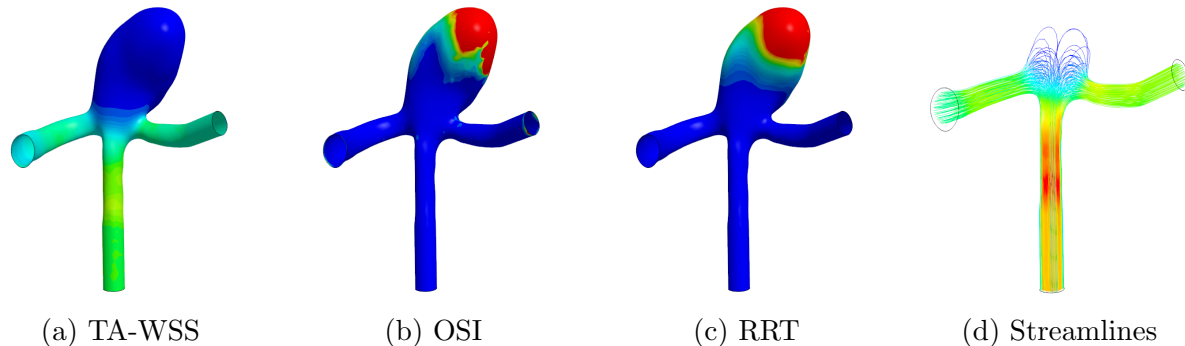


Figure 4.68: Visualisation of results for case 1 with an endovascular coil

Figure 4.66, 4.67, and 4.68 showcase an overview of the results of case 1 untreated, case 1 treated with a flow diversion stent, and case 1 treated with an endovascular coil, respectively. Figure 4.65 showcases a quantitative comparison of MATLAB plots for all three sections, case 1 is denoted by the blue circle markers on the left, case 1 with a stent is denoted by the red square markers in the middle, lastly, case 1 with a coil is denoted by the black diamond markers on the right.

It is important to note that these treatments are being applied to a relatively low baseline as case 1 exhibited a low maximum TA-WSS of 0.07 Pa and an OSI of 0.0604. As such, the net effect of preventive treatment is anticipated to be minimal.

Addressing the TA-WSS distributions, the coil treatment results in a substantial reduction in WSS as denoted by Figure 4.68(a), given the green hue and corresponding MATLAB plots it is calculated to have decreased by 65.5%. For the stent, a localised increase in TA-WSS is observed at the aneurysm neck which is slightly higher than the untreated case by 3 mPa, and therefore negligible. This trend is likely a result of the fluid-structure interaction between the flow and coil, due to its placement around the neck, resulting in localised higher WSS regions. However, a broader reduction in average TA-WSS is still evident, with more yellow hues extending across the branches as seen in Figure 4.67(a).

In terms of OSI, both treatments lead to an overall decrease in the average OSI around the sac, especially in the stent treatment as denoted by Figure 4.67(b). Nevertheless, localised regions of elevated OSI still appear, especially in the coiled geometry. Referring to Figure 4.65, the MATLAB plots suggest a minor increase in maximum OSI of 0.025, the general sac averaged OSI is reduced in both cases, which is of more importance.

Streamline analysis reveals minimal impact on the primary flow paths as shown by Figure 4.66(c), 4.67(c), and 4.68(c). Maximum velocity in the untreated case is recorded at 0.534 m/s. Following stenting, this slightly drops to 0.533 m/s, while the coil treatment yields the most noticeable reduction, with a maximum velocity of 0.524 m/s.

To conclude, both treatments achieve beneficial reductions in haemodynamic parameters. However, the emergence of small, isolated regions with elevated TA-WSS and OSI suggests that these improvements are limited. The flow diversion stent emerges as the more suitable intervention for a wide-neck, single-saccular aneurysm such as case 1. Due to the already low-risk nature of the untreated baseline case, the net benefit from either intervention appears marginal.

#### 4.8.3 Case 2 vs. Case 2 (stent) vs. Case 2 (coil)

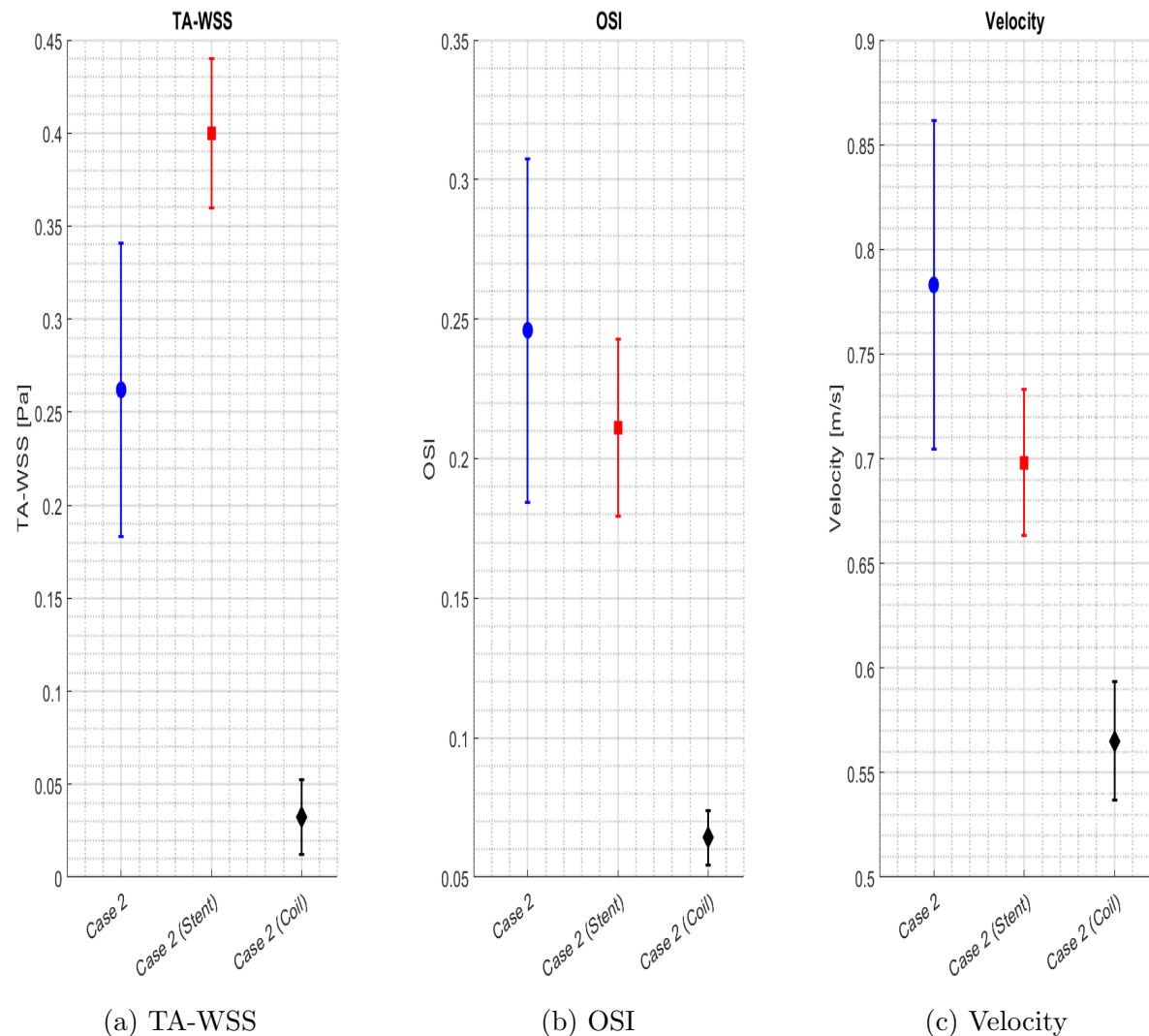


Figure 4.69: Quantitative comparison of parameters

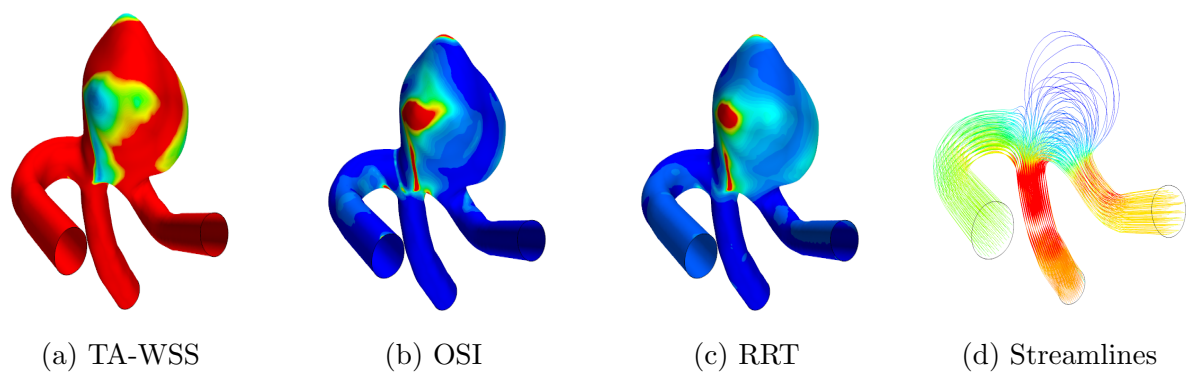


Figure 4.70: Visualisation of results for case 2

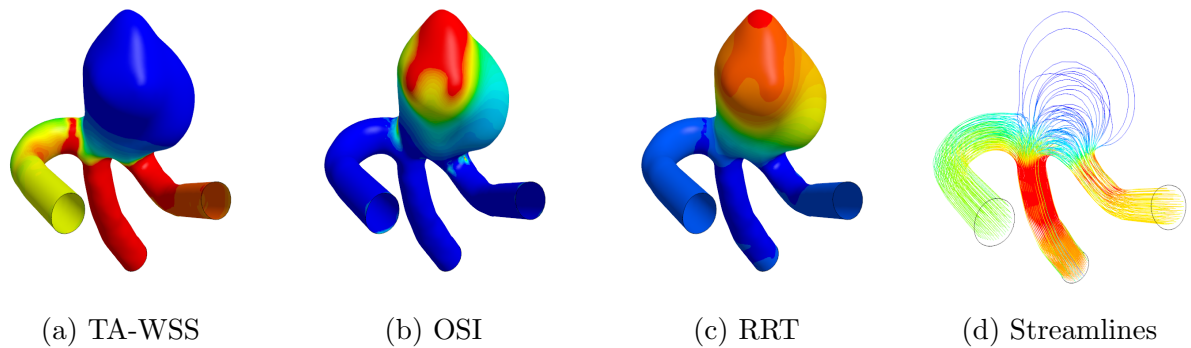


Figure 4.71: Visualisation of results for case 2 with a stent

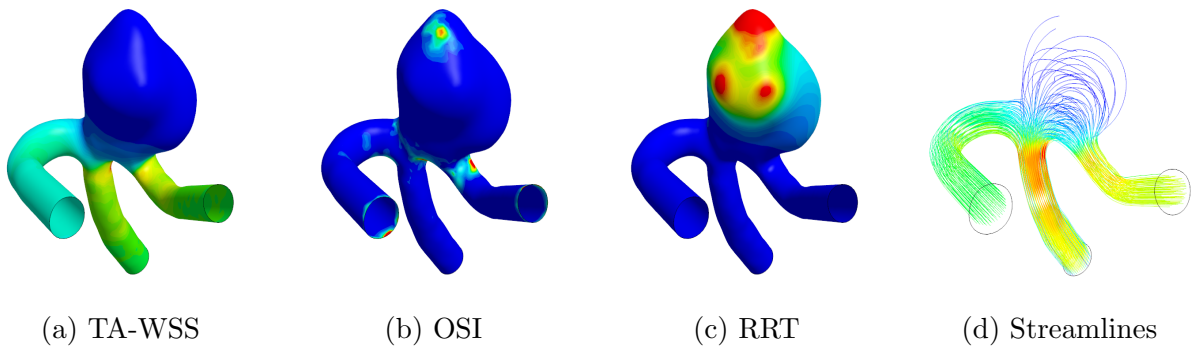


Figure 4.72: Visualisation of results for case 2 with an endovascular coil

Figure 4.70, Figure 4.71, and Figure 4.72 present an overview of the results for case 2 in the untreated state, following treatment with a flow-diverting stent, and an endovascular coil, respectively. As previously described, case 2 is characterised by a multi-saccular aneurysm with a narrow neck measuring 3 mm. The MATLAB plots in Figure 4.69 indicate that coiling treatment leads to a substantial reduction across all haemodynamic parameters.

TA-WSS scenes showcase a general decrease in average WSS following both treatments, however the maximum TA-WSS recorded for the stented condition is 0.4 Pa, which is higher than the baseline value of 0.262 Pa. This is due to the fluid-structure interaction resulting in a localised region of elevated TA-WSS at the neck, as shown in Figure 4.71(a). For the coiled case, the maximum TA-WSS has dropped to 0.0326 Pa, a decrease of 87.54%, and is shown by the blue-teal hue in Figure 4.72(a).

OSI scenes showcase a decrease in maximum OSI from the baseline of 0.246 for both treatments. The stented case decreased OSI to 0.211, while the coiled case decreased OSI to 0.0362, a drop of 86.7%. Although the maximum OSI has decreased for both, it is evident that there is a large region of elevated OSI at the topmost lobe for the stented case, as shown by the red hue in Figure 4.71(b). In contrast, the coiled case exhibits a substantial decrease in OSI, as shown by the blue coloured sac in Figure 4.72(b).

The RRT scenes illustrate an increase towards the upper lobes of the aneurysm following treatment. This effect is more pronounced in the coiled case, as shown in Figure 4.72(c), and aligns with the expected response, where flow stagnation promotes thrombus and clotting of blood, ultimately sealing the aneurysm sac, preventing blood from entering.

Streamlines scenes show the velocity profile of blood within the aneurysm. The untreated case recorded a maximum velocity of 0.783 m/s, while the stented case had a maximum of 0.698 m/s, which results in a minor drop of 0.085 m/s. In contrast, the coiled case resulted in a maximum velocity of 0.565 m/s, resulting in a substantial drop of 0.218 m/s, this is shown by the yellow hue present at the branches in Figure 4.72(d).

In conclusion, these simulations suggest that endovascular coiling would be the preferred treatment option for aneurysms with the morphological characteristics of case 2, specifically narrow-necked and multi-saccular configurations, due to its superior ability to disrupt blood flow and effectively seal of the aneurysm.

# Chapter 5

## Conclusions

This study has demonstrated the effectiveness of CFD in analysing the rupture risk and evaluating treatment options for patient-specific intracranial aneurysms. By modelling two distinct aneurysm geometries, key haemodynamic parameters were extracted to localise potential rupture regions and assess post-treatment haemodynamic outcomes using both flow diversion stents and endovascular coiling.

Additionally, this study applied a three-parameter approach, comparing haemodynamic factors quantitatively to better understand their interplay and identify potential rupture locations, which were flagged as cautionary areas. This provides neurosurgeons and physicians with essential pre-treatment information that can ultimately improve patient outcomes. The novelty of this approach lies in the application of stents and coils, allowing medical professionals to simulate treatments and better understand their long-term effects, perform comparative analysis, and visualise blood flow dynamics. The ability to simulate device insertion in-silico equips clinicians with a powerful tool to anticipate treatment outcomes, refine intervention strategies, and make life-critical decisions. This patient-specific, simulation-driven approach enables tailored, evidence-based treatment selection, reducing recurrence rates and improving overall patient outcomes.

The results indicate that case 1, with its regular single-sac shape and wide neck (5 mm), exhibited more stable haemodynamic profiles, making it less likely to rupture. In contrast, case 2 is significantly more prone to rupture due to its irregular, multi-lobed morphology and narrow neck (3 mm). This conclusion is supported by the haemodynamic parameters, where the maximum TA-WSS gradient was 0.0539 Pa for case 1 and 0.262 Pa for case 2. Similarly, the maximum OSI values were 0.0604 and 0.246 for case 1 and case 2, respectively. The values for case 2 are more than four times greater than those for case 1, reinforcing the conclusion that case 2 is quantitatively more prone to rupture.

Furthermore, the study indicates that flow diversion stents are the recommended treatment for aneurysms with a morphology similar to case 1, as stents were the most effective treatment option in this case. This conclusion is further supported by the decrease in average TA-WSS and OSI around the sac, as well as the minimisation of localised regions of elevated OSI. However, the results were not statistically significant due to the baseline parameters in case 1 being already low.

In contrast, endovascular coiling is recommended for aneurysms resembling the characteristics of Case 2, where coiling treatment resulted in an 87.54% decrease in the TA-WSS gradient and an 86.7% reduction in OSI. This is primarily due to the superior ability of endovascular coiling to effectively seal the blood flow circulating within the multiple lobes of the aneurysm. These results will directly impact the way clinicians approach aneurysm treatment in practice.

These findings align with the clinical methodologies currently used by neurosurgeons, who often employ stents in wide-neck aneurysms and coiling for narrow-neck aneurysms to ensure that the coils do not leave the sac post-treatment. However, the role of the number of lobes and irregular shapes in treatment selection is frequently overlooked. This study helps to clarify the importance of these morphological features, contributing to a better understanding of aneurysm behaviour and ultimately improving patient outcomes.

This study has projected the following as potential thresholds values towards an intracranial aneurysm rupture:

- **WSS Sac Gradient > 0.25 Pa or 2.5 dyn/cm<sup>2</sup>**
- **Maximum OSI > 0.24**
- **Velocity > 1.0 m/s**

Moreover, the ability to simulate device insertion in-silico provides clinicians with a powerful tool to anticipate treatment outcomes and refine intervention strategies. This patient-specific, simulation-driven approach allows for tailored, evidence-based treatment selection, which can ultimately reduce recurrence rates and improve patient outcomes.

Lastly, the study developed JavaScript macros to automate both pre-processing and post-processing tasks. This yields an output haemodynamic diagnostic scene in as little as six hours, making CFD analysis more accessible for use in clinical environments, especially in time-sensitive contexts such as aneurysm management. These automation tools serve as a bridge between advanced simulation techniques and practical clinical application, marking a significant step toward real-time CFD-assisted diagnosis and treatment planning.

## 5.1 Future Work and Limitations

Despite these promising results, several limitations remain:

**Limited sample size:** Threshold values were derived from only two patient-specific aneurysms. While trends were observed, a larger dataset is necessary to statistically validate these haemodynamic thresholds. Expanding the case study pool is now feasible thanks to the automated macro system developed in this project, which significantly reduces computational workload and time.

**Generic patient parameters:** This study utilised average cardiac cycle profiles and standardised blood properties, which limits its ability to account for individual variations such as hypertension, irregular heart rhythms, haematological disorders, smoking habits, and gender differences. Incorporating patient-specific data (e.g. from medical records) would enhance the personalisation of CFD outputs and improve clinical accuracy. Ethical approval constraints limited access in this study.

**Rigid wall assumption:** Due to computational constraints, the aneurysm sac was assumed to be rigid. While justified in literature for short-term analysis, this simplification neglects the sac retrusion post-treatment. Incorporating deformable models in future work will improve accuracy, especially for long-term outcome prediction.

**RRT limitations:** Relative residence time results were difficult to compare quantitatively across cases due to the short simulation duration of two cardiac cycles (1.9 seconds). Extending simulation time and increasing temporal resolution would yield more reliable RRT values and enhance comparative analysis.

**Turbulence modelling:** This study assumed laminar flow. While generally valid in blood circulation, emerging hypotheses suggest potential low-Reynolds-number turbulence due to interactions between blood and treatment devices (Ferguson 1970). Including turbulence modelling in future CFD frameworks could capture more complex flow dynamics, though experimental validation is still required.

**Anatomical scope:** The methodology employed in this study can be applied to various types of aneurysms. Although this research focused on intracranial saccular aneurysms located at the base of the brain in the circle of Willis, similar approaches could be extended to other aneurysm types with comparable mortality rates. For instance, Thoracic Aortic Aneurysms (TAA) and Abdominal Aortic Aneurysms (AAA), located along the aorta, present similar clinical challenges.

**Fusiform Aneurysms** The study focused on saccular aneurysms, which, as shown in Figure 5.1(a), are the most common morphology, accounting for approximately 90% of all intracranial aneurysms (Koutsouhanasis and Sampath 2020). The remaining 10% are fusiform in shape, as illustrated in Figure 5.1(b). To gain a more comprehensive understanding of aneurysms across various morphologies and locations, it is recommended that this study be extended to include a wider range of aneurysm types. Unfortunately, this was not feasible in the present study due to the limited availability of patient-specific data and the challenges associated with accessing such data.

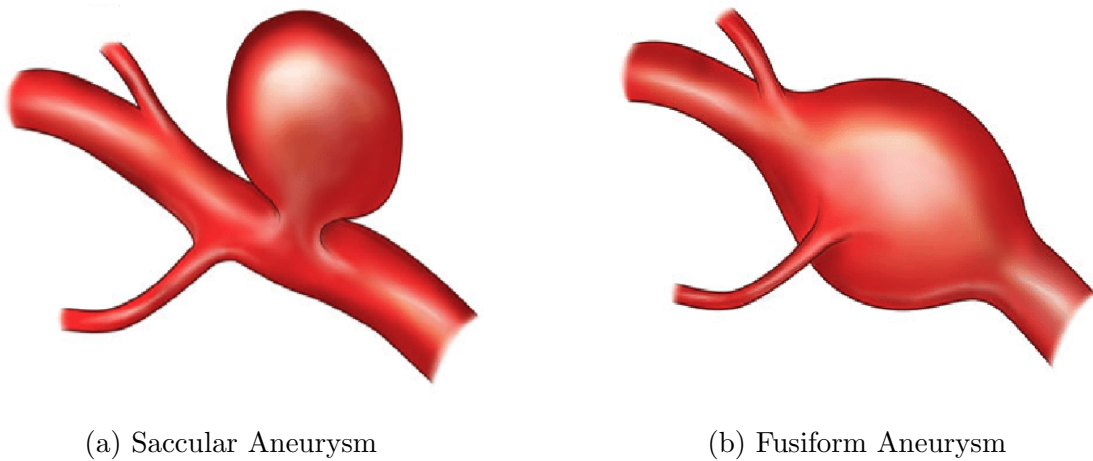


Figure 5.1: Representation of aneurysm shapes (Withers et al. 2013)

## 5.2 Recommendations and Applications

**Clinical adoption:** Hospitals should consider integrating CFD into aneurysm treatment planning. The automated macro system developed in this study provides an efficient and clinically viable pathway for adoption. This integration would enable the personalisation of treatment, allowing for tailored interventions that improve patient outcomes and enhance the effectiveness of surgical procedures, by streamlining the crucial decision-making process.

**AI-powered imaging:** The large dataset produced by CFD simulations could be integrated into a machine learning model capable of accurately predicting rupture risk using linear regression classification. This approach would reduce reliance on time-consuming CFD simulations, shifting towards an image learning algorithm that can account for critical morphological characteristics, such as sac diameter, neck width, and the number of lobes. Such a model would enhance current aneurysm risk calculators, which are often outdated and rely on a limited number of patient-specific cases, ultimately improving the accuracy and efficiency of risk assessments.

**Aneurysm Classification:** Threshold-based risk classification (e.g., OSI > 0.24) could be formalised into clinical guidelines, enabling the prioritisation of high-risk aneurysms. This would help reduce waiting times and improve patient management systems, leading to more timely and effective interventions.

**Device optimisation:** Manufacturers could leverage CFD simulations to design next-generation stents and coils tailored to diverse aneurysm geometries. In addition, these simulations can support the research and development (R&D) of newer endovascular techniques, potentially extending beyond aneurysms to other cardiovascular conditions, such as cardiac stent design or vascular surgeries, promoting advancements in personalised treatment across cardiovascular care. Moreover, CFD can be used to test and optimise new materials for medical devices, enabling the development of more effective, durable, and biocompatible devices tailored to individual patient needs.

**Regulatory Approval:** CFD generates valuable in-silico data that can expedite the regulatory approval process typically required by the BSI and FDA for biomedical devices. By providing detailed virtual simulations, CFD has the potential to streamline the approval timeline, making it more efficient. Furthermore, the use of CFD data could reduce reliance on both animal and human testing, fostering a more ethical and cost-effective approach to the development of medical devices. This could allow emerging technologies, such as the Woven EndoBridge (WEB) device shown in Figure 5.2, to reach the market more quickly.

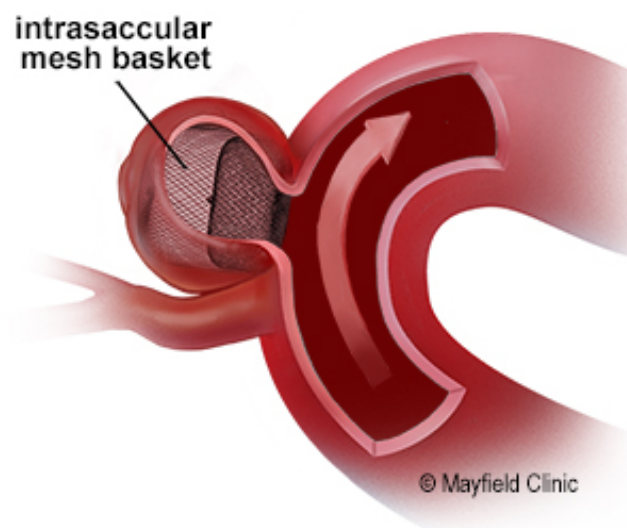


Figure 5.2: Woven EndoBridge device (Mayfield Clinic 2015)

# Chapter 6

## Management

### 6.1 Project Plan and Reflection

The project was successfully completed within the allocated timeframe, with all stated aims and objectives being fully achieved. Certain tasks, such as the simulations, progressed ahead of schedule due to access to the Computational Shared Facility (CSF4) and High Performance Computing (HPC) resources provided by the University of Manchester. Although minimal work was originally scheduled during the winter break, the ability to run simulations remotely through CSF4 enabled these tasks to be completed two weeks earlier than planned.

In contrast, some components, including the literature review, poster, and the dissertation drafts, required more time than initially anticipated. These tasks frequently extended beyond the planned schedule by around one week.

Overall, the project deliverables remained consistent with those outlined in the planned Gantt chart. The only notable change was the addition of a new task: preparing the study for submission to the journal *Scientific Reports*. This task is scheduled to begin in the week commencing 26th May 2025 and is expected to continue until 13th June 2025, and is shown in Figure ???. The project timeline was largely consistent with the original plan. The main differences were the early completion of the simulation tasks, as these were completed within 6 to 8 hours, compared to the initially estimated duration of over 15 hours, and the additional time required for the report preparation.

The Gantt charts presented in Appendix A illustrate the full project plan. The initial Gantt charts did not account for constraints arising from other commitments and deliverable deadlines; these omissions were addressed and corrected in the planned and final Gantt charts.

## **6.2 Future Work**

While the project was completed on time and met all deliverables, the initial project plan underestimated the time required for the literature review and academic writing stages. Future projects will therefore include more generous scheduling for these components, particularly when engaging with unfamiliar or interdisciplinary material. Timeboxing proved to be a highly effective time management strategy and will continue to be used, particularly for structuring longer-term tasks such as drafting and data analysis. Additionally, the integration of contingency buffers will become standard practice to mitigate the impact of unexpected technical setbacks or competing academic commitments. These refinements will improve the resilience of future project timelines and contribute to higher-quality outcomes. Overall, this project has been both technically and personally rewarding, and the lessons learned will be directly applied in the author’s forthcoming MSc thesis and potential academic publication.

## **6.3 Ethical Approval and University Policy**

This study did not involve direct interaction with human participants or personal health data. As such, it did not require formal ethical approval from the University Research Ethics Committee. However, the project adhered strictly to The University of Manchester’s policies on the ethical use of publicly available data. The aneurysm geometries used were anonymised and sourced from the CFD Rupture Challenge 2013 dataset, with explicit permission granted for academic use. All simulations and computational work were conducted in accordance with the University’s code of practice for research integrity and responsible data handling, ensuring compliance with data security protocols.

# Appendix A

## Gantt Charts

This section presents the Gantt charts that guided the project timeline across different phases. For clarity, each chart set is split into Semester 1 and Semester 2.

- **Final Gantt Charts** – updated on 30th April 2025 (Figures 6.2 and 6.3)
- **Planned Gantt Charts** – created on 21st October 2024 (Figures 6.4 and 6.5)
- **Initial Gantt Charts** – created on 6th October 2024 (Figures 6.6 and 6.7)

All tasks and deliverables were organised into the following work packages for clarity and simplicity, these work packages were colour-coded, as shown in the legend in Figure ??.

Work Package	Colour
LR: Literature Review	Yellow
Case 1	Light Blue
Case 2	Light Orange
Deliverables	Purple
Prerequisites for CFD/Report	Light Green
Poster	Pink
Report	Green

Figure 6.1: Work package legend

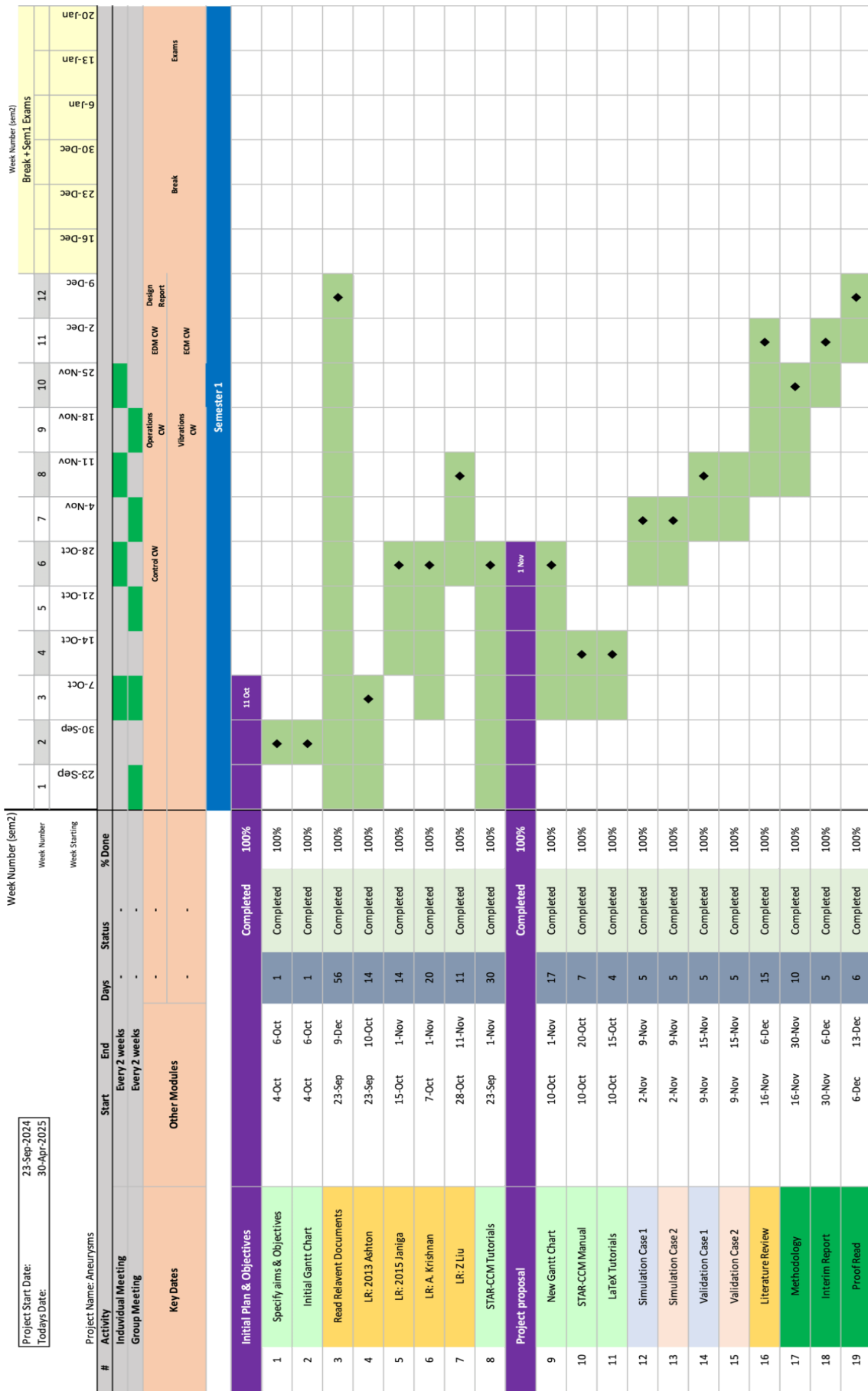


Figure 6.2: Final Gantt Chart – Semester 1

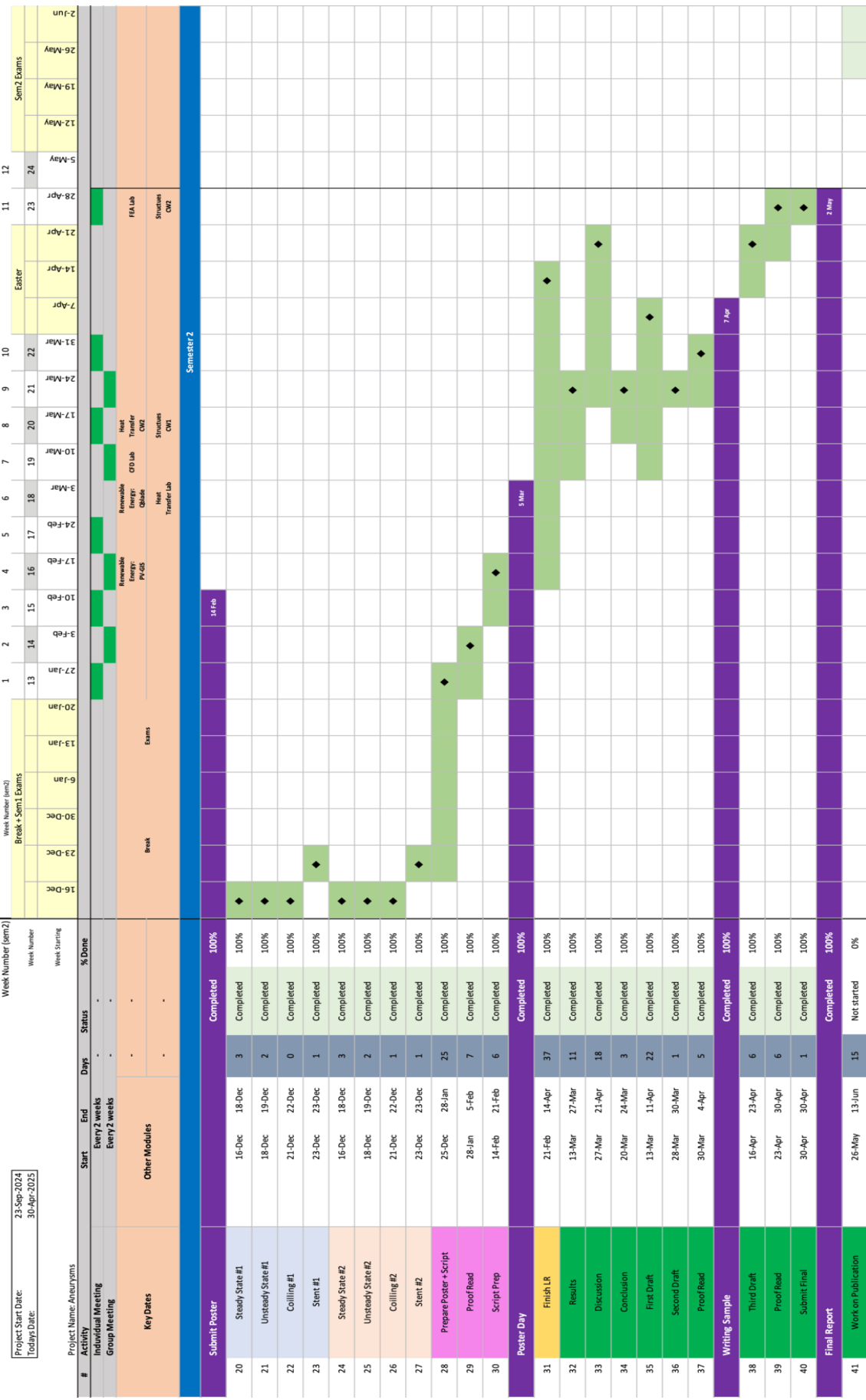


Figure 6.3: Final Gantt Chart – Semester 2

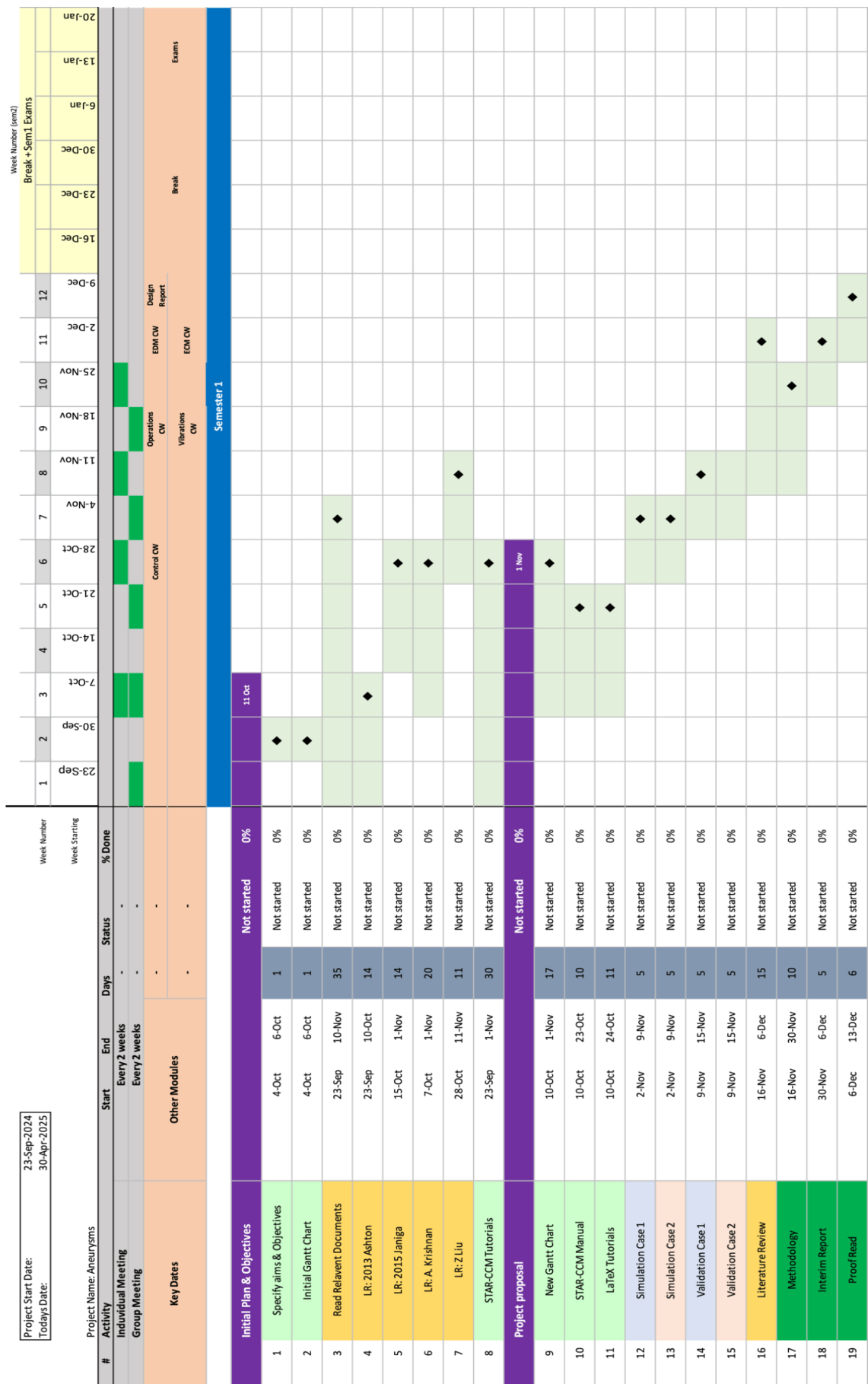


Figure 6.4: Planned Gantt Chart – Semester 1

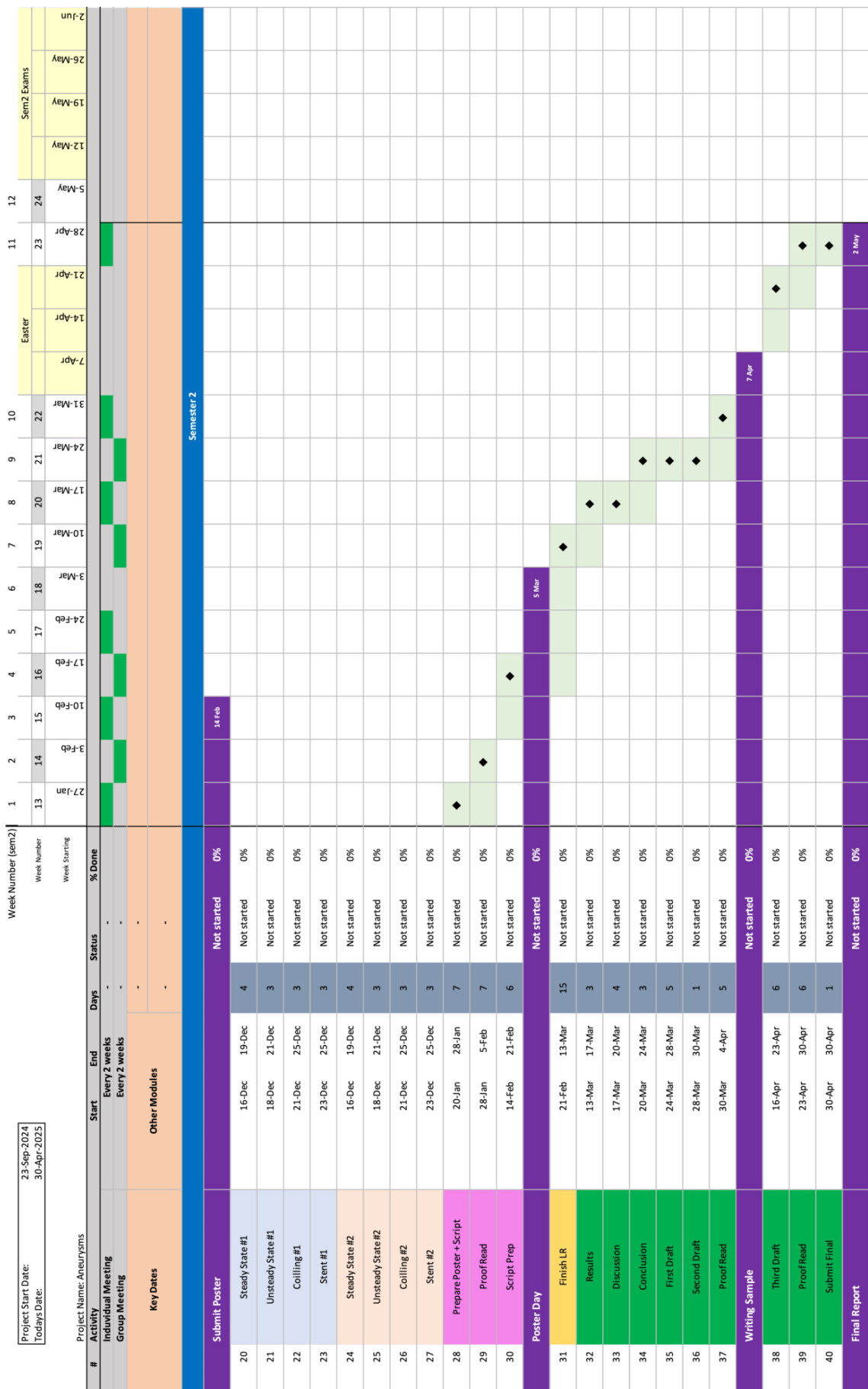


Figure 6.5: Planned Gantt Chart – Semester 2

# Initial Gantt Chart - Semester 1

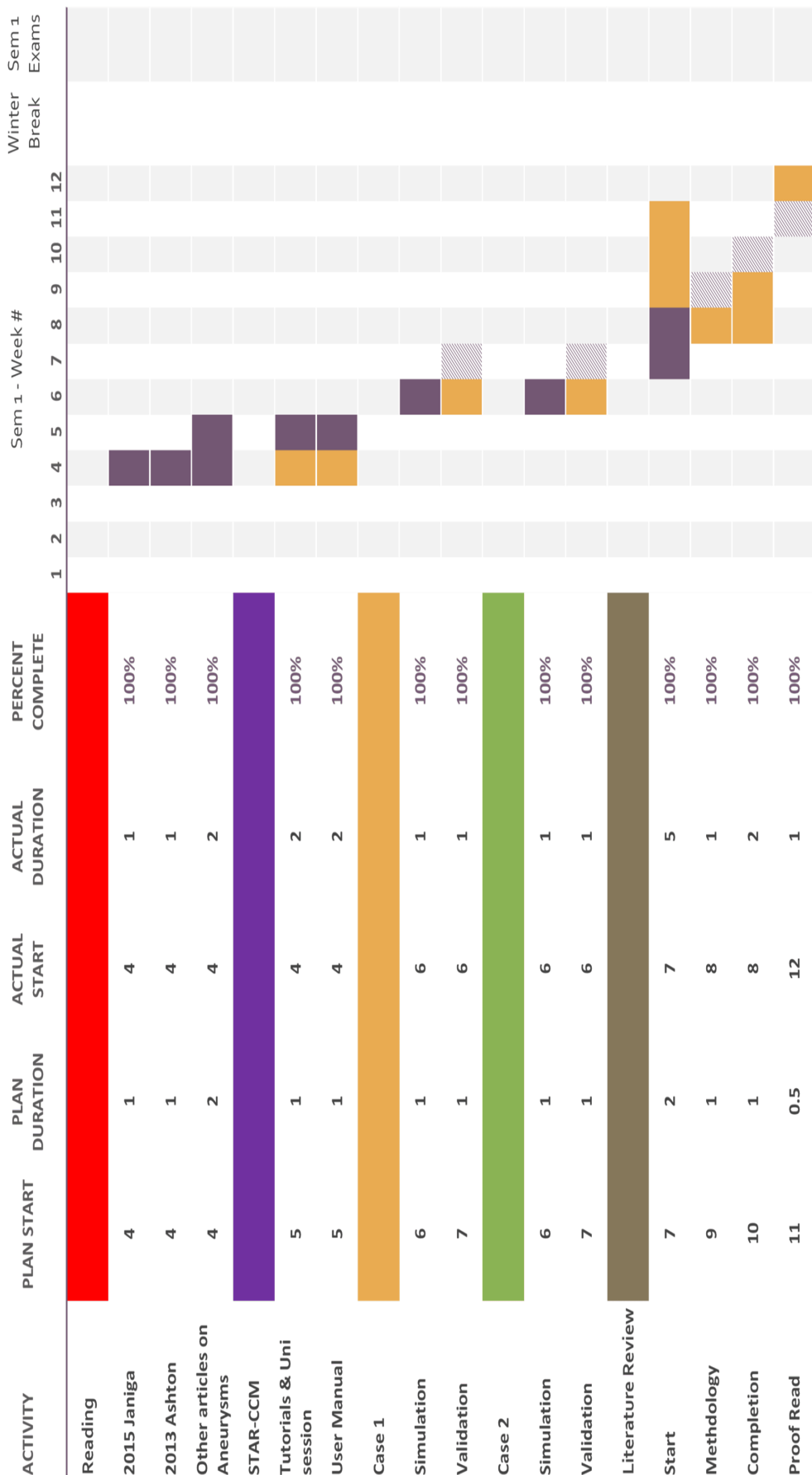


Figure 6.6: Initial Gantt Chart – Semester 1

## Initial Gantt Chart - Semester 2

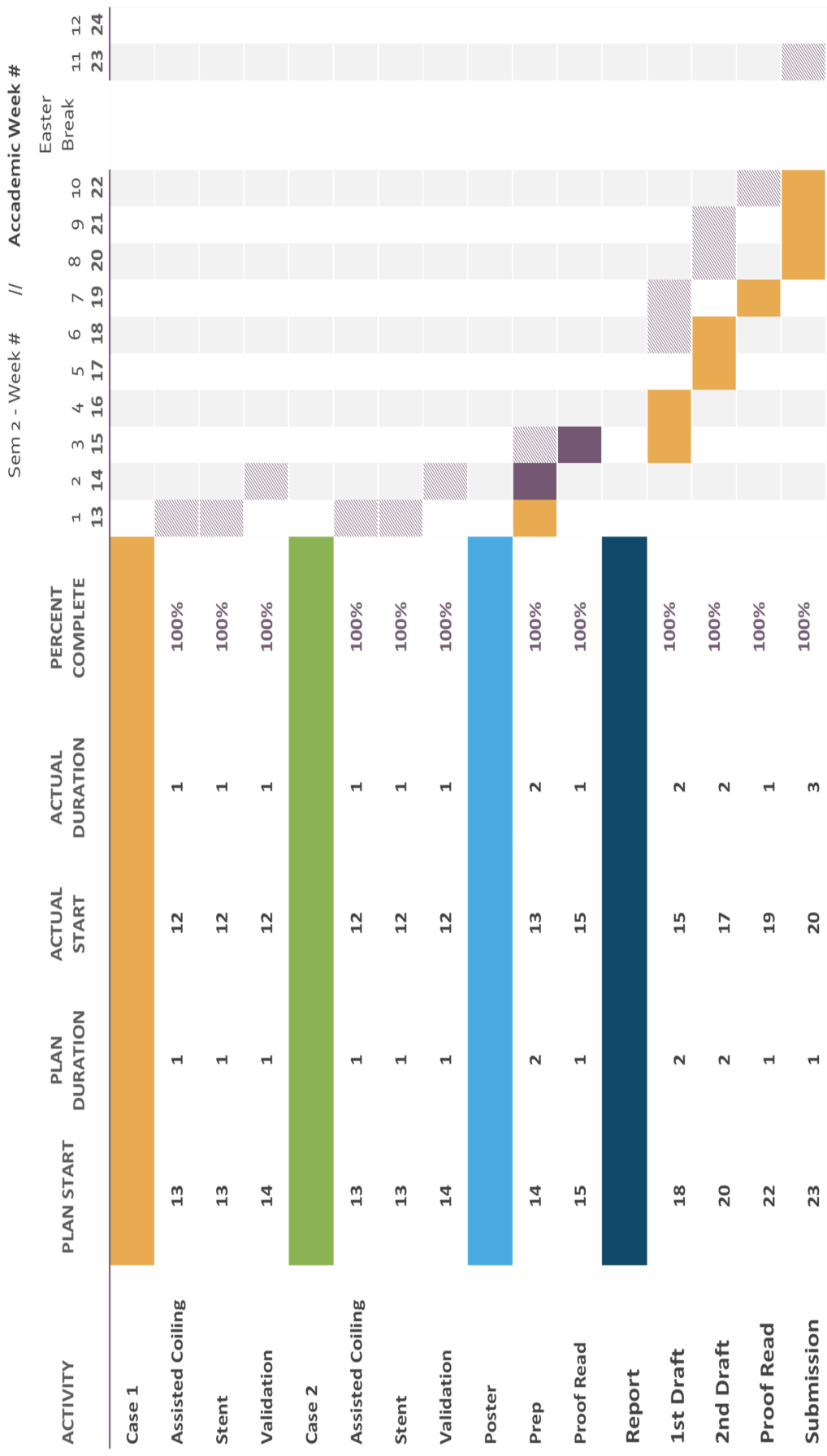


Figure 6.7: Initial Gantt Chart – Semester 2

# Appendix B

## Risk Assessment

The risk assessment process involved the construction of a risk matrix, presented in Figure 7.1, with the corresponding legend shown in Figure 7.2.

Risk	Likelihood (1–5)	Impact (1–5)	Risk Score (LxI)
Time management	2	2	4
Model errors from incorrect segmentation	3	2	6
Software failure or licensing issues	2	4	8
Semester 2 deliverables and other commitments	2	5	10
Data loss or corrupted files	3	5	15
High computational cost	5	5	25

Figure 7.1: Risk Matrix

Risk Score	Category	Colour	Description
1-9	Low	Green	Acceptable risk, monitor periodically.
10-19	Moderate	Yellow	Requires action and mitigation
20-25	Critical	Red	Unacceptable, immediate action and contingency

Figure 7.2: Legend for Risk Matrix

The following mitigation strategies were implemented to address the identified risks:

- **Time management:** Timeboxing strategies were applied, with calendars regularly updated and Gantt charts adjusted to ensure the project remained on schedule.
- **Model errors from incorrect segmentation:** STL geometries underwent pre-import validation using Blender and MeshLab to ensure topological accuracy and watertight meshes, thereby minimising import failures on STAR-CCM+.
- **Software failure or licensing issues:** No mitigation strategy was implemented, as these occurrences were considered rare.
- **Semester 2 deliverables and other academic commitments:** A dedicated time allocation of four hours per week was reserved for this project using timeboxing.
- **Data loss or corrupted files:** Version control was maintained using GitHub, with additional backups stored on the University of Manchester OneDrive.
- **High computational cost:** Simulations were executed on the University of Manchester's High Performance Computing (HPC) platform: CSF4, which significantly reduced runtime to approximately 6–8 hours per simulation.

# Appendix C

## Meshes used for the grid independence study

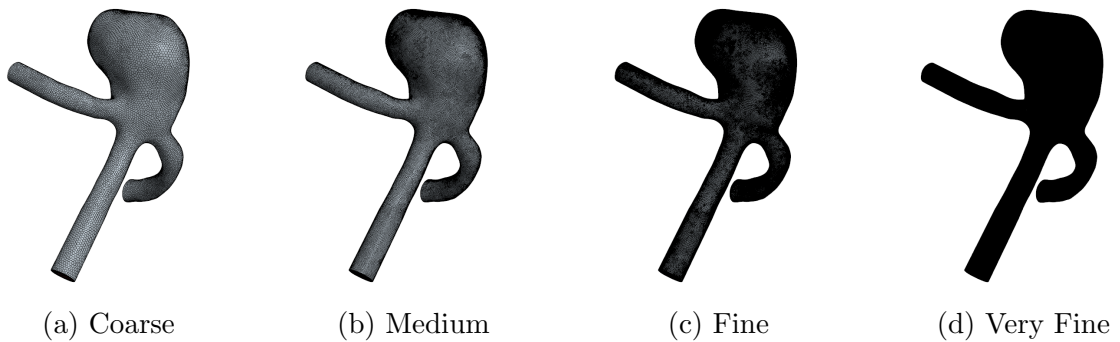


Figure 8.1: Case 1 Polyhedral Meshes

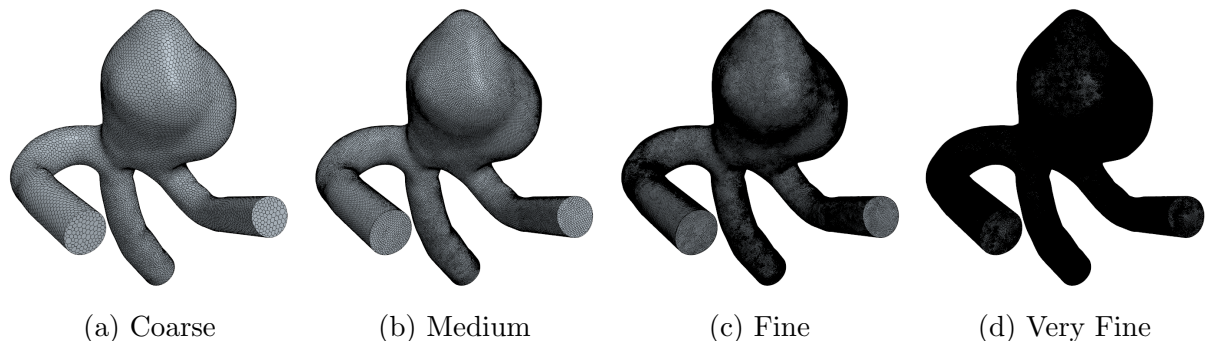


Figure 8.2: Case 2 Polyhedral Meshes

# Appendix D

## User-Defined Field Functions

User-defined field functions for TA-WSS, OSI, and RRT were developed as part of this study. Before defining these field functions, four field sum monitors were first set up. The user field functions were then specified as follows:

### 1. Number of Samples (n)

$$n_{\text{samples}} = \frac{\text{Maximum physical time of stopping criteria}}{\text{Time step}}$$

### 2. Time Averaged Wall Shear Stress (TA-WSS)

$$\text{TAWSS} = \frac{1}{T} \int_0^T [WSS] dt$$

The function for TA-WSS in STAR-CCM+ is expressed as:

$$TAWSS = \frac{\$ \{FieldSumWSSmagMonitor\}}{n_{\text{samples}}}$$

### 3. Oscillatory Shear Index (OSI)

$$\text{OSI} = \frac{1}{2} \left( 1 - \frac{\int_0^T [WSS] dt}{\int_0^T |WSS| dt} \right)$$

In STAR-CCM+, this is calculated using the following expression:

$$OSI = 0.5 \times 1 - \frac{\text{mag}([\$\{FieldSumWSSiMonitor\}], \$\{FieldSumWSSjMonitor\}, \$\{FieldSumWSSkMonitor\}))}{\$\{FieldSumWSSmagMonitor\}}$$

### 4. Relative Residence Time (RRT)

$$\text{RRT} = \frac{1}{(1 - \text{OSI}) \cdot \text{TA-WSS}}$$

The formula for RRT in STAR-CCM+ is given as:

$$RRT = \frac{1}{(1 - 2 \times \$\{OSI\}) \times \$\{TAWSS\}}$$

These user-defined field functions were created and incorporated to facilitate the calculation of the aforementioned parameters during the simulation.

# Appendix E

## GitHub Repository Preview: Macros

The `StarCCM-Aneurysm-Automation` repository contains a set of Java macros designed to automate STAR-CCM+ pre-processing and post-processing workflows for aneurysms. The key files in the repository include:

- `a1continua.java`: Sets up the continuum with blood properties.
- `a2inletvel.java`: Applies a varying velocity profile using external data.
- `a3velocityprobe.java`: Places a velocity probe and generates a graph.
- `a4monitors.java`: Creates monitors for WSS and related metrics.
- `a5fieldfunctions.java`: Defines custom field functions like OSI and WSS.
- `a6meshoperations.java`: Configures mesh operations
- `a8views.java`: Saves isometric screenshots for visualization.
- `a9outlet.java`: Sets outlet conditions.
- `a10scenes.java`: Creates and configures scenes.
- `unsteadyinlet.csv`: Contains velocity-time data for simulations.

For more detailed information, please refer to the repository's `README.md` file.

Repository link: <https://github.com/Dineth5/StarCCM-Aneurysm-Automation>

## GitHub Repository Preview: Aneurysm Sims

The `StarCCM-Aneurysm-Sims` repository contains files used in this study. The repository includes simulation files, geometry files, job scripts, output logs, and output simulations. These files are organized in a manner that allows users to run and manage simulations on the CSF4. The repository was created as a backup to ensure that all the necessary components for running and troubleshooting the simulations are securely stored and easily accessible for future use.

Each simulation folder within the repository typically contains the following files:

- `*.stl`: Geometry file used by STAR-CCM+ to define the simulation mesh.
- `*.sim`: The original, unrun simulation file that contains the setup configuration.
- `*@XXXXX.sim`: A completed simulation file that holds the output from the CSF4 cluster after the simulation run.
- `*.jobscript.sbatch`: A job script file used to submit the simulation to the CSF4 cluster for execution.
- `slurm-*.*.out`: Output log file generated by CSF4, useful for troubleshooting and verifying the successful completion of simulation tasks.

For more detailed information, please refer to the repository's `README.md` file.

Repository link: <https://github.com/Dineth5/StarCCM-Aneurysm-Sims>

# References

- [1].Aoki, T et al. (2011). “PGE2-EP2 signalling in endothelium is activated by haemodynamic stress and induces cerebral aneurysm through an amplifying loop via NF- $\kappa$ B”. In: *British journal of pharmacology* 163.6, pp. 1237–1249.
- [2].Belavadi, Rishab et al. (2021). “Surgical clipping versus endovascular coiling in the management of intracranial aneurysms”. In: *Cureus* 13.12.
- [3].Brain Aneurysm Foundation (2024). *Statistics and Facts*. Accessed: 2025-03-28. URL: <https://www.bafound.org/statistics-and-facts/>.
- [4].Brinjikji, W et al. (2016). “Risk factors for growth of intracranial aneurysms: a systematic review and meta-analysis”. In: *American Journal of Neuroradiology* 37.4, pp. 615–620.
- [5].Castro, MA et al. (2006). “Computational fluid dynamics modeling of intracranial aneurysms: effects of parent artery segmentation on intra-aneurysmal hemodynamics”. In: *American Journal of Neuroradiology* 27.8, pp. 1703–1709.
- [6].Dijk, J Marc C van et al. (2011). “Surgical clipping as the preferred treatment for aneurysms of the middle cerebral artery”. In: *Acta neurochirurgica* 153, pp. 2111–2117.
- [7].Dolan, Jennifer M et al. (2013). “High wall shear stress and spatial gradients in vascular pathology: a review”. In: *Annals of biomedical engineering* 41, pp. 1411–1427.
- [8].Ferguson, Gary G (1970). “Turbulence in human intracranial saccular aneurysms”. In: *Journal of neurosurgery* 33.5, pp. 485–497.
- [9].Friesen, John et al. (2021). “Comparison of existing aneurysm models and their path forward”. In: *Computer Methods and Programs in Biomedicine Update* 1, p. 100019.
- [10].Frösen, Juhana et al. (2019). “Flow-induced, inflammation-mediated arterial wall remodeling in the formation and progression of intracranial aneurysms”. In: *Neurosurgical focus* 47.1, E21.
- [11].Giotta Lucifero, Alice et al. (2021). “Shedding the light on the natural history of intracranial aneurysms: an updated overview”. In: *Medicina* 57.8, p. 742.
- [12].Hashimoto, Nobuo et al. (1987). “Experimental induction of cerebral aneurysms in monkeys”. In: *Journal of neurosurgery* 67.6, pp. 903–905.
- [13].Holdsworth, DW et al. (1999). “Characterization of common carotid artery blood-flow waveforms in normal human subjects”. In: *Physiological measurement* 20.3, p. 219.

- [14].Hopkins, Johns (2018). *Cerebral Aneurysm*. Accessed: 2025-03-31. URL: <https://www.hopkinsmedicine.org/health/conditions-and-diseases/cerebral-aneurysm>.
- [15].Inselspital, Bern University Hospital (2024). *Unruptured Aneurysm of a Cerebral Artery*. Last accessed: April 2025. URL: <https://neurochirurgie.insel.ch/en/diseases-specialities/brain-vessels/aneurysm/unruptured-aneurysm-of-a-cerebral-artery>.
- [16].Janiga, Gabor et al. (2015). “The Computational Fluid Dynamics Rupture Challenge 2013—Phase I: prediction of rupture status in intracranial aneurysms”. In: *American Journal of Neuroradiology* 36.3, pp. 530–536.
- [17].Juvela, Seppo et al. (2008). “Natural history of unruptured intracranial aneurysms: probability of and risk factors for aneurysm rupture”. In: *Journal of neurosurgery* 108.5, pp. 1052–1060.
- [18].Karakas, Hakki et al. (2013). “ITU tailless UAV design”. In: *Journal of Intelligent & Robotic Systems* 69, pp. 131–146.
- [19].Keedy, Alexander (2006). “An overview of intracranial aneurysms”. In: *McGill Journal of Medicine: MJM* 9.2, p. 141.
- [20].Kelsey, Lachlan J et al. (2017). “A comparison of hemodynamic metrics and intraluminal thrombus burden in a common iliac artery aneurysm”. In: *International journal for numerical methods in biomedical engineering* 33.5, e2821.
- [21].Kim, Tackeun et al. (2021). “Higher oscillatory shear index is related to aneurysm recanalization after coil embolization in posterior communicating artery aneurysms”. In: *Acta neurochirurgica* 163, pp. 2327–2337.
- [22].Koutsouhanasis, George A and Raghuram Sampath (2020). “Berry aneurysm”. In.
- [23].Kulkarni, Ashutosh (2023). *Volume Meshing in STAR-CCM+*. Accessed: 2025-05-09. URL: <https://skill-lync.com/student-projects/volume-meshing-in-starccm>.
- [24].Kumar, V. S. and V. S. Kumar (2023). “High Wall Shear incites cerebral aneurysm formation and low Wall Shear stress propagates cerebral aneurysm growth”. In: *Journal of Neurology Research* 13.1, pp. 1–11.
- [25].Lan, Hongzhi et al. (Jan. 2018). “A Re-Engineered Software Interface and Workflow for the Open-Source SimVascular Cardiovascular Modeling Package”. In: *Journal of Biomechanical Engineering* 140.2, p. 024501. ISSN: 0148-0731. DOI: 10.1115/1.4038751. eprint: [https://asmedigitalcollection.asme.org/biomechanical/article-pdf/140/2/024501/5989483/bio\\_140\\_02\\_024501.pdf](https://asmedigitalcollection.asme.org/biomechanical/article-pdf/140/2/024501/5989483/bio_140_02_024501.pdf). URL: <https://doi.org/10.1115/1.4038751>.
- [26].Lebedeva, Elena R et al. (2013). “Migraine before rupture of intracranial aneurysms”. In: *The journal of headache and pain* 14, pp. 1–8.

- [27].Liu, Yongsheng et al. (2017). “Comparison of stent-assisted coil placement and coiling-only for the treatment of ruptured intracranial aneurysms”. In: *Medical Science Monitor: International Medical Journal of Experimental and Clinical Research* 23, p. 5697.
- [28].Machi, Paolo et al. (2019). “Hemodynamics of focal versus global growth of small cerebral aneurysms”. In: *Clinical neuroradiology* 29, pp. 285–293.
- [29].Mascitelli, Justin R et al. (2015). “Predictors of success following endovascular retreatment of intracranial aneurysms”. In: *Interventional Neuroradiology* 21.4, pp. 426–432.
- [30].Mayfield Clinic (2015). *Endovascular Coiling for Brain Aneurysms*. Accessed: 31 March 2025. URL: <https://mayfieldclinic.com/pe-coiling.htm>.
- [31].Mayo Clinic (2023). *Brain Aneurysm — Symptoms and Causes*. Last updated: June 14, 2023. Last accessed: April 2025. URL: <https://www.mayoclinic.org/diseases-conditions/brain-aneurysm/symptoms-causes/syc-20361483>.
- [32].Mayr, Ernst (1961). “Cause and effect in biology: kinds of causes, predictability, and teleology are viewed by a practicing biologist.” In: *Science* 134.3489, pp. 1501–1506.
- [33].Meng, H et al. (2014). “High WSS or low WSS? Complex interactions of hemodynamics with intracranial aneurysm initiation, growth, and rupture: toward a unifying hypothesis”. In: *American Journal of Neuroradiology* 35.7, pp. 1254–1262.
- [34].Mutlu, Onur et al. (2023). “How does hemodynamics affect rupture tissue mechanics in abdominal aortic aneurysm: Focus on wall shear stress derived parameters, time-averaged wall shear stress, oscillatory shear index, endothelial cell activation potential, and relative residence time”. In: *Computers in biology and medicine* 154, p. 106609.
- [35].NHS (2022). *Brain aneurysm - Symptoms*. URL: <https://www.nhs.uk/conditions/brain-aneurysm/>.
- [36].Pougatch, Konstantin and Marvin Weiss (2021). *CFD – Different Mesh Cell Types*. Accessed: 2025-05-09. Coanda Research and Development Corporation. URL: <https://coanda.ca/blog/cfd-mesh-cell-types/>.
- [37].Rahma, Ahmed G and Talaat Abdelhamid (2023). “Hemodynamic and fluid flow analysis of a cerebral aneurysm: a CFD simulation”. In: *SN Applied Sciences* 5.2, p. 62.
- [38].Rand, Peter W et al. (1964). “Viscosity of normal human blood under normothermic and hypothermic conditions”. In: *Journal of applied physiology* 19.1, pp. 117–122.
- [39].Reid, Luke (2021). “An introduction to biomedical computational fluid dynamics”. In: *Biomedical Visualisation: Volume 10*. Springer, pp. 205–222.
- [40].Riccardello Jr, Gerald J et al. (2018). “Influence of relative residence time on side-wall aneurysm inception”. In: *Neurosurgery* 83.3, pp. 574–581.

- [41].Sforza, Daniel M, Christopher M Putman, and Juan R Cebral (2012). “Computational fluid dynamics in brain aneurysms”. In: *International journal for numerical methods in biomedical engineering* 28.6-7, pp. 801–808.
- [42].Sforza, Daniel M, Christopher M Putman, and Juan Raul Cebral (2009). “Hemodynamics of cerebral aneurysms”. In: *Annual Review of Fluid Mechanics* 41.1, pp. 91–107.
- [43].Shimano, Kenjiro et al. (2019). “Understanding of boundary conditions imposed at multiple outlets in computational haemodynamic analysis of cerebral aneurysm”. In: *Journal of Biomechanics* 33.2, pp. 32–42.
- [44].Slob, Marjan J et al. (2005). “Coil thickness and packing of cerebral aneurysms: a comparative study of two types of coils”. In: *American Journal of Neuroradiology* 26.4, pp. 901–903.
- [45].Sosnowski, Marcin et al. (2018). “Polyhedral meshing in numerical analysis of conjugate heat transfer”. In: *EPJ Web of Conferences*. Vol. 180. EDP Sciences, p. 02096.
- [46].Spiegel, Martin et al. (2011). “Tetrahedral vs. polyhedral mesh size evaluation on flow velocity and wall shear stress for cerebral hemodynamic simulation”. In: *Computer methods in biomechanics and biomedical engineering* 14.01, pp. 9–22.
- [47].Staarmann, Brittany et al. (2019). “Shear stress and aneurysms: a review”. In: *Neurosurgical focus* 47.1, E2.
- [48].Terada, Masaki et al. (2016). “Low WSS and high OSI measured by 3D cine PC MRI reflect high pulmonary artery pressures in suspected secondary pulmonary arterial hypertension”. In: *Magnetic Resonance in Medical Sciences* 15.2, pp. 193–202.
- [49].The Royal Children’s Hospital (2020). *Cerebral Aneurysm*. Accessed: 2025-03-31. URL: [https://www.rch.org.au/kidsinfo/fact\\_sheets/Cerebral\\_Aneurysm/](https://www.rch.org.au/kidsinfo/fact_sheets/Cerebral_Aneurysm/).
- [50].Walton (2025). *Brain Aneurysms and Screening*. Tech. rep. Accessed: 31 March 2025. The Walton Centre NHS Foundation Trust. URL: <https://www.thewaltoncentre.nhs.uk/patient-leaflets/brain-aneurysms-and-screening/428318>.
- [51].Wilson, Nathan et al. (2001). “A Software Framework for Creating Patient Specific Geometric Models from Medical Imaging Data for Simulation Based Medical Planning of Vascular Surgery”. In: *Medical Image Computing and Computer-Assisted Intervention – MICCAI 2001*. Ed. by Wiro J. Niessen and Max A. Viergever. Berlin, Heidelberg: Springer Berlin Heidelberg, pp. 449–456. ISBN: 978-3-540-45468-7.
- [52].Withers, Kathleen et al. (2013). “Pipeline™ embolization device for the treatment of complex intracranial aneurysms: a NICE Medical Technology Guidance”. In: *Applied health economics and health policy* 11, pp. 5–13.
- [53].Wu, Tao and Qing Zhu (2021). “Advancement in the haemodynamic study of intracranial aneurysms by computational fluid dynamics”. In: *Brain Hemorrhages* 2.2, pp. 71–75.

[54].Zhang, Hegui et al. (2020). “Comparison of computational fluid dynamic simulation of a stirred tank with polyhedral and tetrahedral meshes”. In: *Iranian Journal of Chemistry and Chemical Engineering* 39.4, pp. 311–319.